NASA TN D-92

TECHNICAL NOTE

D-92

MEASURED AND THEORETICAL FLOW FIELDS BEHIND A RECTANGULAR AND A TRIANGULAR WING UP TO HIGH ANGLES OF ATTACK AT A MACH NUMBER OF 2.46

By Frank J. Centolanzi

Ames Research Center
Moffett Field, Calif.

NATIONAL AERONAUTICS AND SPACE ADMINISTRATION

WASHINGTON September 1959

NATIONAL AERONAUTICS AND SPACE ADMINISTRATION

TECHNICAL NOTE D-92

MEASURED AND THEORETICAL FLOW FIELDS BEHIND A RECTANGULAR AND A TRIANGULAR WING UP TO HIGH ANGLES OF ATTACK AT A MACH NUMBER OF 2.46

By Frank J. Centolanzi

SUMMARY

Measurements were made of the flow field behind a rectangular and a triangular wing of aspect ratio 2 up to angles of attack of 30°. The wings had a 4-inch semispan and were 5 percent thick with maximum thickness at midchord. Tests were performed at a Mach number of 2.46 and a Reynolds number of 3.12 million per foot. Flow-field measurements were taken for wing angles of attack of 0°, 6°, 20°, and 30°.

The downwash, sidewash, Mach number, and dynamic pressure in the wakes of both wings are compared with the predictions of various theoretical methods. The results show that for angles of attack up to 20° these flow quantities can be calculated with sufficient accuracy for most engineering purposes.

The measured downwash, dynamic pressure, and Mach number in the wake of the rectangular wing were used to estimate the effectiveness of a hypothetical tail placed at various heights above and below the chord plane of the wing. The effectiveness was also computed using shock-expansion theory to determine the required flow quantities. These two calculations of the tail effectiveness are in fair agreement.

INTRODUCTION

The determination of the stability and control of high-speed aircraft operating at high altitudes and Mach numbers requires knowledge of the flow field behind wings over a wide range of angles of attack. Most of the previous experimental investigations of the flow field behind wings have been confined to relatively low angles

of attack (e.g., refs. 1 and 2). At high angles of attack (greater than 15°) little experimental data is available. In reference 1, surveys of the downwash, sidewash, Mach number, and dynamic pressure were made behind a rectangular wing at a Mach number of 1.6 up to 6° angle of attack. The predictions of supersonic vortex theory agree reasonably well with experimental results in the plane of the wing but not above or below it. In reference 2, flow-angle and pitot-pressure surveys were made at stations relatively far (1.5, 3.0, and 4.0 chord lengths) behind five pointed tipped wings of various plan forms for angles of attack from 9° to 17°. The downwash and sidewash were compared with various theoretical methods. The agreement between experiment and theory was good for some plan forms but poor for others.

The purpose of this paper is to present details of the flow field behind and near the trailing edge of a rectangular and a triangular wing up to high angles of attack and to assess the extent of applicability of existing theories in predicting the flow-field characteristics. The theories are first assessed directly by comparison of measured and theoretical flow quantities, then indirectly by comparison of the effectiveness of a hypothetical horizontal tail calculated by using both the measured and predicted flow quantities.

SYMBOLS

c local wing chord

c_R root chord

C_L lift coefficient, $\frac{L}{qS}$

C_{L_α} lift-curve slope at local conditions

$C_{L_{\alpha_\infty}}$ lift-curve slope at free-stream conditions

C_{L_α}' effective lift-curve slope of tail (corrected for local dynamic pressure and Mach number)

L lift

M	local Mach number
$\bar{M}$	mean Mach number across tail, $\frac{1}{2s_t}\int_{-s_t}^{s_t} M\,dy$
M_∞	free-stream Mach number
q	local dynamic pressure
q_∞	free-stream dynamic pressure
$\bar{q}$	mean dynamic pressure across tail, $\frac{1}{2s_t}\int_{-s_t}^{s_t} q\,dy$
s	wing semispan
s_t	tail semispan
S	plan-form area
t	wing thickness
V_∞	free-stream velocity
x,y,z	Cartesian coordinates of wind axes measured from wing axis of rotation (see fig. 2)
x'	distance behind leading edge of a typical wing section (see fig. 1)
α	angle of attack
β	$\sqrt{M^2-1}$
Γ	circulation distribution
Γ_T	total circulation
ϵ	downwash angle, deg
$\bar{\epsilon}$	weighted mean downwash at tail, $\frac{1}{2s_t\bar{q}}\int_{-s_t}^{s_t} \epsilon q\,dy$
σ	sidewash angle, positive outward, deg

Subscripts

c	extended wing chord
t	tail
v	vortex
W	wave
w	wing

EXPERIMENT

Apparatus

Models and support.- For these tests semispan rectangular and triangular wings of aspect ratio 2.0 were used. Their dimensions and orientation with respect to the stream are shown in figure 1. The wings were mounted on a boundary-layer plate (which serves to bypass the tunnel boundary layer) in the Ames 1- by 3-foot supersonic wind tunnel No. 1 as shown in figure 2. Both wings were pitched about axes passing through their centroid of area. The angle of attack could be varied manually from outside the wind tunnel.

Instrumentation.- The flow-field surveys were made with a rake of five 40° included-angle cones. Each cone had four equally spaced static-pressure orifices on its surface and a total-pressure orifice at its apex. The details of the cones and the rake are shown in figure 3. The pressures were measured by means of a multiple-tube manometer filled with tetrabromoethane. The measured pressures are used to determine the local flow angles, dynamic pressure, and Mach number in the manner of reference 3. The survey rake was attached to a wedge-shaped strut and mounted from a circular support plate through one of three rectangular holes. Each of the holes was located at a different distance from the center of the plate, thereby giving three choices of longitudinal position. The holes not used were fitted with observation windows. A fourth hole located at the center of the plate was for observation purposes only. The lateral and vertical positions of the rake were adjustable from outside the wind tunnel. The rake could be pitched in order to compensate for the large downwash angles at high angles of attack.

Tests

Test procedure.- The tests were conducted at a free-stream Mach number of 2.46 and a Reynolds number of 3.12 million per foot. The flow field behind the rectangular wing was surveyed at the streamwise stations $x/c = 0.56$ and 1.10. These stations were approximately 1/4 inch and 2-1/2 inches, respectively, behind the wing trailing edge at zero angle of attack. The triangular wing was surveyed at the station $x/c_R = 0.55$ only which was approximately 1-3/4 inches behind the wing trailing edge. Each of the wings was tested at angles of attack of 0°, 6°, 20°, and 30°. At each angle of attack greater than zero the range from $y/s = 0.125$ to 1.5 and $z/s = -1.25$ to $+1.25$ was surveyed in 1/4-inch increments. At zero angle of attack the surveys were made in 1/2-inch increments in most cases since the flow variations were expected to be small. At high angles of attack, where large downwash angles were expected, the survey rake was pitched upward to compensate for the large downwash angles.

The flow-field measurements in each of the three selected survey planes were made first with only the boundary-layer plate in the wind tunnel. The measurements were then repeated with the wings installed. The flow angles measured with the wings removed were subtracted from those measured with the wings present. This procedure corrected for the presence of stream angle and any slight misalinement of the cones. The average magnitude of these corrections was approximately 0.25°.

Precision of the data.- The errors in the controlled conditions are estimated to be as follows:

M_∞	± 0.01
α	$\pm 0.1^\circ$
x,y,z	± 0.01 inch

In a uniform stream the instruments are capable of measuring Mach number, dynamic pressure, and flow angles with the precision tabulated as follows:

M	± 1.0 percent
q	± 1.0 percent
ϵ and σ	$\pm 0.25^\circ$

In the wake of the wing the precision of the instruments is influenced by such factors as stream gradients, shock waves, and separation. These effects tend to increase the estimated errors. At high angles of attack these effects become large enough in some regions to invalidate the data. In this case the curves are either extrapolated from reliable data or omitted entirely.

Results

The downwash, sidewash, Mach number, and dynamic-pressure data for both wings are presented in contour plots in figures 4 through 22. In regions where the data appeared questionable or have been extrapolated, the contours are shown dotted. In either case the dotted line represents the best estimate. In order to compensate for the large downwash angles, the rake was pitched 10° in some cases (see sketch (a)). Because the rake adjustments were in planes normal to the free-stream, each cone surveyed a different chordwise position. Since the streamwise gradients of downwash, sidewash, dynamic pressure, and Mach number between the planes surveyed by adjacent cones (i.e., between points A and B in the sketch) were found to be small, the contours in each of the planes were connected in order to facilitate the data presentation. The location of each of these planes relative to each wing is indicated on the contour plots. In figures 4 through 7

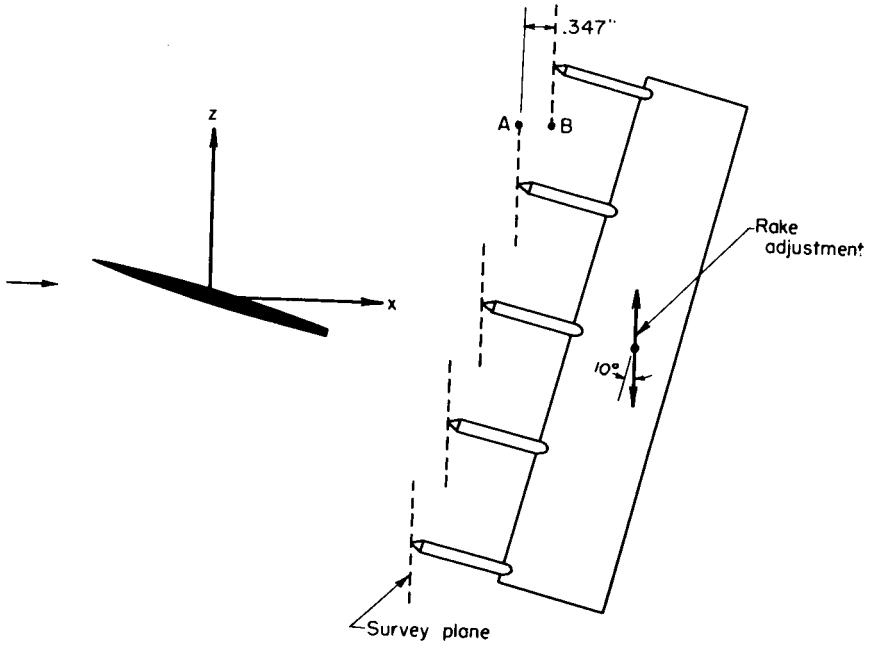

Sketch (a)

are shown the downwash contours for the rectangular wing. At 0° angle of attack the downwash contours are asymmetrical contrary to expectations, especially in the region near the shock waves in the plane $x/c = 0.56$. This asymmetry is due to the fact the wing is at a small angle of attack as a result of support misalinement. For angles of attack greater than zero the downwash variations indicate the presence of a vortex near the tip. At the high angles of attack the increased distance between the points of maximum and minimum downwash indicates a substantial increase in the size of the viscous core.

The regions of two-dimensional flow are characterized by straight contours which are normal to the Z-axis in the survey plane, in contrast to the curved contours in the regions of three-dimensional flow. The position of shock waves is indicated by the coalescence of these lines. At high angles of attack the region of two-dimensional flow extends farther outboard above the wing than below the wing because the Mach numbers on the upper surface are greater than those on the lower surface. As a result the Mach lines on the upper and lower surfaces move outboard and inboard, respectively, as shown in sketch (b).

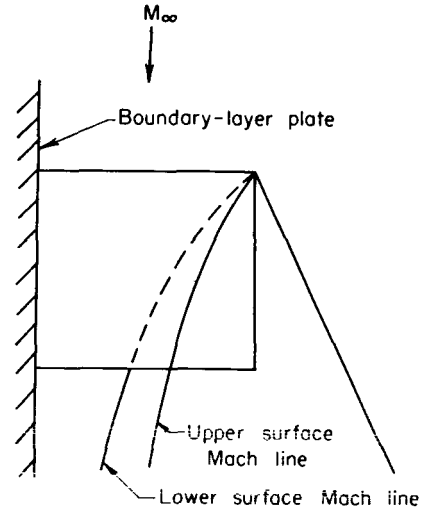

Sketch (b)

In figures 8 through 10 are shown the sidewash contours for the rectangular wing. At 0° angle of attack the sidewash is negligible; therefore, no data are presented. For angles of attack greater than 0° these curves, like the downwash curves, show the presence of a vortex near the tip of the wing. In the region of two-dimensional flow the sidewash is, of course, zero.

The dynamic-pressure ratio, q/q_∞, and Mach number contours for the rectangular wing are shown in figures 11 through 18. In the vicinity of the vortex core the dynamic pressures and Mach numbers decrease markedly. At the station $x/c = 0.56$ for 20° and 30° angles of attack, there exists a wide region of low dynamic pressures and Mach numbers in the wake (see, e.g., figs. 13(a) and 14(a)) which indicates that the flow separates before reaching the trailing edge (see sketch (c)).

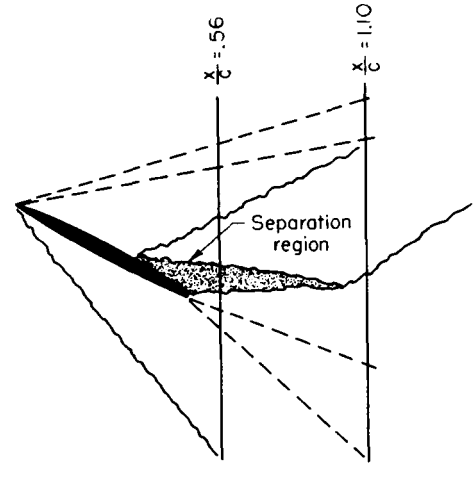

Sketch (c)

Farther downstream, at the station $x/c = 1.10$ the separated region has closed, resulting in higher dynamic pressures and Mach numbers.

In figures 19 through 22 are shown the downwash, sidewash, dynamic pressure, and Mach number contours behind the triangular wing. For 6° angle of attack the downwash and sidewash variations between the trailing-edge waves indicate the presence of vorticity. The low dynamic pressures behind the trailing edge at 20° and 30° angles of attack indicate the possibility of flow separation. In this region it is difficult to obtain accurate flow measurements.

THEORETICAL METHODS

There are three well-known methods available for predicting the flow field behind wings at supersonic speeds:

1. Two-dimensional shock-expansion theory.
2. Linearized wing theory.
3. Vortex theory.

A description of each theory and the method by which each is applied is discussed in the following sections.

Shock-Expansion Theory

For a rectangular wing the region outside the influence of the tips is two-dimensional. In the absence of separation, the flow field in this region can be predicted by shock-expansion theory which is valid up to the angle of attack at which shock detachment occurs. For the wing used in these tests the angle of attack at which shock-detachment occurs was about 24° at $M_\infty = 2.46$. In the application of the theory the following assumptions are made:

1. The interaction of the Mach waves from the curved wing surface with the shock waves at the leading and trailing edges is neglected.

2. At the blunt trailing edge the flow from the upper and lower surfaces is assumed to return to the free-stream direction. A more exact calculation, which takes into account the presence of a slip plane in the wake, has shown that this assumption is valid in the present application since the slip plane is inclined only 1° upward from the free stream at 20° angle of attack at the Mach number under consideration (2.46). It should be noted that, theoretically, the upwash at the trailing edge increases both with Mach number and with angle of attack, so that in the case of a wing at large angles of attack at high Mach numbers, the present assumption may not be valid.

3. The presence of separation near the trailing edge (see sketch (c)) is neglected.

In this report the shock-expansion theory is applied also to the triangular wing. Since the leading edge of the wing is supersonic, each local wing chord is treated as a two-dimensional airfoil. The resulting flow field is then computed by the conventional shock-expansion methods. Strictly speaking, the shock-expansion theory is not applicable to triangular wings in this fashion because the flow is not two-dimensional. The method, however, might furnish a good approximation of the downwash, Mach number, and dynamic-pressure variations because the theory accounts for the presence of shock waves and expansion waves which other theories neglect.

Linearized Theory

A linearized theory solution for the downwash and sidewash behind a rectangular wing is presented in reference 4. For regions between the trailing-edge waves the downwash can be evaluated only by numerical integration techniques since no closed form solutions are available at this time. In the vortex sheet, $z = 0$, the numerical integrations have been performed and the downwash results have been presented for various spanwise and streamwise stations behind the wing. For regions outside the influence of the trailing edge the downwash and sidewash solutions are presented in closed form. In the application of linearized theory in these regions, the movement of the bow waves with angle of attack can be taken into account by choosing the corresponding points for the experimental and theoretical comparisons by means of the following relationship (see sketch (d)):

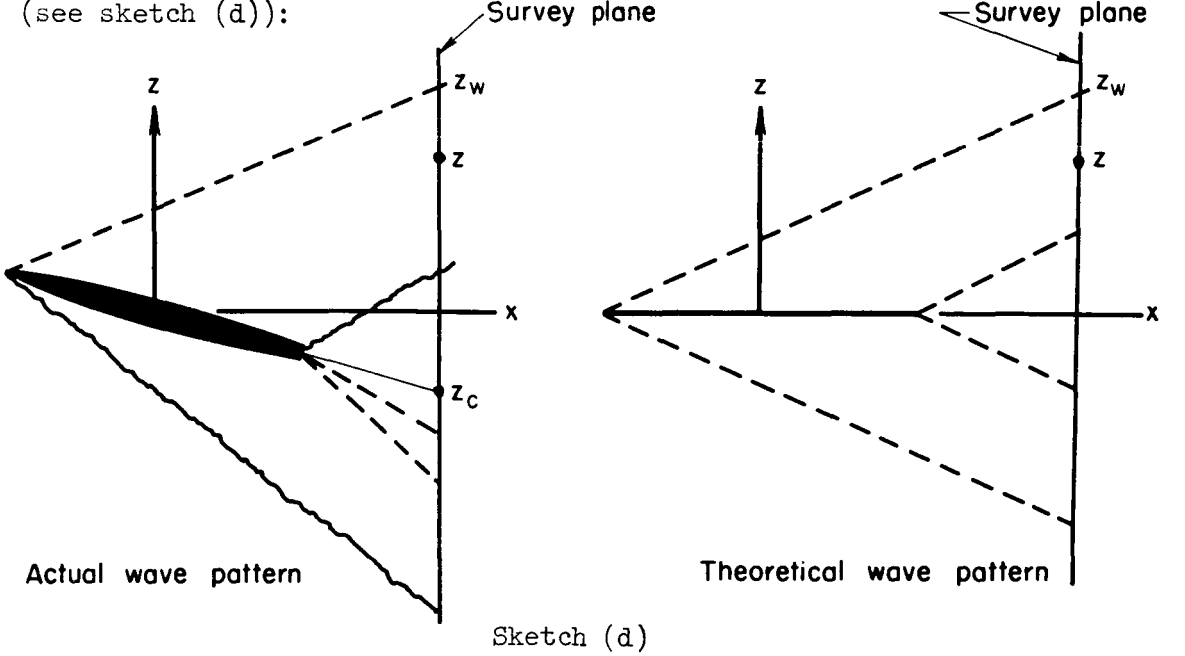

Sketch (d)

$$\frac{z_{Theor}}{z_{W_{Theor}}} = \frac{z_{Exp} - z_c}{z_{W_{Exp}} - z_c}$$

This insures that for the actual case the following boundary conditions are satisfied:

1. On the wing surface $\epsilon = \alpha$

2. At the bow wave $\epsilon = 0$

In applying this formula the experimental positions of the bow waves in the region of two-dimensional flow were used. In this region the position of the bow waves can also be predicted closely by shock-expansion theory. The downwash and sidewash in the region of the tip are calculated by using the constant value of z_{Theor} obtained from the method outlined above in the linearized theory.

The linearized theory solutions for the conical part of the downwash and sidewash field behind a triangular wing are presented in references 5 and 6. The results are presented in the form of charts for various combinations of leading-edge sweep angle and free-stream Mach number. In the region between the trailing-edge waves, the downwash and sidewash must be evaluated by other techniques, such as the lift cancellation method described in reference 4. In the application of the theory the movement of the bow waves with angle of attack can be taken into account in a manner similar to that for the rectangular wing.

Vortex Theory

The use of line vortex theory to compute the downwash and sidewash behind wings in supersonic flow offers a convenient method for approximating the more exact linearized wing theory solutions between the trailing-edge waves. In reference 7, a method, which accounts for the rolling up of the vortex sheet, is outlined for computing the downwash and sidewash behind wings and wing-body combinations by means of incompressible, infinite-line vortices. In references 2 and 8 the details for performing the downwash and sidewash calculations for supersonic horseshoe vortices are presented.

Vortex strengths and positions.- In application of the vortex theory the wing loading is replaced with finite-strength vortices. The strengths

and lateral positions of the trailing vortices are determined by a stepwise approximation to either the theoretical or experimental span loading (see sketch (e)). Since the area under the span loading curve represents the total lift of the wing, the strengths and positions of the vortices are chosen so that this area is preserved. Unless otherwise indicated the strength of each of the vortices is taken to be Γ_T/n where n is the number of vortices. The bound portion of the vortices can be located by connecting the lines of constant circulation from the trailing edge of the wing. In order to facilitate computation, the curved portions of the vortices were approximated by straight line segments. For the case of a rectangular wing, neglecting the chordwise loading and placing the bound portion of the vortices at the midchord position further simplifies the computations. For cases where the vortex sheet is essentially rolled up and the experimental positions of the cores are known, a single horseshoe vortex can be placed at the known position with strength sufficient to account for the total lift.

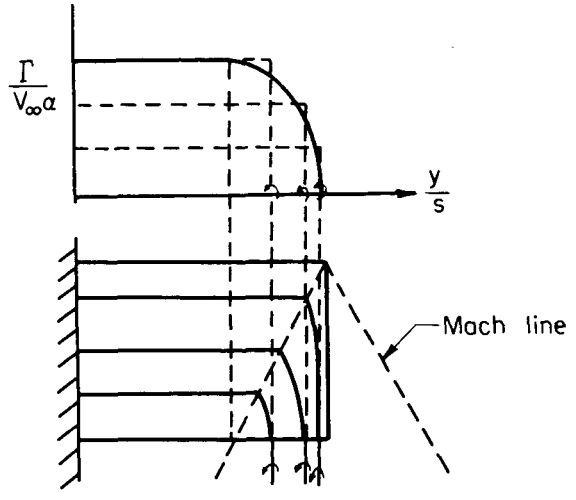

Sketch (e)

Span loading and vortex models.- The comparisons of the experimental and theoretical span loading for the rectangular and triangular wings are shown in figure 23. The experimental span loadings of the present models are reported in reference 9. For the rectangular wing the linearized theory closely predicts the span loading for $\alpha = 6^\circ$ but underestimates the loading for $\alpha = 20^\circ$. For the triangular wing the theory, in general, overestimates the span loading except for $\alpha = 20^\circ$ near $y/s = 0$. At high angles of attack the loading on the triangular wing tends to become linear with y/s. The vortex models used for predicting the flow field behind the rectangular and triangular wings are shown in figures 24 and 25. In each case, a single-horseshoe-vortex model is compared with a three-horseshoe-vortex model having equal strength vortices which more closely approximates the loading on the wing. In addition, for the rectangular wing at 6° angle of attack, the downwash due to six-infinite-line vortices was computed for one value of z for comparison with that obtained using the horseshoe-vortex models. Since the experimental position of the vortices for the rectangular wing were well defined, the trailing vortex for the single-horseshoe-vortex model was placed at the known spanwise position. The strength of the vortex was chosen so as to account for the total lift of the wing.

The strengths and positions of the vortices based upon both the experimental and theoretical span loadings are shown in figures 24 and 25. For the rectangular wing at 6° angle of attack, it makes little difference which loading is used. At 20° angle of attack the positions of the vortices are changed only slightly, but the strengths are approximately 16 percent higher when the measured span loading is used in place of that given by theory. For the triangular wing at 6° angle of attack the measured and theoretical strengths are equal but the corresponding positions of the vortices differ slightly. For the triangular wing at 20° angle of attack no valid data were obtained in the region where vortex theory was applicable. Therefore, the vortex models obtained with the experimental and theoretical span loadings are not compared at this angle of attack. The downwash and sidewash in the wakes of both wings are computed using the theoretical span loading and are compared with experiment. It is interesting to note that calculations based on the experimental span loadings do not improve the accuracy of the predictions.

Displacement of vortex sheet.- In the computations of the downwash using horseshoe vortices the downward displacement of the vortex sheet was taken into account by placing the horseshoe vortices in the approximate x-y plane of the experimental center of vorticity. This center is defined to be the point at which the downwash and sidewash simultaneously go to zero. In the application of the infinite-line-vortex theory, the initial vortex strengths and positions were determined from the span loading, as described earlier. The methods outlined in reference 7 were used to determine the vortex paths downstream to the plane at which the downwash was desired.

Tail Loads

The lift coefficient of a tail in the wake of a wing is shown in reference 10 to be

$$C_L' = K \frac{\bar{q}}{q_\infty} C_{L_{\alpha_t}} (\alpha_t - \bar{\epsilon})$$

where K is a constant taken equal to 1.0 for the present application. If $\bar{\epsilon}$ is a linear function of α_t and is zero at $\alpha_t = 0$, the equation can be written

$$\frac{C_{L_\alpha}'}{C_{L_{\alpha_\infty}}} = \frac{\bar{q}}{q_\infty} \left(1 - \frac{\bar{\epsilon}}{\alpha_t} \right) \frac{C_{L_{\alpha_t}}}{C_{L_{\alpha_\infty}}}$$

The ratio $C_{L_\alpha}'/C_{L_{\alpha_\infty}}$ can be thought of as a measure of tail effectiveness. For a rectangular tail flying at supersonic speeds the lift-curve slope from linearized theory is

$$C_{L_{\alpha_t}} = \frac{4}{\bar{\beta}}\left(1 - \frac{1}{2\bar{\beta}A}\right)$$

where $\bar{\beta} = \sqrt{\bar{M}^2 - 1}$. For small angles of attack where the Mach number and dynamic-pressure changes are small the effectiveness becomes

$$\frac{C_{L_\alpha}'}{C_{L_{\alpha_\infty}}} = 1 - \frac{\bar{\epsilon}}{\alpha_t}$$

The mean values of the measured downwash, dynamic pressure, and Mach number obtained by graphical integration are used to determine the experimental effectiveness. The theoretical effectiveness is determined by using shock-expansion theory to obtain the desired flow quantities.

DISCUSSION

Rectangular Wing

In figures 26 through 31 are shown the comparisons of the measured downwash, dynamic pressure, and Mach number with predictions of shock-expansion theory at both longitudinal stations. In general, the theory predicts the experimental trends and even the magnitude of these quantities with fair accuracy except in the region greatly influenced by the tip or in the viscous wake. It is important to note that for some wings of high effective aspect ratio the greater portion of the flow field may be two-dimensional and can, in general, be predicted reasonably well by shock-expansion theory.

The measured downwash at both longitudinal stations is compared with vortex theory, linearized theory, and shock-expansion theory in figures 32 through 34. For the region between the trailing-edge waves, vortex theory is used. Outside the influence of the trailing edge, linearized theory or shock-expansion theory is used.

The measured downwash in the plane $x/c = 0.56$ outside the region of influence of the trailing-edge is compared with linearized theory and shock-expansion theory in figure 32. Generally, the downwash is predicted with fair accuracy by linearized theory. Outside the region of the tips, where it is applicable, shock-expansion theory can be used to improve the

accuracy somewhat. At this station (which was only 1/4 inch behind the wing trailing edge) the region between the trailing-edge waves was small compared to the size of the conical probes used to measure the flow field; therefore accurate measurements were impossible. For this reason no comparison is made with vortex theory between the trailing-edge waves.

The measured downwash in the plane $x/c = 1.10$ is compared with shock-expansion theory, linearized theory, and line-vortex theory in figures 33 and 34. Outside the region of influence of the trailing edge the agreement between theory and experiment is about the same as that noted above for station $x/c = 0.56$. For the region influenced by the trailing edge, a single-horseshoe-vortex model can be used to predict the trends but not the magnitude of the downwash. Using either a three-horseshoe-vortex model (neglecting chordwise loading) or a three-bent-horseshoe-vortex model (including chordwise loading) provides a small improvement in accuracy over the method using a single-vortex model. At 6° angle of attack for $(z - z_V)/s = 0.10$ the infinite-line-vortex theory does not adequately predict the downwash variation inboard of the tip. For this reason no calculations were performed for 20° angle of attack. For stations farther downstream the infinite-line-vortex theory may predict the downwash more closely. The experimental downwash variations in the vortex region at 30° angle of attack are not compared with theory because of the questionable nature of the data.

The comparisons of the measured and predicted sidewash are shown in figures 35, 36, and 37. It can be seen that the agreement between theory and experiment is generally fair with better agreement above than below the vortex core. Also, it is interesting to note that usually predictions based upon three-horseshoe vortices show little improvement over those based upon a single-horseshoe vortex. As was mentioned previously, the theoretical span loading was used to determine the strengths and positions of the vortices. For the rectangular wing at 6° angle of attack the vortex models obtained by using either the theoretical or experimental span loading are closely similar in regard to strength and position. For this case the differences in the resulting downwash and sidewash can be deduced to be small. At 20° angle of attack there was little difference in the positions of the vortices computed from either loading, but the strengths obtained from the measured span loading were approximately 15 percent higher than those calculated from the theoretical loading. This increase in strength does not, in general, improve the agreement between the theoretical and the experimental downwash and sidewash.

It has been shown that the shock-expansion theory predicts the downwash, dynamic pressure, and Mach number closely in some regions of the flow field. In other regions the trends of downwash and sidewash

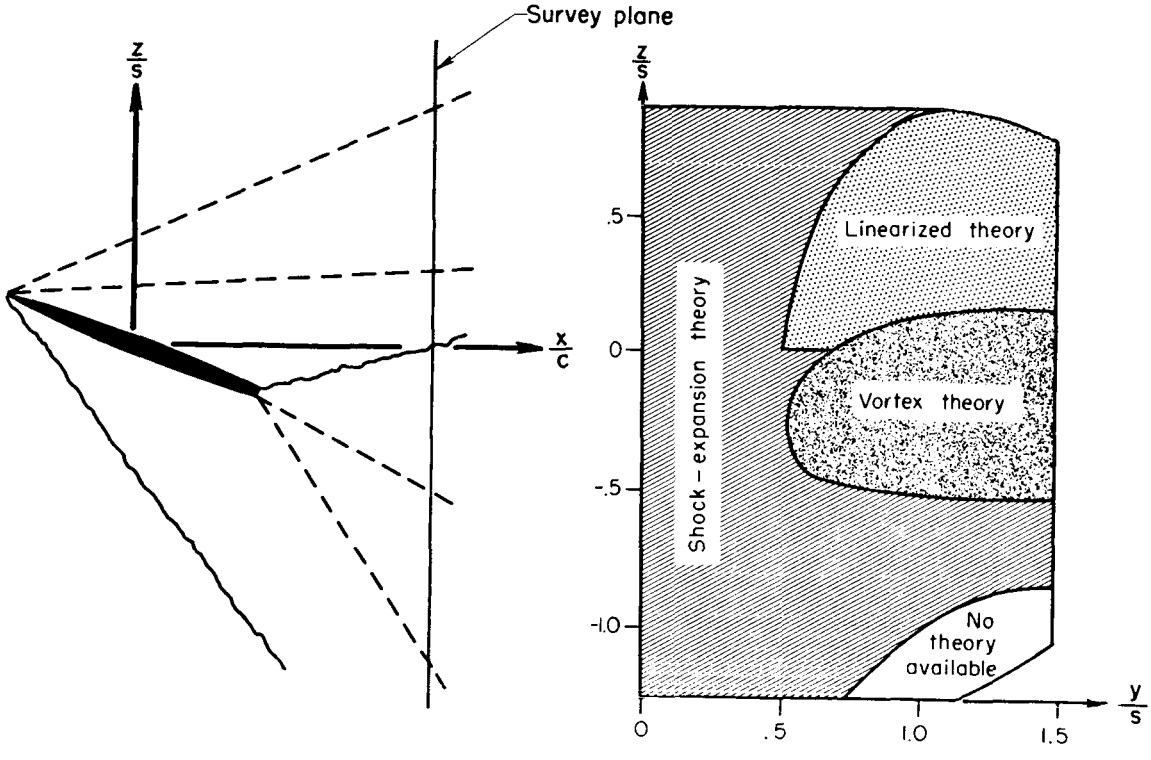

Sketch (f)

can be predicted by vortex theory and linearized theory. In sketch (f) are shown the regions in which the various theories appear to furnish closest approximations to the measured flow characteristics. In the region near the shock wave from the leading edge of the wing none of these theories predict the experimental variations of the flow quantities.

Triangular Wing

In figures 38 through 40 are shown the comparisons of the measured downwash, Mach number, and dynamic pressure with shock-expansion theory. The downwash outside the influence of the trailing-edge has also been compared with the linearized theory of reference 5. Because of the tediousness of the numerical integrations, the linearized theory was not computed for points inside the trailing-edge waves. In general, the shock-expansion theory predicts the variations of these quantities fairly closely except in the region between the trailing-edge waves. Outside the influence of trailing edge the linearized theory predicts the downwash variations with fair accuracy above the wing but not below the wing.

The measured downwash in the region between the trailing-edge waves is compared with vortex theory in figure 41 for $\alpha = 6^\circ$. For points in the plane $z = z_V$, vortex theory based on a single-horseshoe vortex does not adequately predict the downwash. For points removed from the plane of the vortices $[(z-z_V)/s = -0.125]$ the theory based on a single-horseshoe vortex predicts the downwash fairly closely. The theory based upon three-horseshoe vortices predicts the downwash with somewhat better accuracy than that based on a single-horseshoe vortex. If the experimental rather than the theoretical span loading were used to determine the vortex strengths and positions, the strengths would remain unchanged (see fig. 23), but the trailing portion of the vortices would lie farther inboard. Theoretical downwash calculations based upon the experimental span loading do not improve the agreement between theory and experiment. No comparison with theory is made for $\alpha = 20^\circ$ since no valid data were obtained at this angle of attack between the trailing-edge waves.

The comparisons of the measured sidewash with the linearized theory of reference 7 are shown in figure 42. The theory predicts the experimental trends of sidewash for points above the extended chord plane but not below. In general, the theory does not give good quantitative agreement with the experimental measurements.

Tail Loads

The measured downwash, Mach number, and dynamic pressure in the wake of the rectangular wing at $x/c = 1.10$ were used to evaluate the effectiveness, $C_{L_\alpha}'/C_{L_{\alpha_\infty}}$, of a hypothetical tail placed at various heights above and below the chord plane of the wing. The aspect ratio of the tail was chosen to be equal to that of the wing, and the span to be 50 percent of the wing span. The theoretical effectiveness was computed using shock-expansion theory to determine the required flow quantities. The comparison of the theoretical effectiveness with that obtained using the experimental measurements is shown in figure 43. The effect of neglecting the changes in dynamic pressure and Mach number in the theoretical calculations is shown. It can be seen that for the case investigated the variations in tail effectiveness are predicted with sufficient accuracy for most engineering applications by using only the theoretical downwash. Little improvement in accuracy is obtained by inclusion of the effects of the predicted variations of dynamic pressure and Mach number in the calculations.

CONCLUDING REMARKS

An investigation was conducted to determine the detailed flow field behind a rectangular and a triangular wing both of aspect ratio 2, and to assess the extent of applicability of existing theories in predicting the measured quantities. The measurements were made at a Mach number of 2.46, Reynolds number of 3.12 million per foot, and angles of attack up to 30°. Comparison of the measured quantities, downwash, sidewash, dynamic pressure, and Mach number, with predictions of various theories indicates that, generally, these quantities can be predicted with sufficient accuracy for most engineering applications for angles of attack up to 20°. The above statement was further substantiated for the rectangular wing by comparison of the calculations of effectiveness of a hypothetical tail based upon both the measured and predicted flow quantities.

Ames Research Center
National Aeronautics and Space Administration
Moffett Field, Calif., Feb. 16, 1959

REFERENCES

1. Davis, Theodore: Experimental Investigation of Downwash and Sidewash Behind a Rectangular Wing at a Mach Number of 1.60. Meteor Rep. UAC-45, United Aircraft Corp., Jan. 1950.

2. Boatright, William B.: An Analysis of Pressure Studies and Experimental and Theoretical Downwash and Sidewash Behind Five Pointed-Tip Wings at Supersonic Speeds. NACA RM L54B10, 1954.

3. Centolanzi, Frank J.: Characteristics of a 40° Cone for Measuring Mach Number, Total Pressure, and Flow Angles at Supersonic Speeds. NACA TN 3967, 1957.

4. Lagerstrom, P. A., and Graham, Martha E.: Downwash and Sidewash Induced by Three-Dimensional Lifting Wings in Supersonic Flow. Rep. No. SM-13007, Douglas Aircraft Co., April 1947.

5. Nielsen, Jack N., and Perkins, Edward W.: Charts for the Conical Part of the Downwash Field of Swept Wings at Supersonic Speeds. NACA TN 1780, 1948.

6. Bobbitt, Percy J., and Maxie, Peter J., Jr.: Sidewash in the Vicinity of Lifting Swept Wings at Supersonic Speeds. NACA TN 3938, 1957.

7. Rogers, Arthur W.: Application of Two-Dimensional Vortex Theory to the Prediction of Flow Fields Behind Wings of Wing-Body Combinations at Subsonic and Supersonic Speeds. NACA TN 3227, 1954.

8. Mirels, Harold, and Haefeli, Rudolph C.: Line-Vortex Theory for Calculation of Supersonic Downwash. NACA Rep. 983, 1950. (Supersedes NACA TN 1925)

9. Kaattari, George E.: Pressure Distributions on Triangular and Rectangular Wings to High Angles of Attack - Mach Numbers 2.46 and 3.36. NACA RM A54J12, 1955.

10. Silverstein, Abe: Toward a Rational Method of Tail-Plane Design. Jour. Aero. Sci., vol. 6, no. 9, July 1939, pp. 361-369.

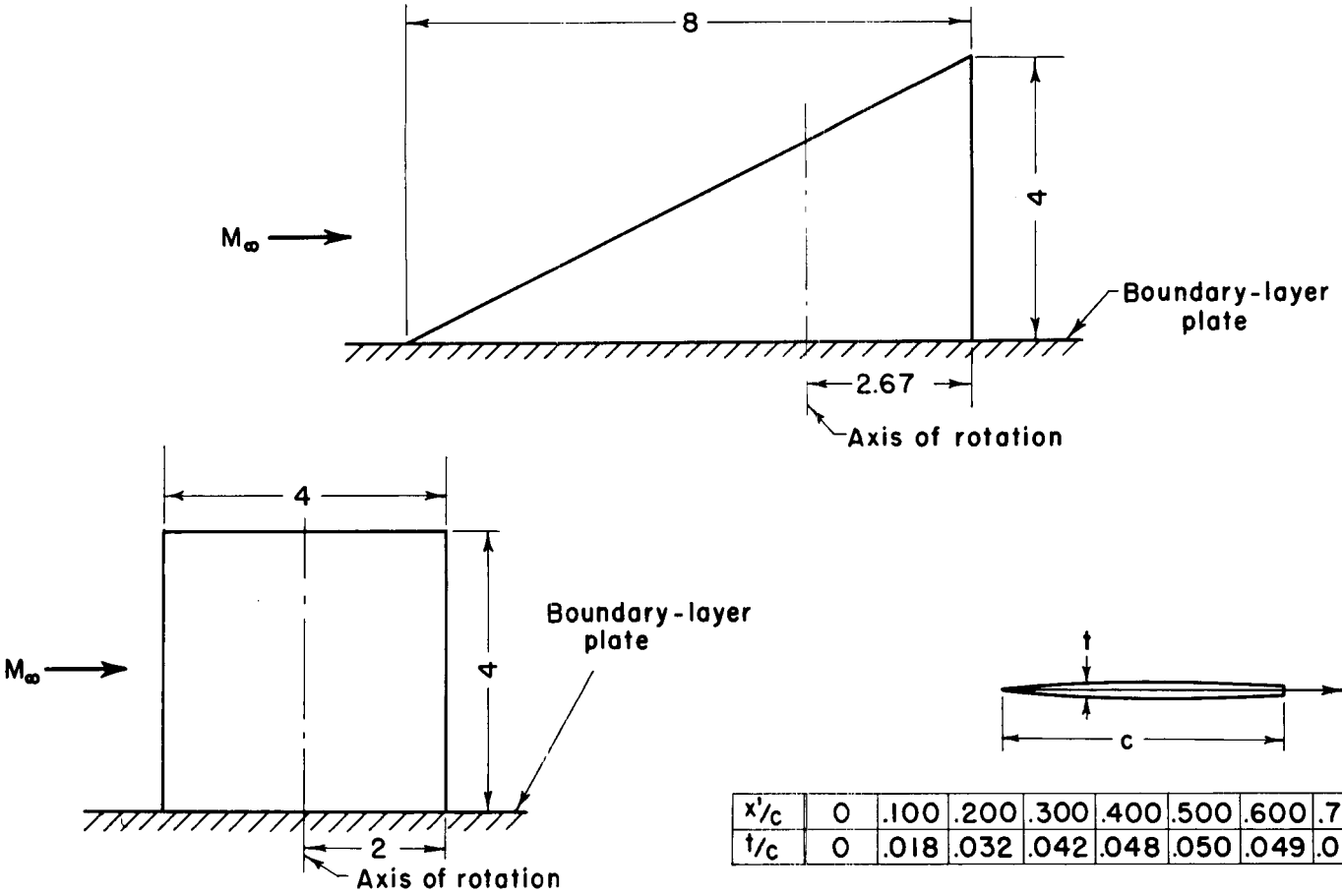

x'/c	0	.100	.200	.300	.400	.500	.600	.700	.800	.900	1.00
t/c	0	.018	.032	.042	.048	.050	.049	.046	.041	.034	.025

Typical streamwise section

Figure 1.- Models.

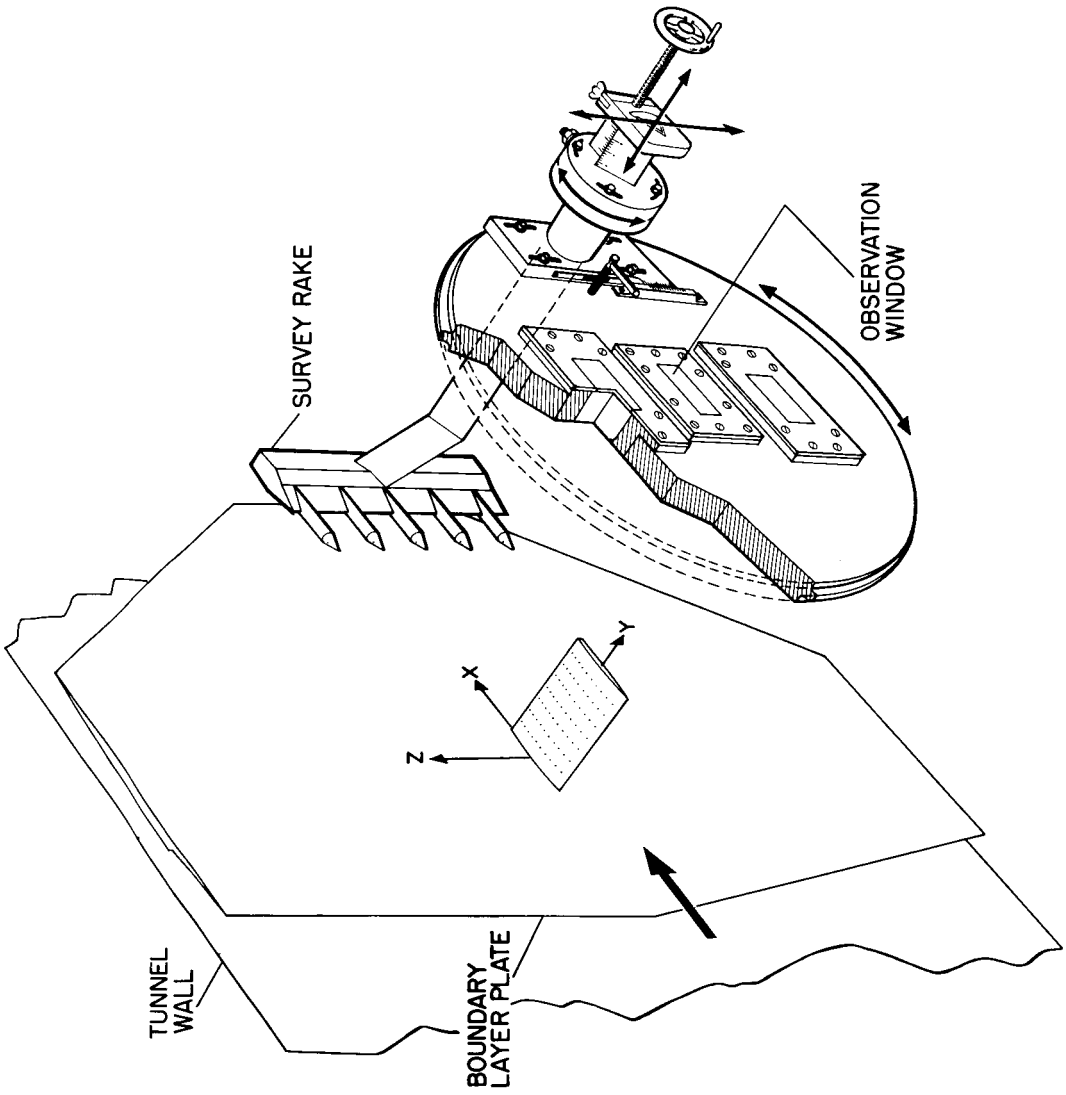

Figure 2.- Model support and survey apparatus.

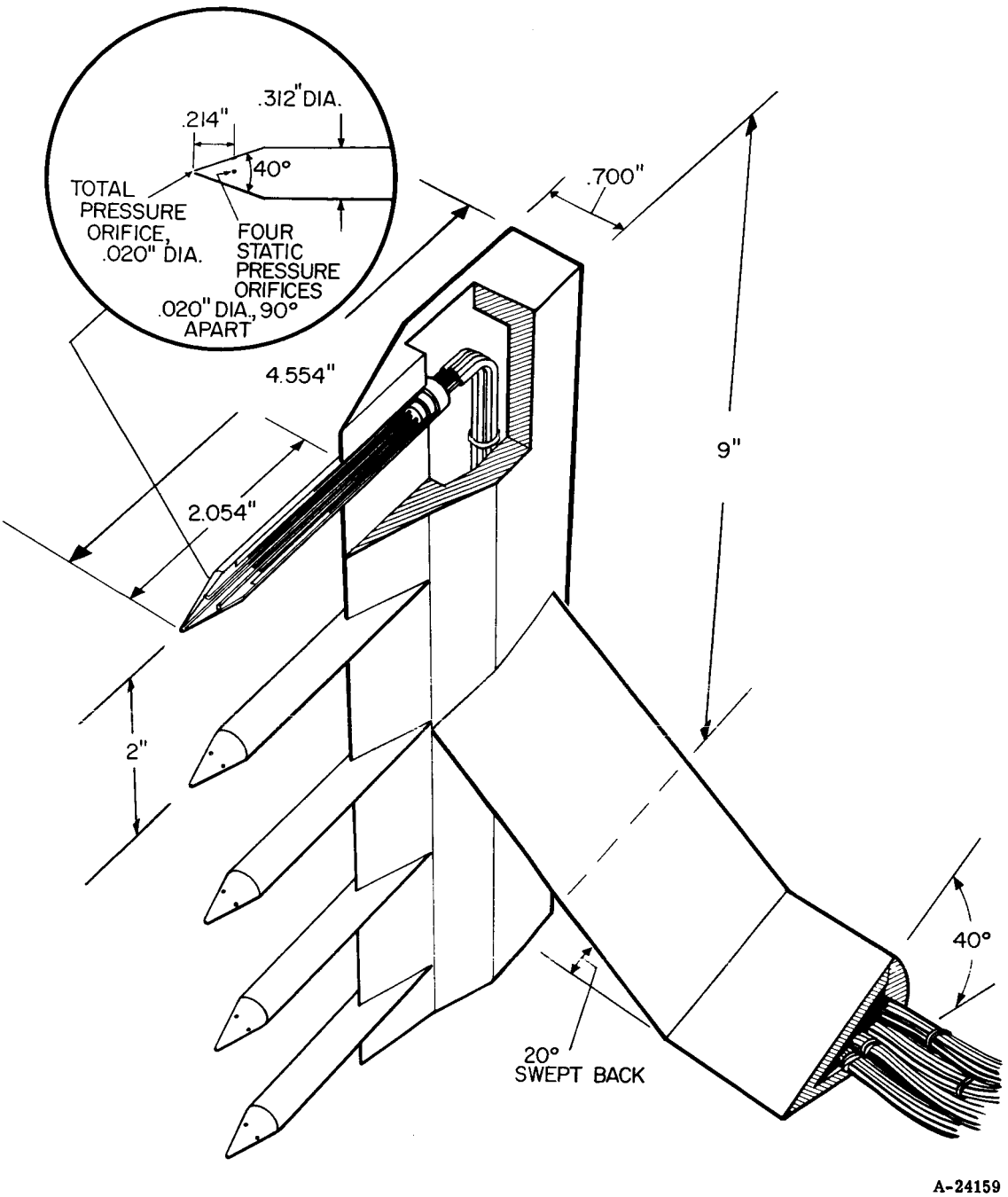

Figure 3.- Details of survey rake.

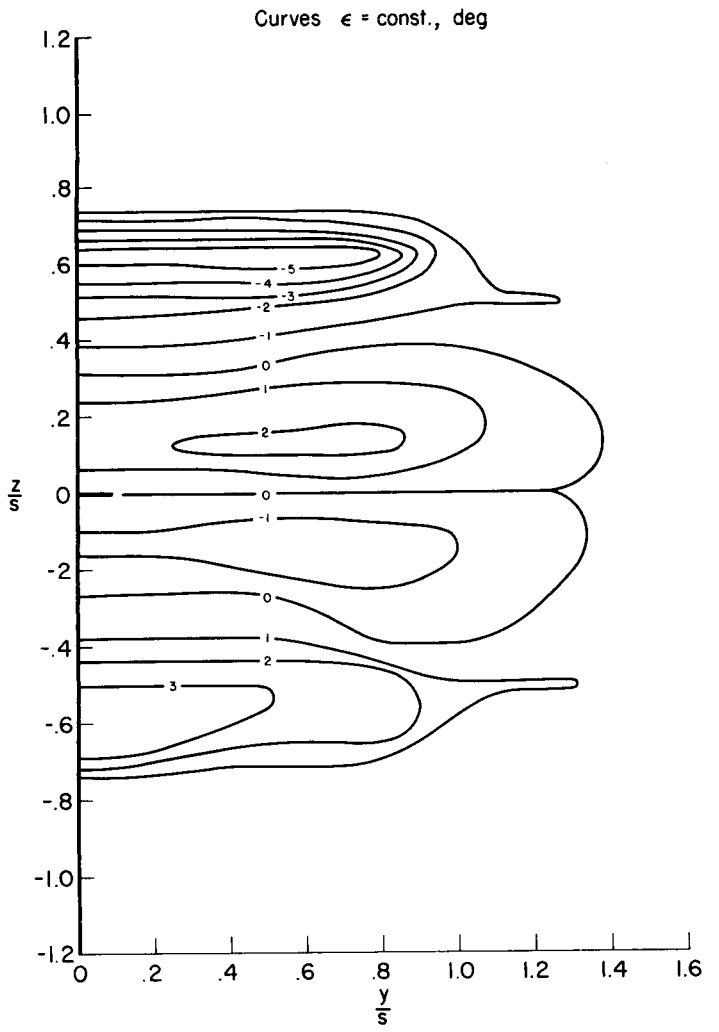

(a) x/c = 0.56

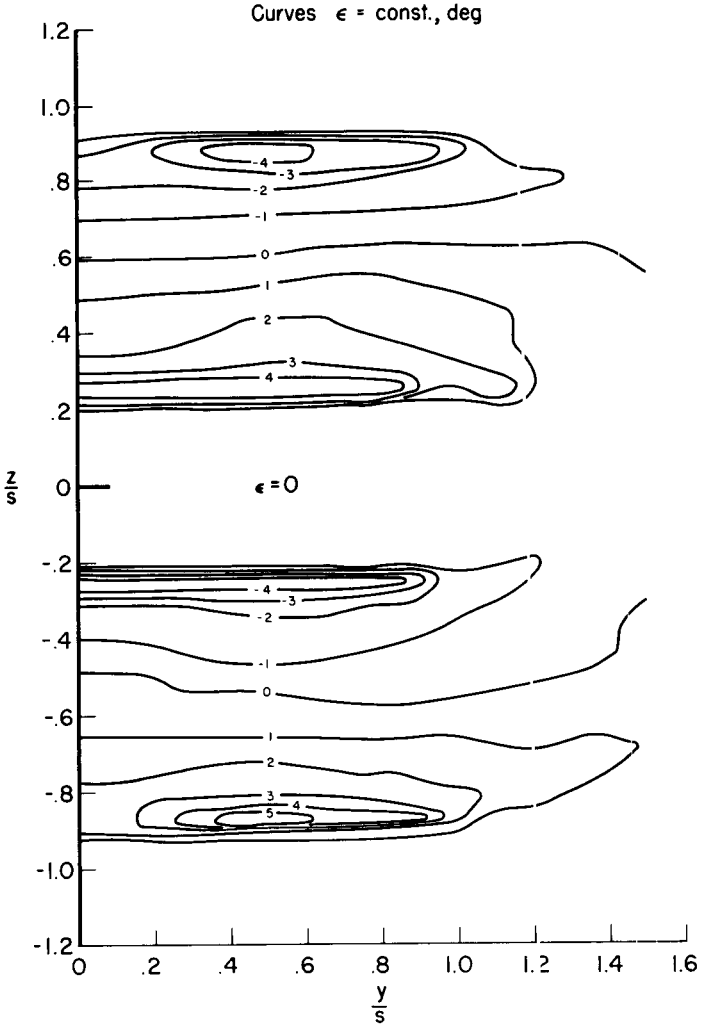

(b) x/c = 1.10

Figure 4.- Contours of constant downwash angle behind rectangular wing; $\alpha = 0^{\circ}$.

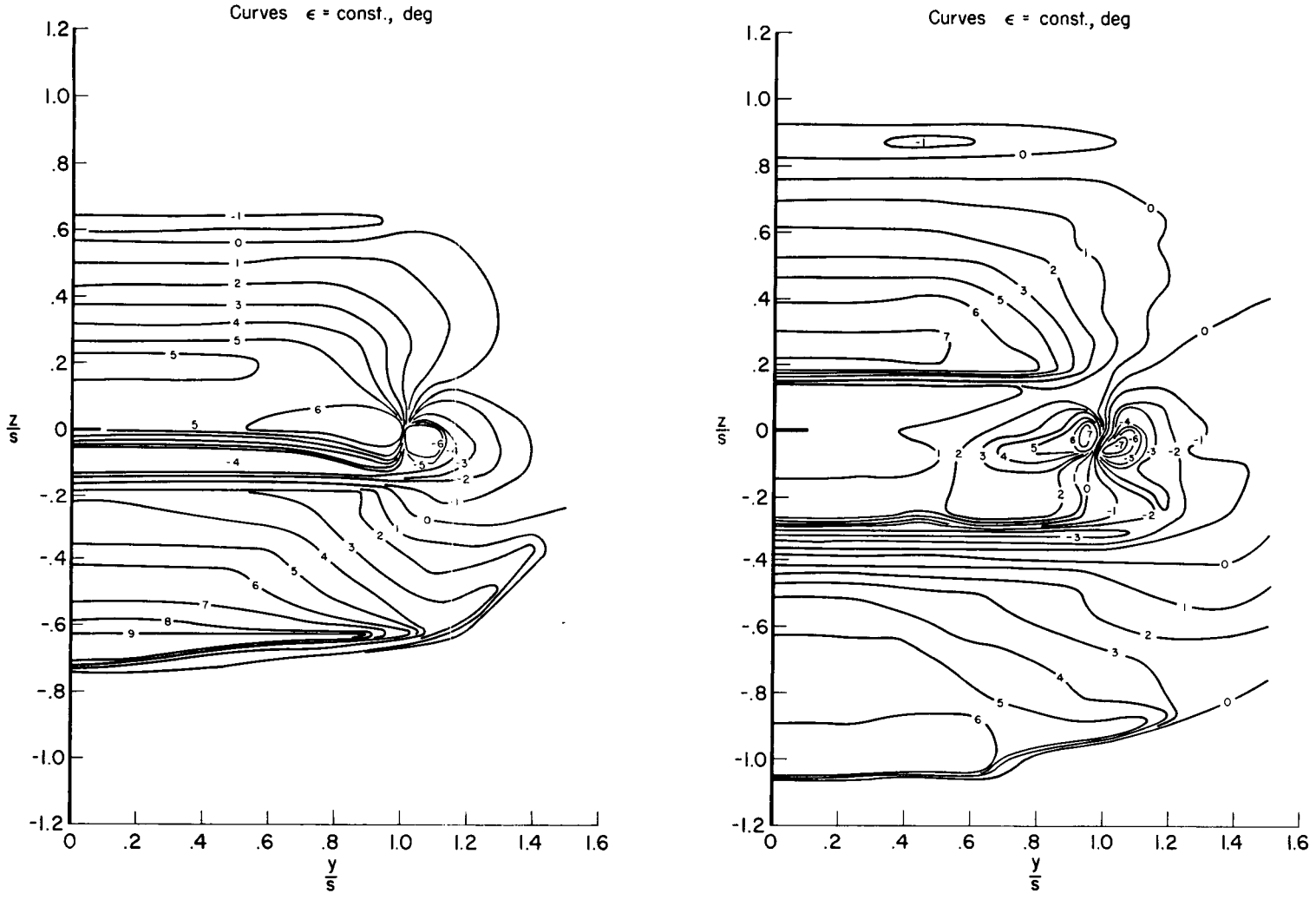

(a) x/c = 0.56

(b) x/c = 1.10

Figure 5.- Contours of constant downwash angle behind rectangular wing; $\alpha = 6^{\circ}$.

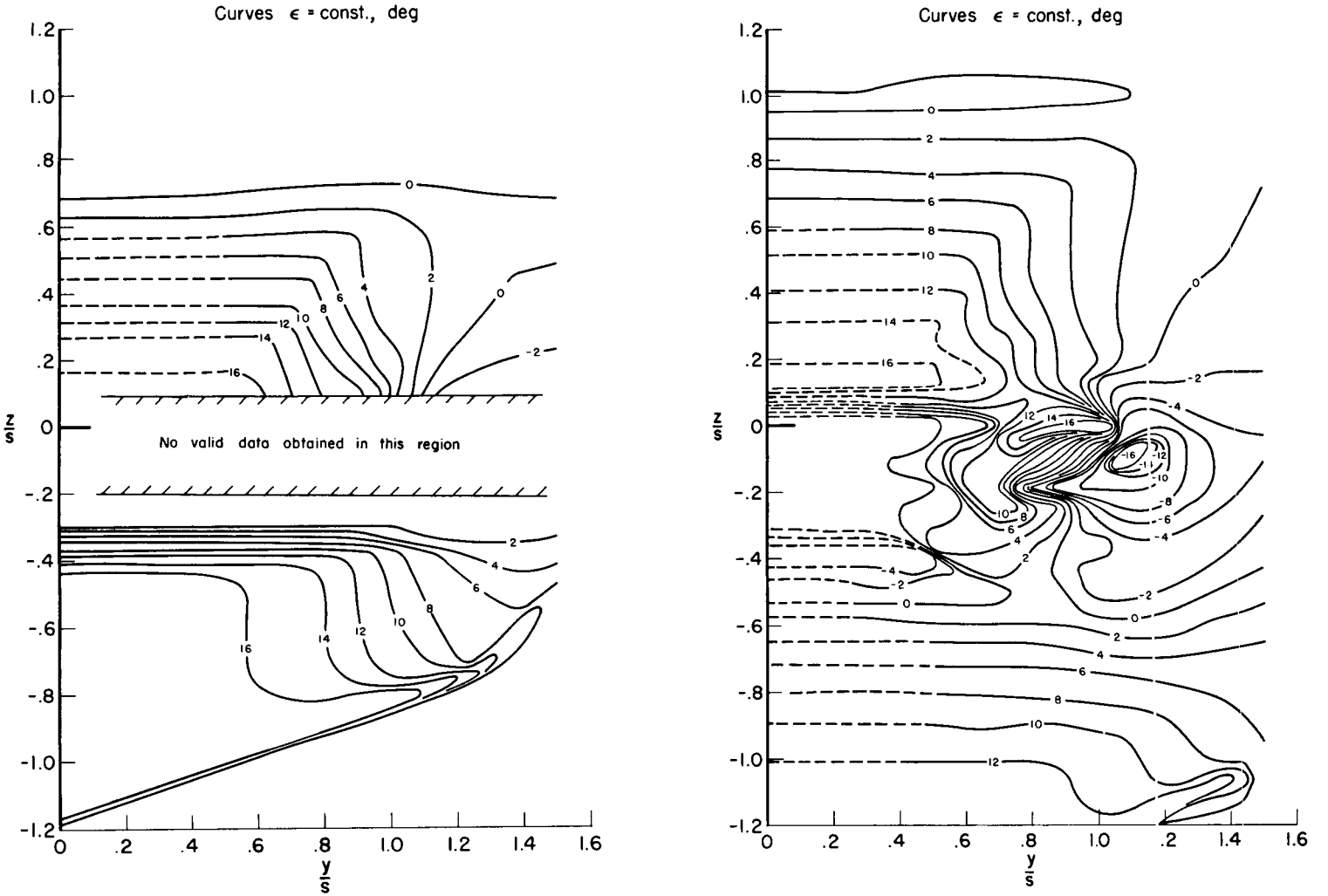

(a) x/c = 0.56

(b) x/c = 1.10

Figure 6.- Contours of constant downwash angle behind rectangular wing; $\alpha = 20^{\circ}$.

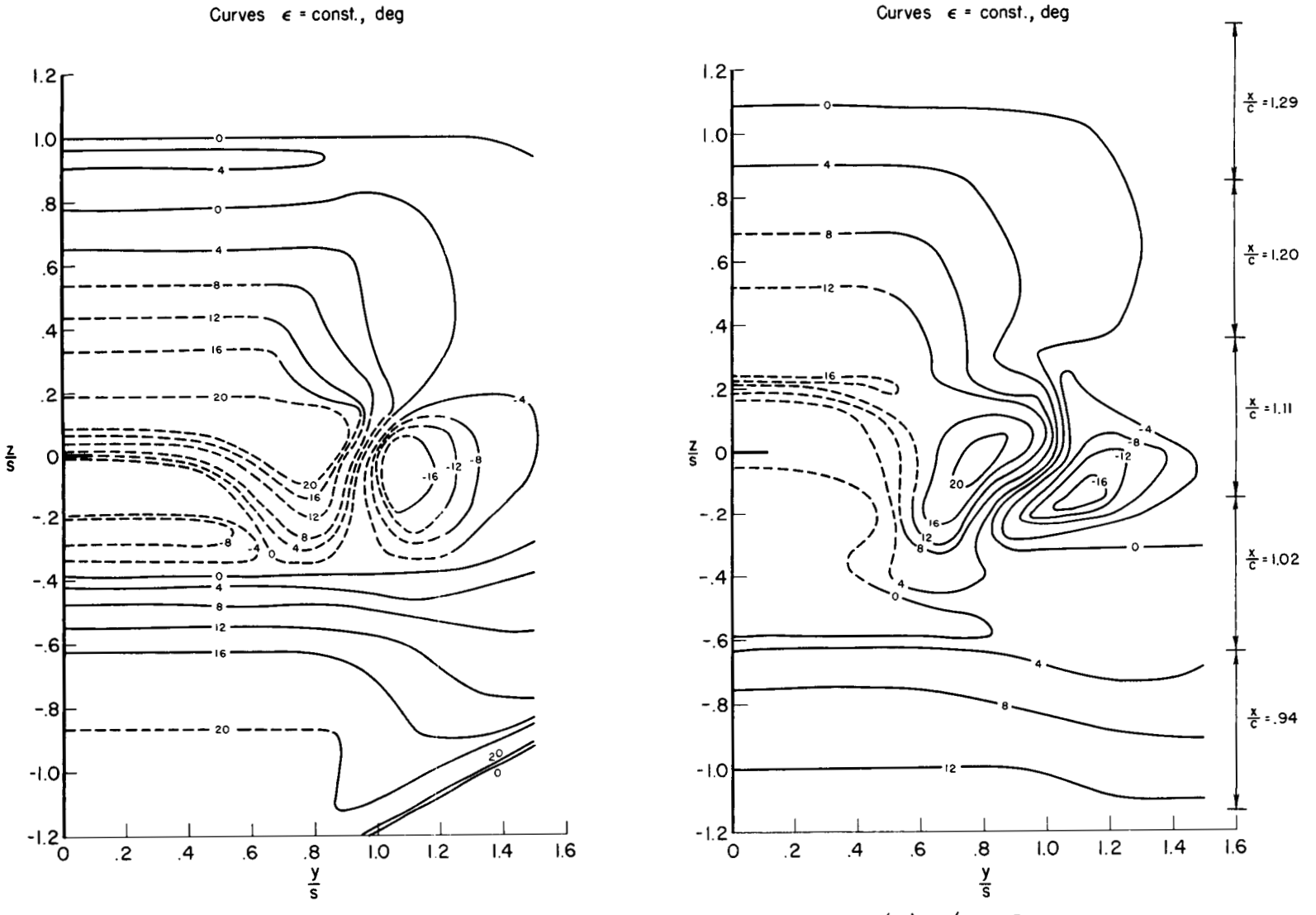

(a) x/c = 0.56

(b) x/c ≈ 1.10

Figure 7.- Contours of constant downwash angle behind rectangular wing; $\alpha = 30^{\circ}$.

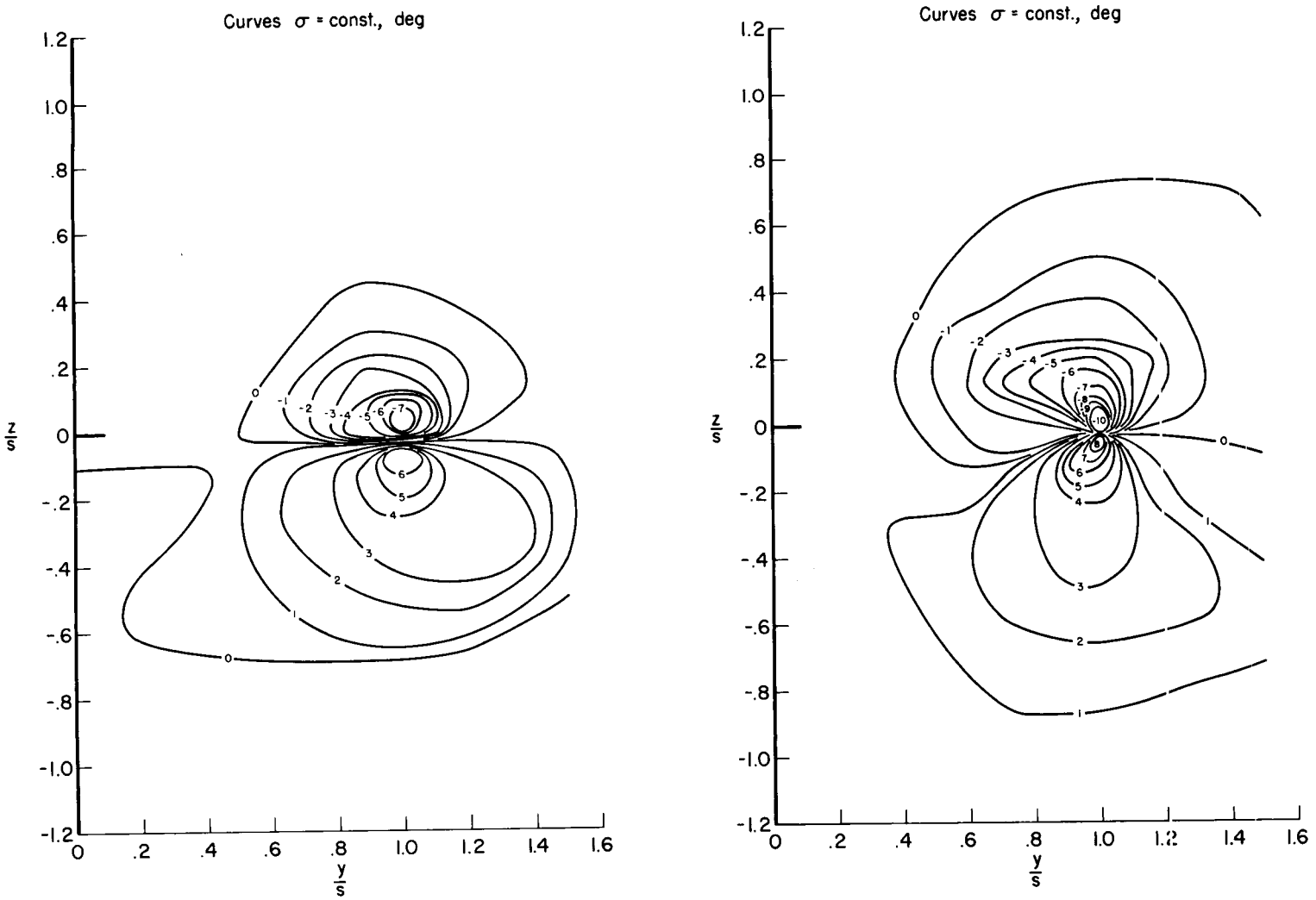

(a) x/c = 0.56

(b) x/c = 1.10

Figure 8.- Contours of constant sidewash angle behind rectangular wing; $\alpha = 6^{\circ}$.

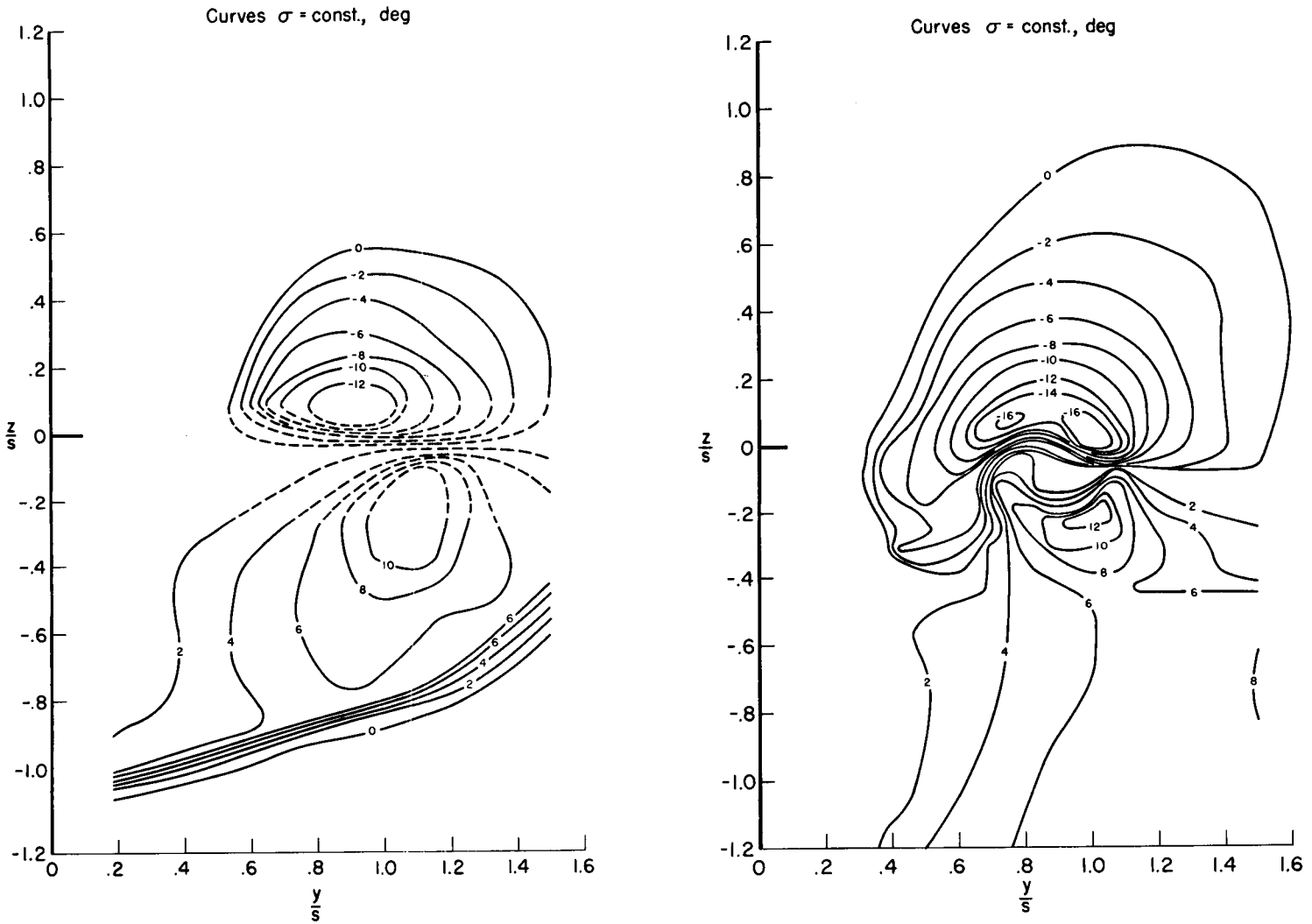

(a) x/c = 0.56

(b) x/c = 1.10

Figure 9.- Contours of constant sidewash angle behind rectangular wing; $\alpha = 20^{\circ}$.

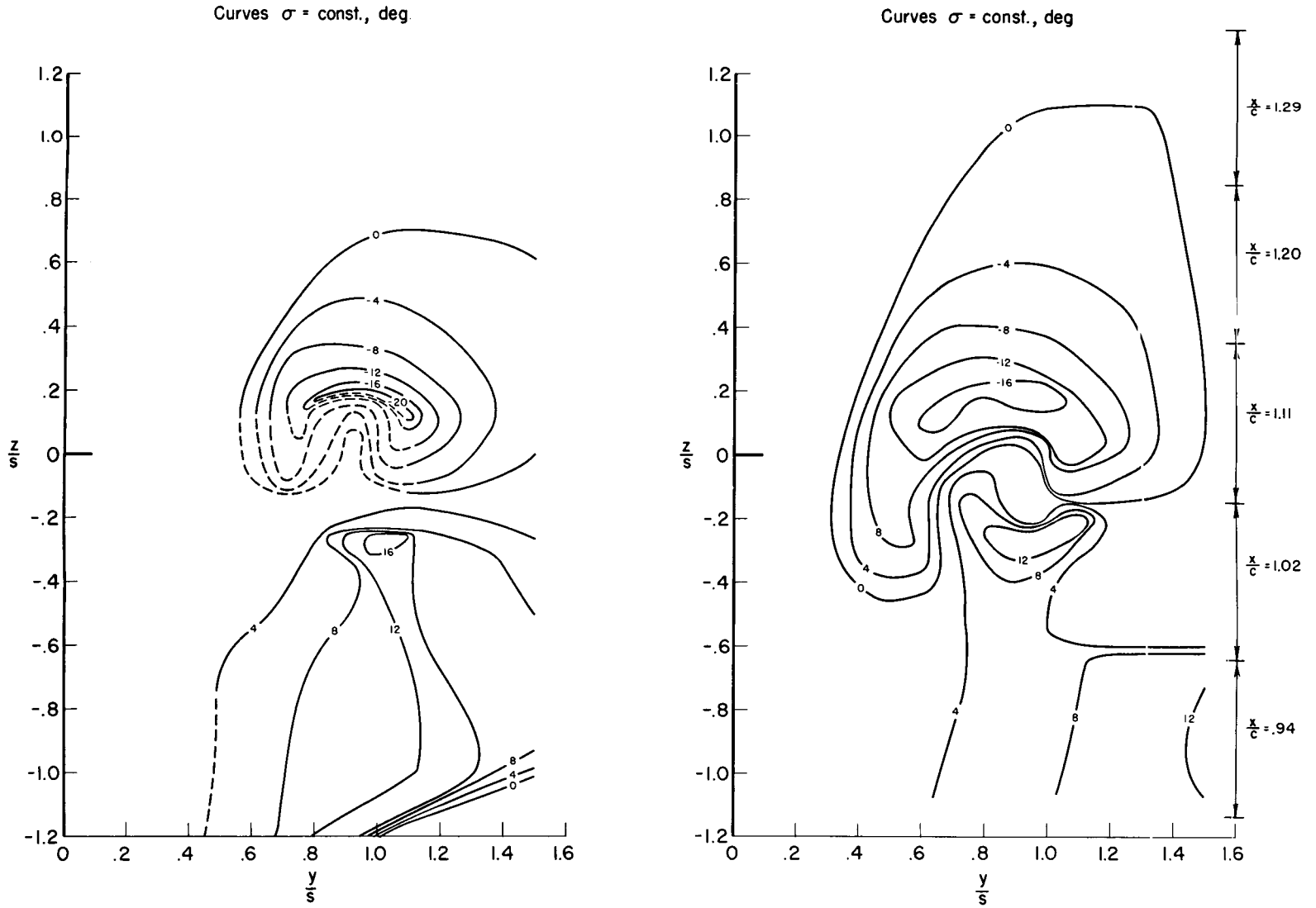

(a) x/c = 0.56

(b) x/c ≈ 1.10

Figure 10.- Contours of constant sidewash angle behind rectangular wing; $\alpha = 30^{\circ}$.

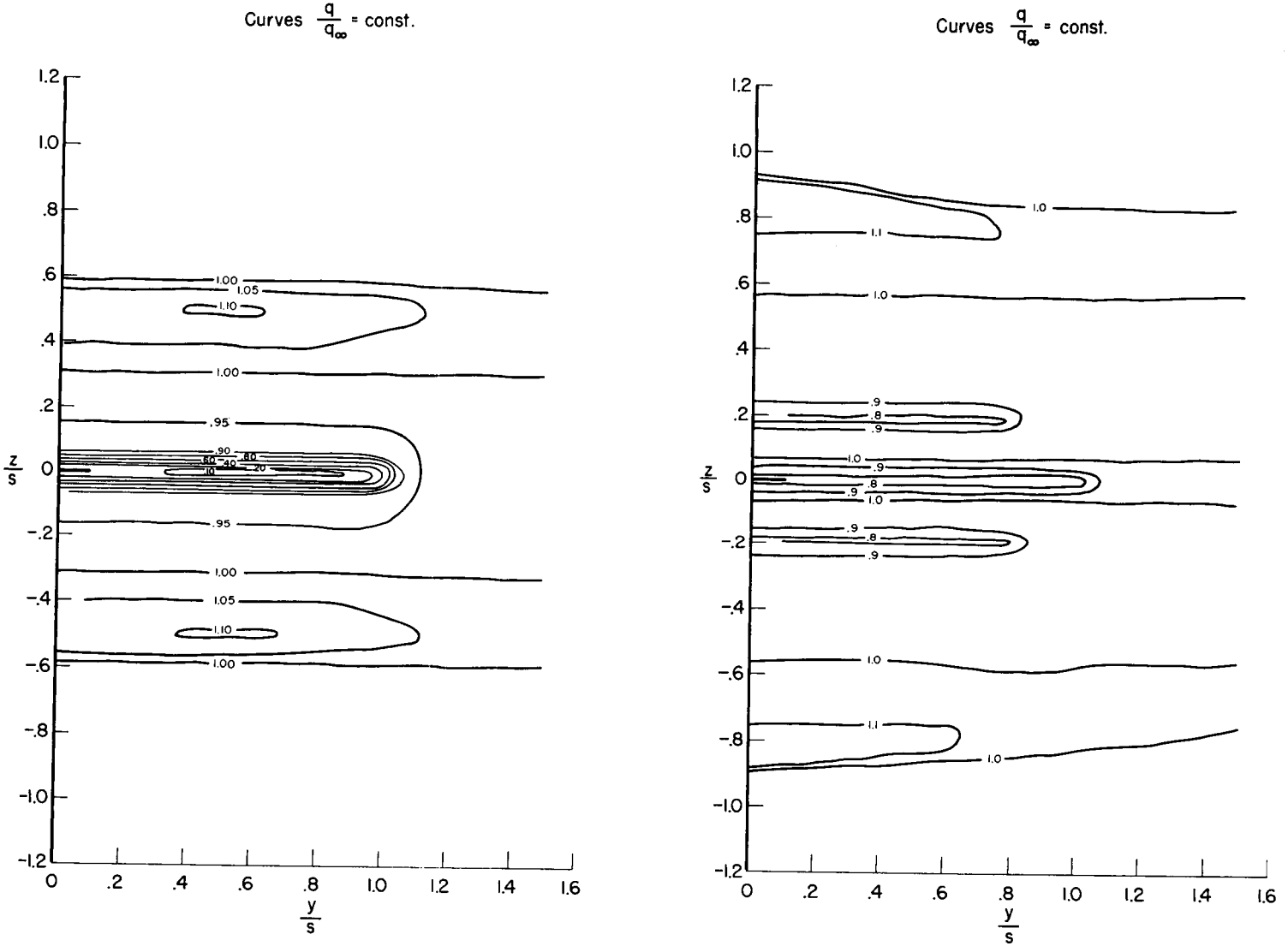

(a) x/c = 0.56

(b) x/c = 1.10

Figure 11.- Contours of constant dynamic-pressure ratio behind rectangular wing; $\alpha = 0^\circ$.

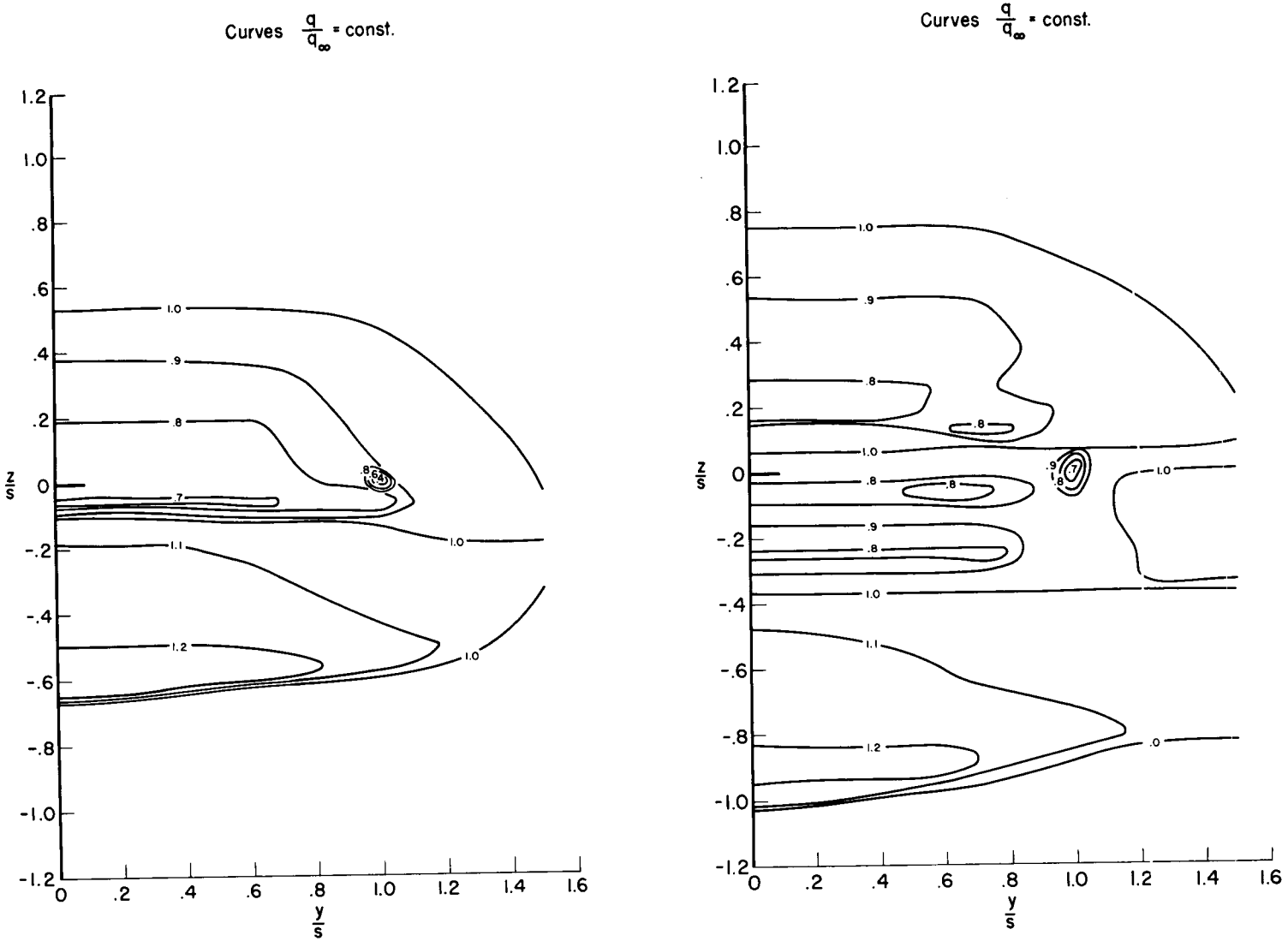

(a) x/c = 0.56

(b) x/c = 1.10

Figure 12.- Contours of constant dynamic-pressure ratio behind rectangular wing; $\alpha = 6^\circ$.

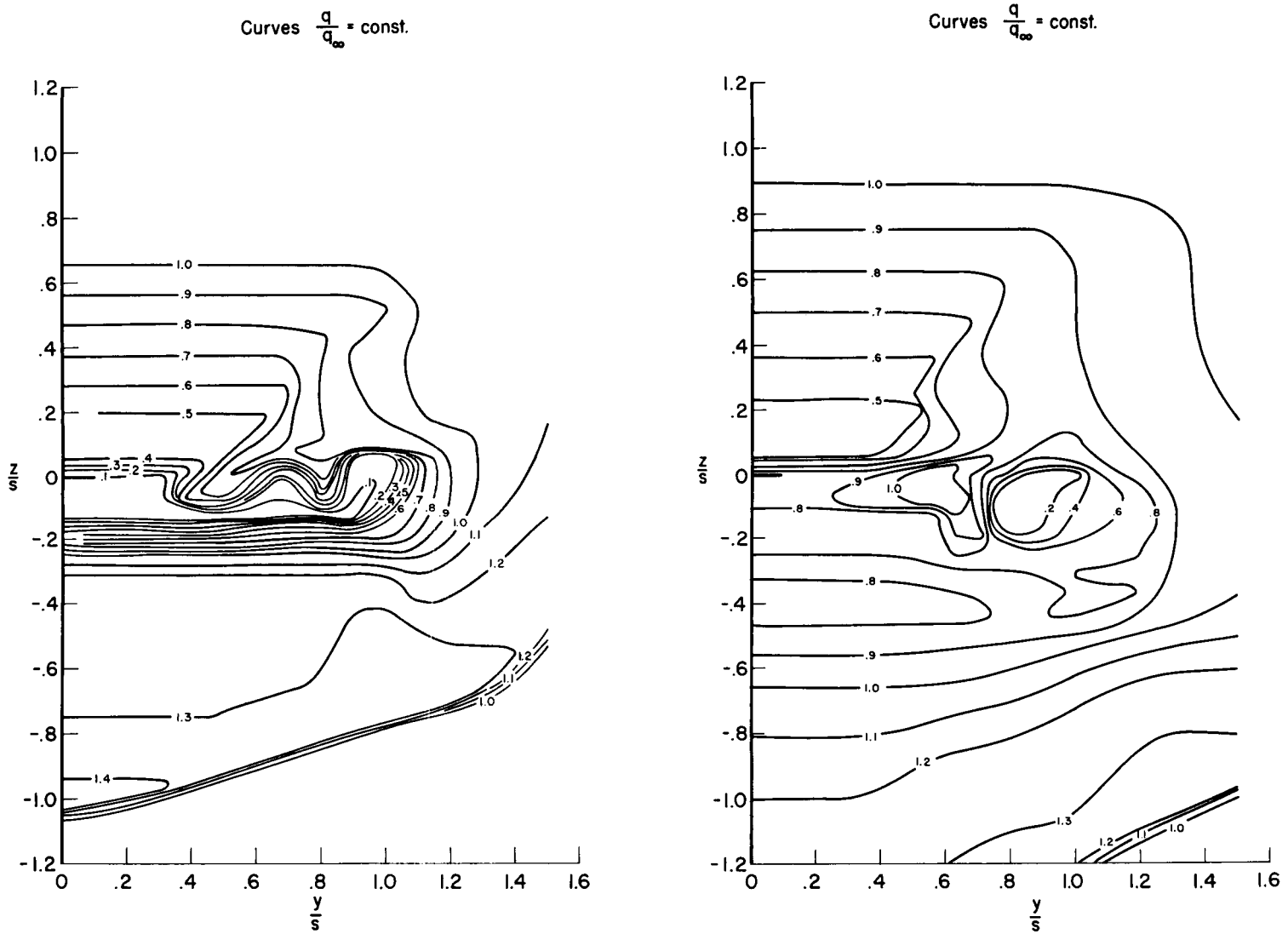

(a) x/c = 0.56

(b) x/c = 1.10

Figure 13.- Contours of constant dynamic-pressure ratio behind rectangular wing; $\alpha = 20^\circ$.

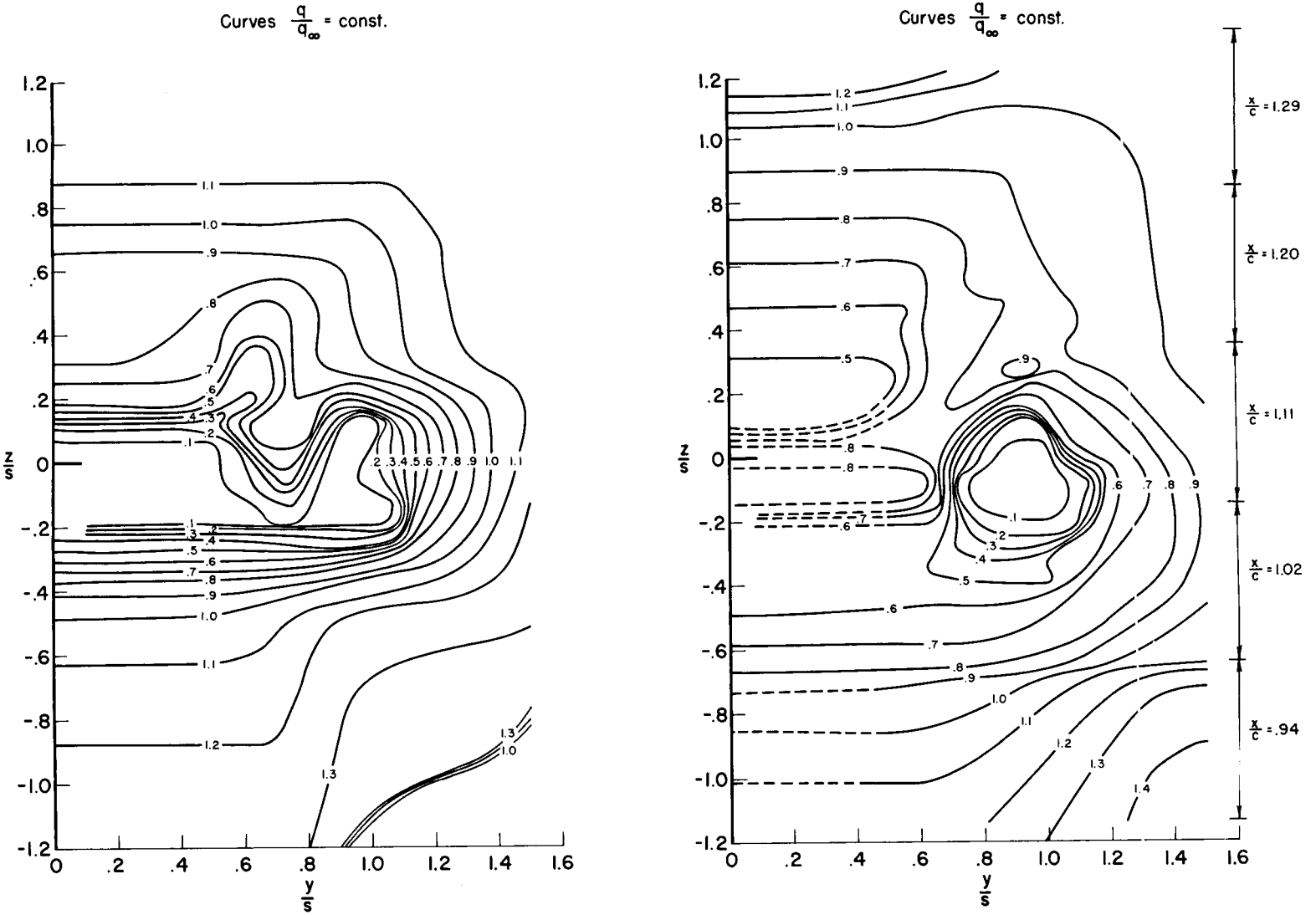

(a) x/c = 0.56 (b) x/c ≈ 1.10

Figure 14.- Contours of constant dynamic-pressure ratio behind rectangular wing; $\alpha = 30^\circ$.

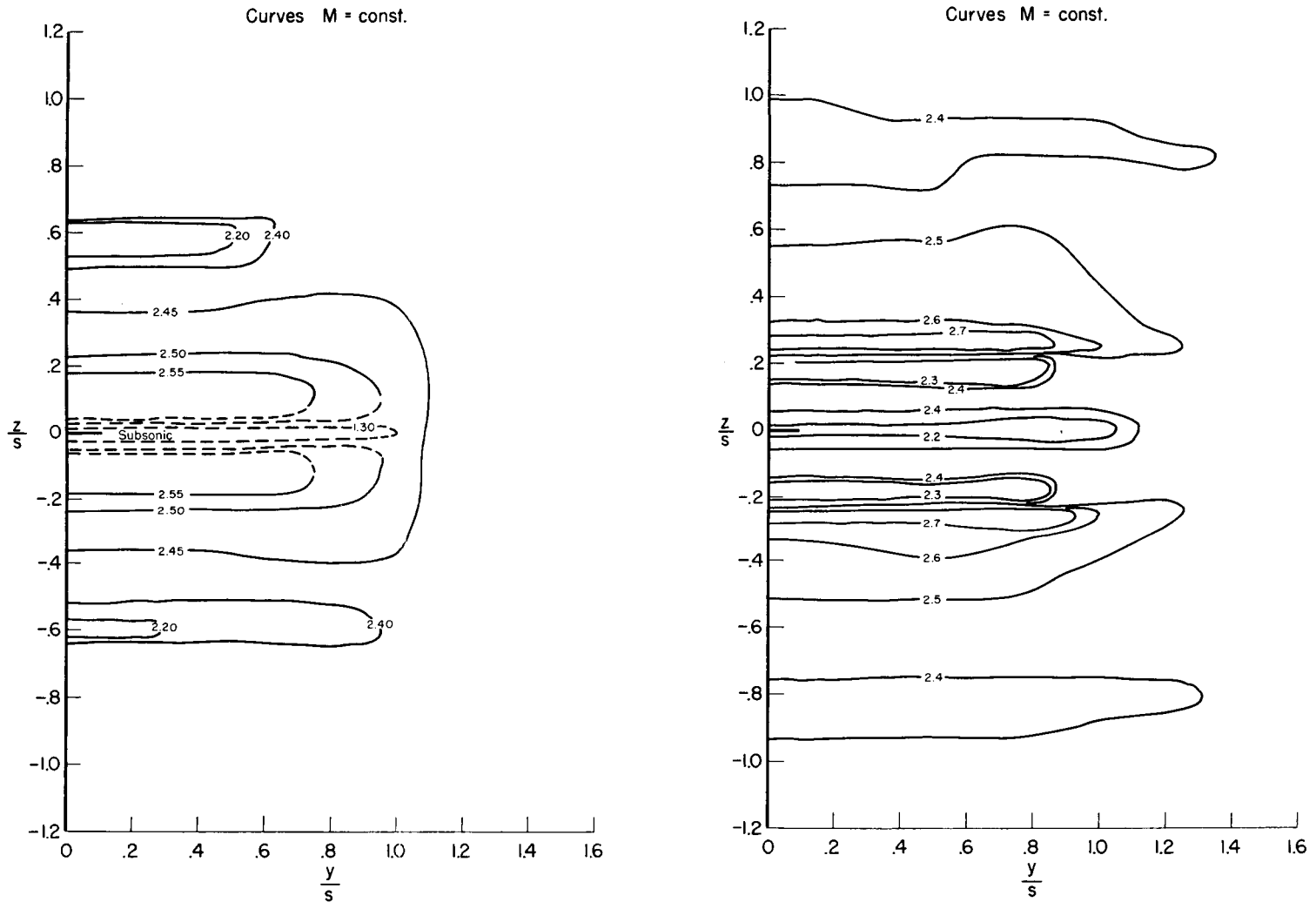

Figure 15.- Contours of constant Mach number behind rectangular wing; $\alpha = 0^{\circ}$.

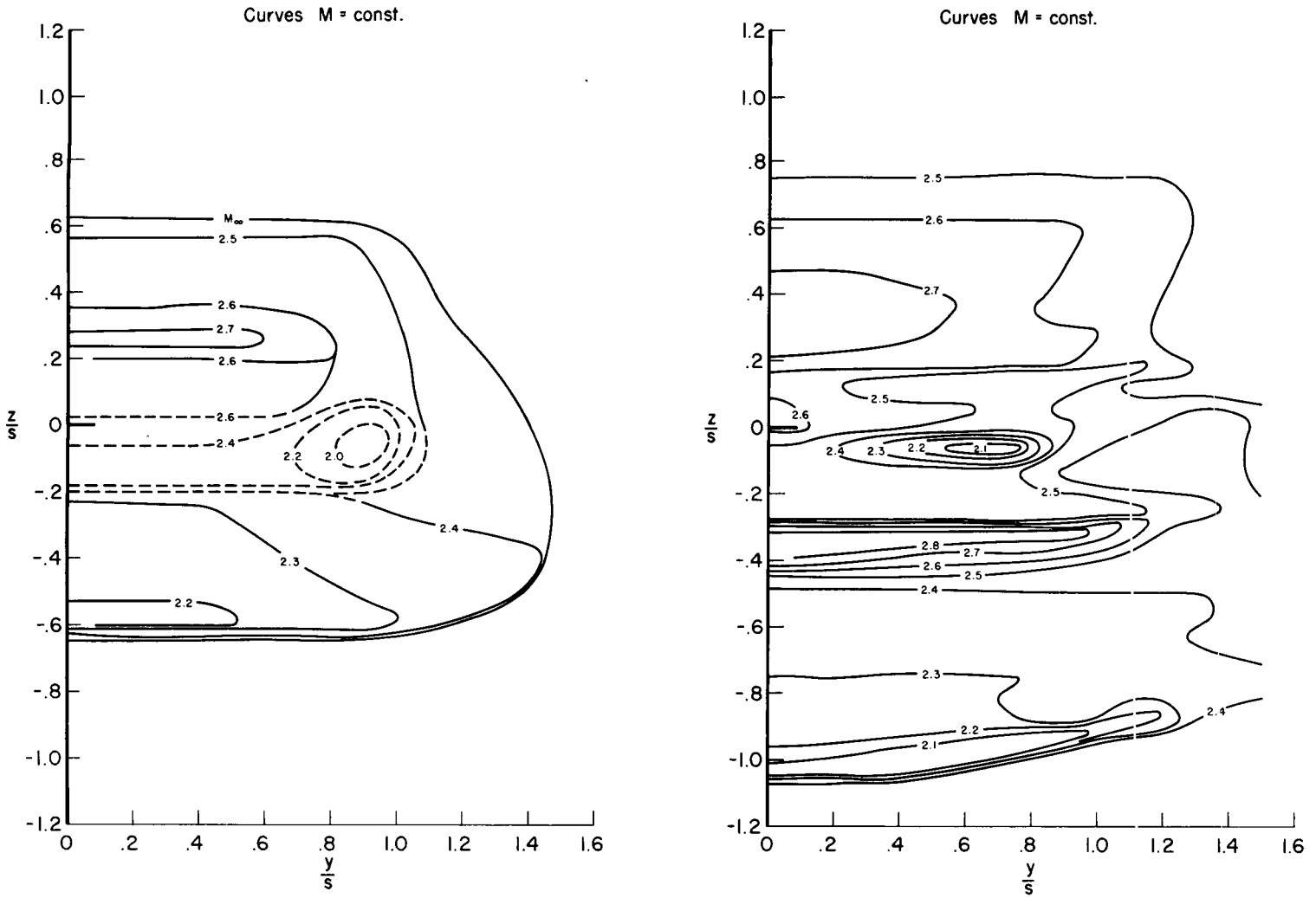

(a) x/c = 0.56

(b) x/c = 1.10

Figure 16.- Contours of constant Mach number behind rectangular wing; $\alpha = 6^{\circ}$.

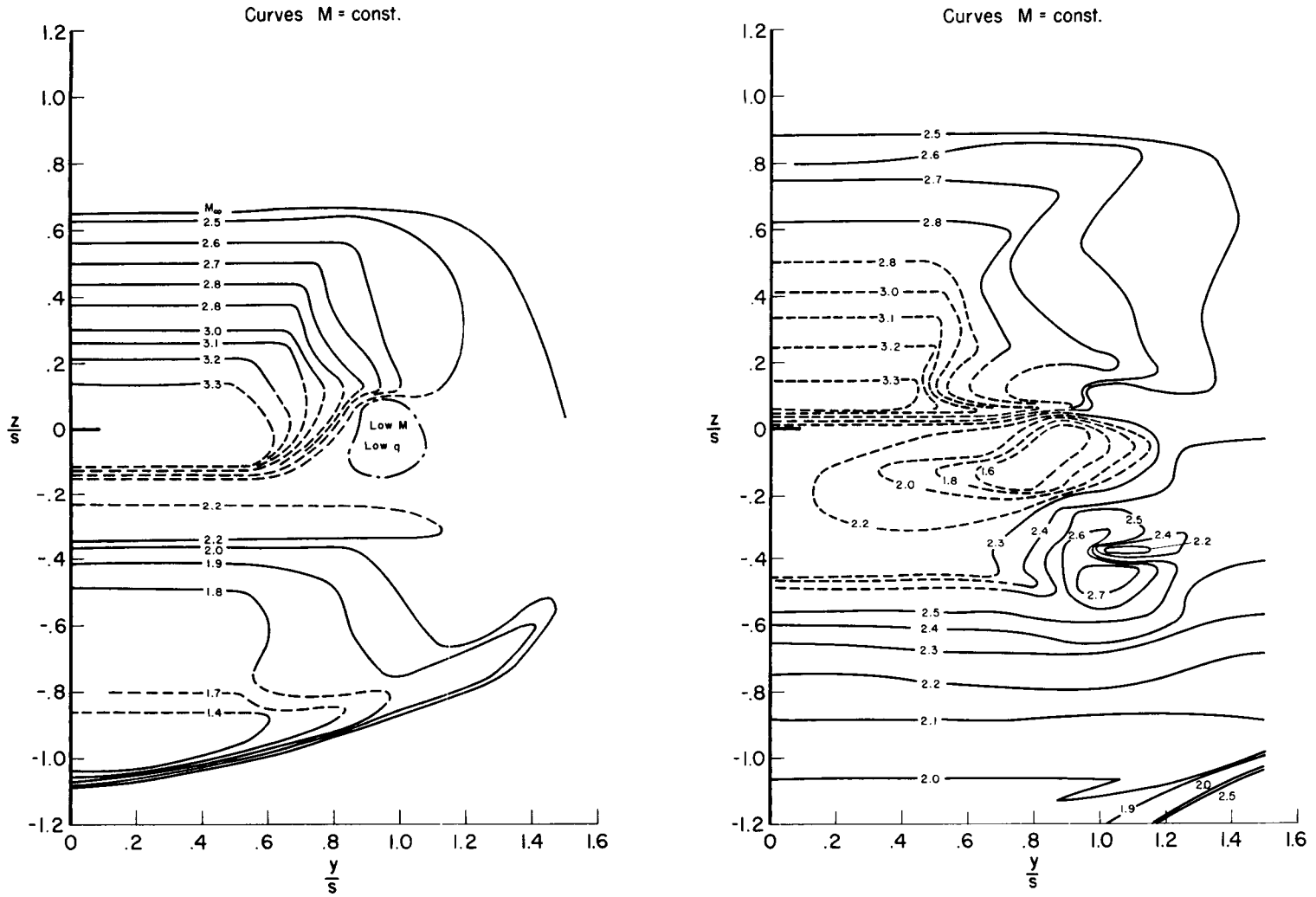

(a) x/c = 0.56

(b) x/c = 1.10

Figure 17.- Contours of constant Mach number behind rectangular wing; $\alpha = 20^{\circ}$.

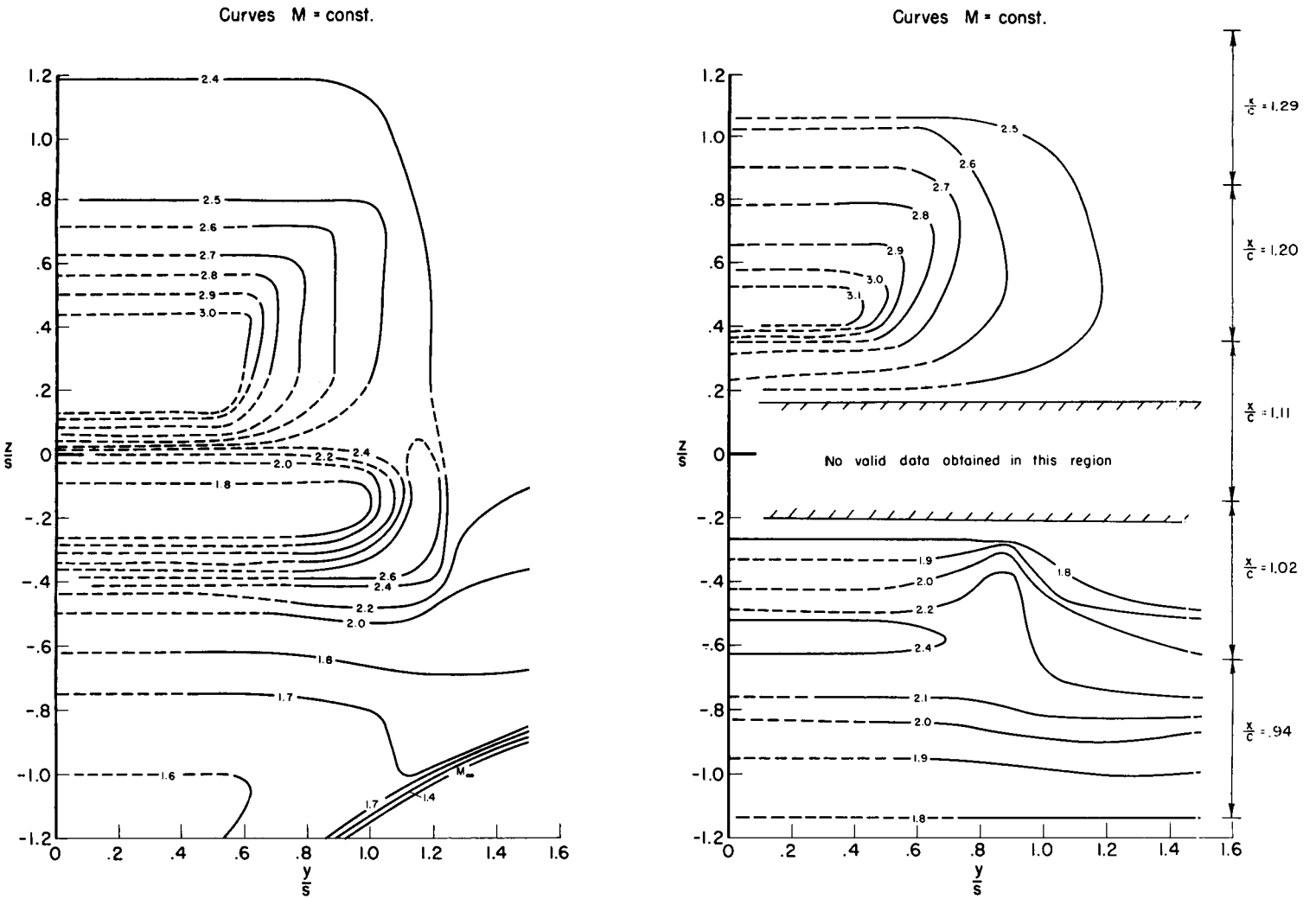

(a) x/c = 0.56

(b) x/c ≈ 1.10

Figure 18.- Contours of constant Mach number behind rectangular wing; $\alpha = 30^{\circ}$.

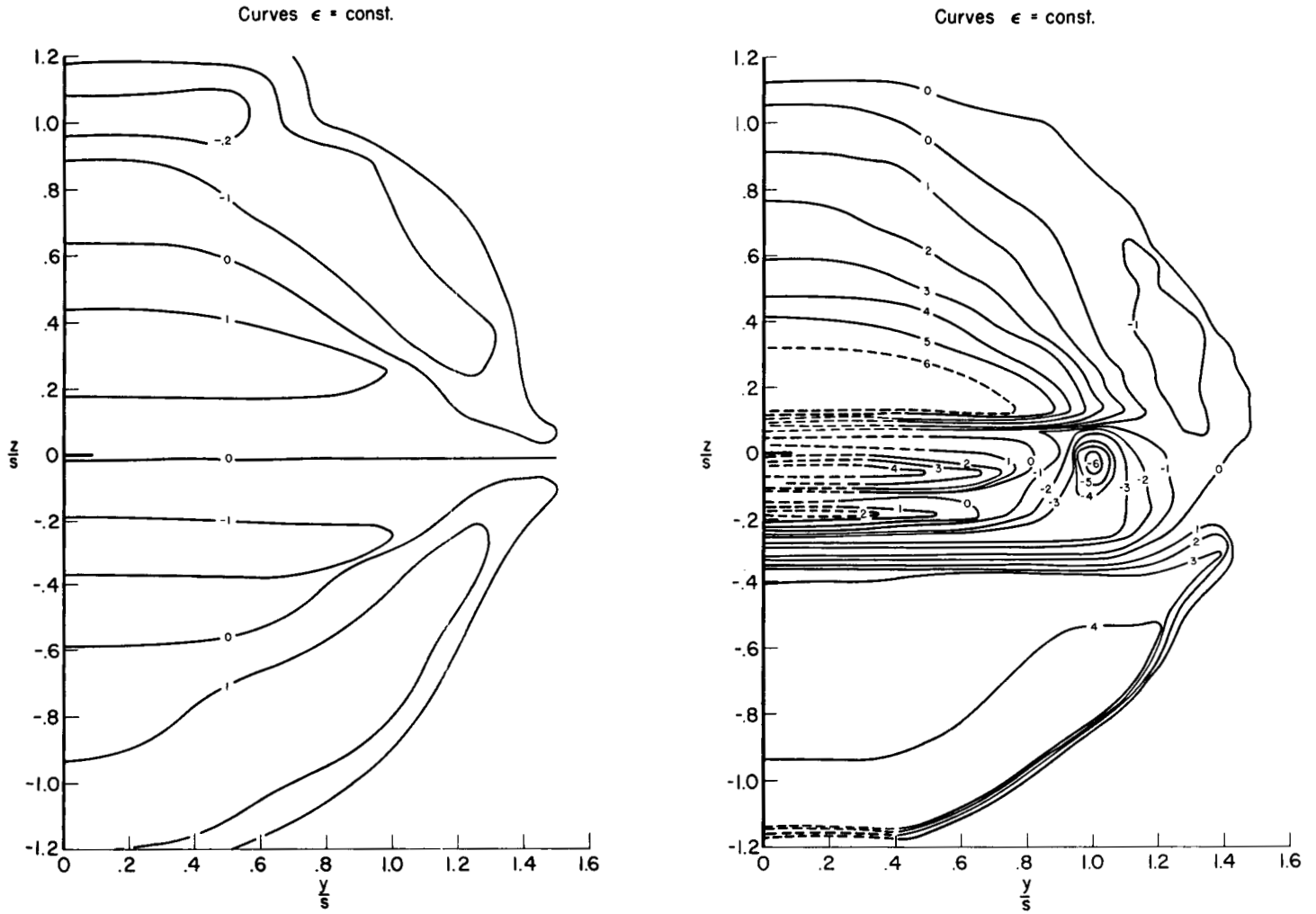

(a) $\alpha = 0^{\circ}$

(b) $\alpha = 6^{\circ}$

Figure 19.- Contours of constant downwash behind triangular wing; x/c = 0.55.

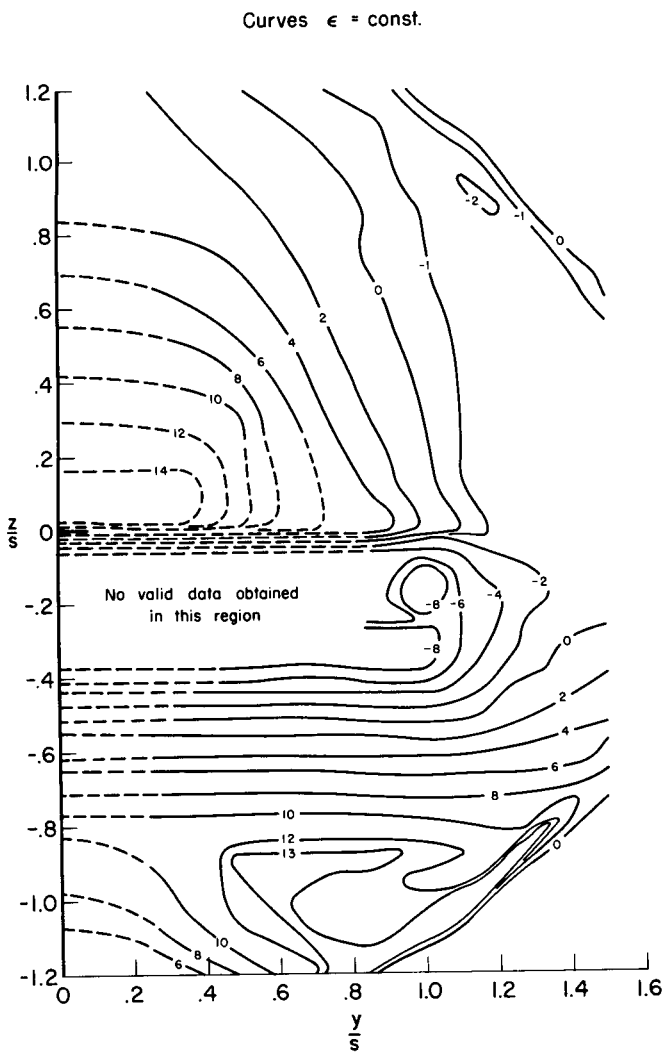

(c) $\alpha = 20^{\circ}$

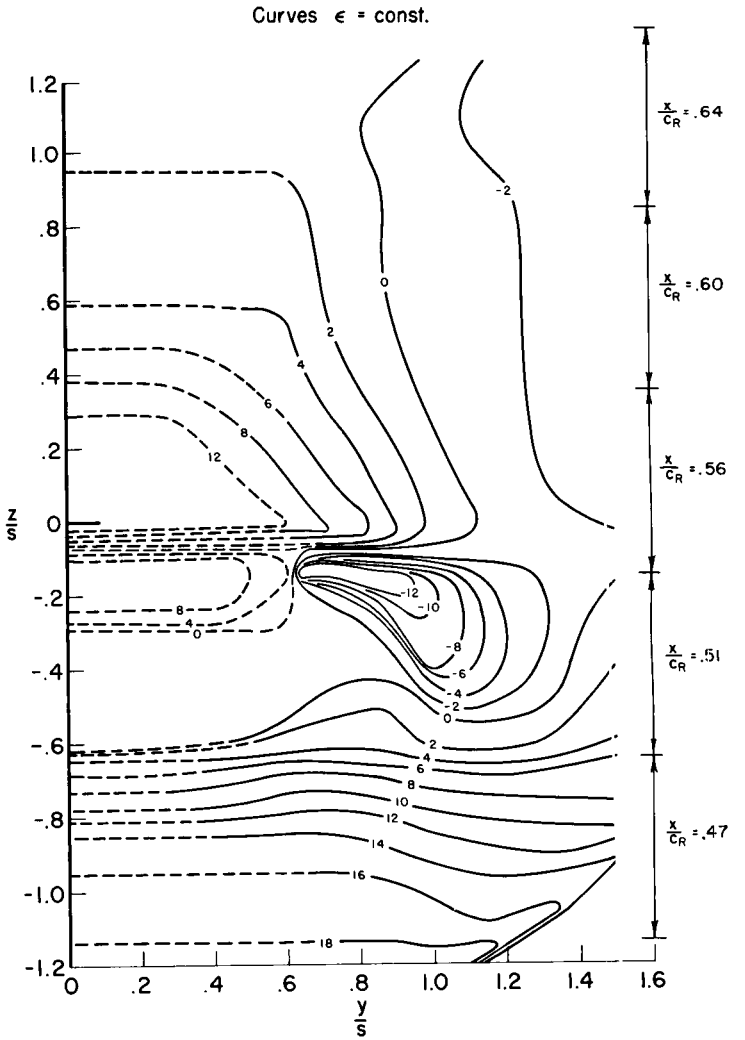

(d) $\alpha = 30^{\circ}$; $x/c_R \approx 0.55$

Figure 19.- Concluded.

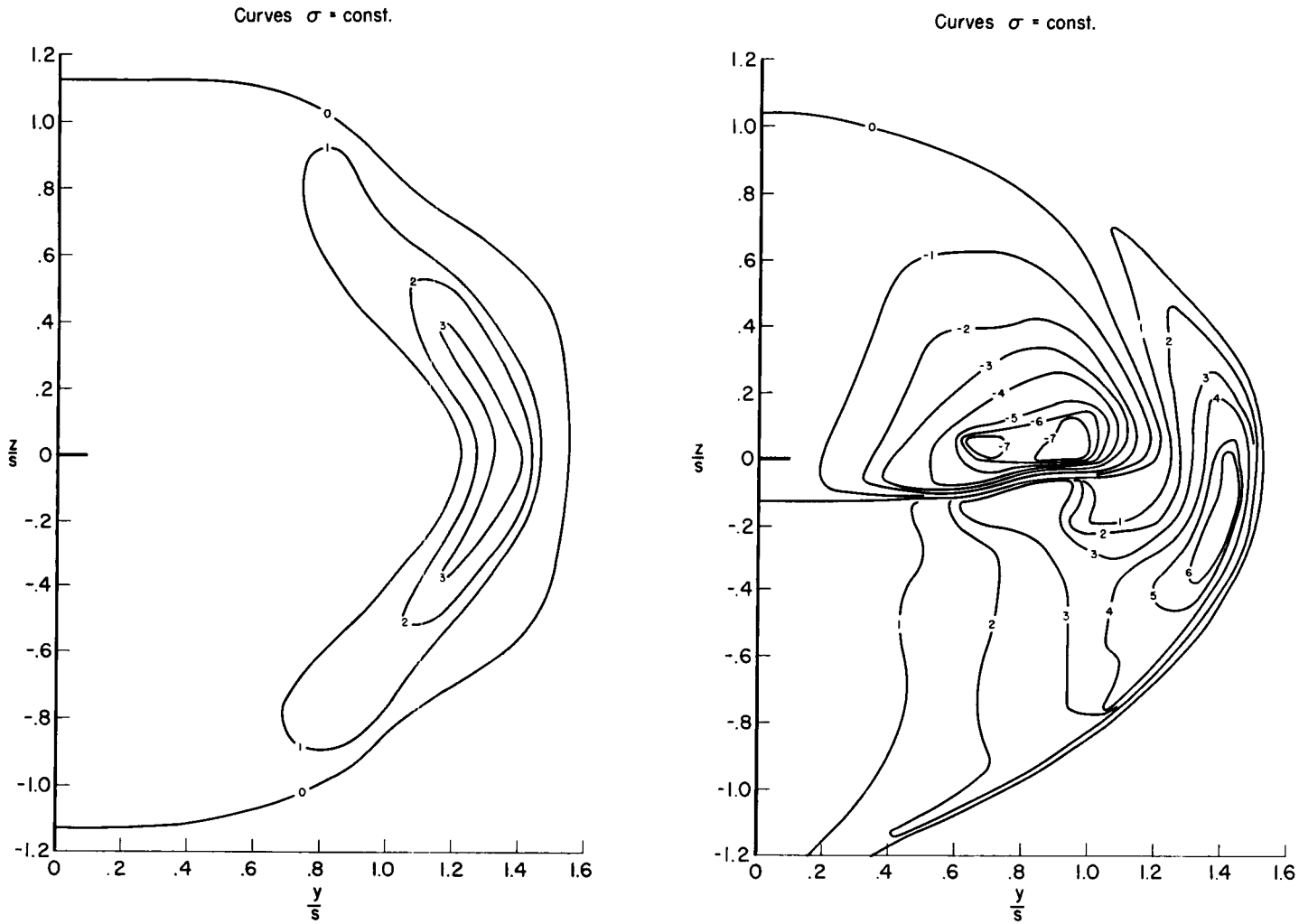

(a) $\alpha = 0^\circ$

(b) $\alpha = 6^\circ$

Figure 20.- Contours of constant sidewash behind triangular wing; $x/c_R = 0.55$.

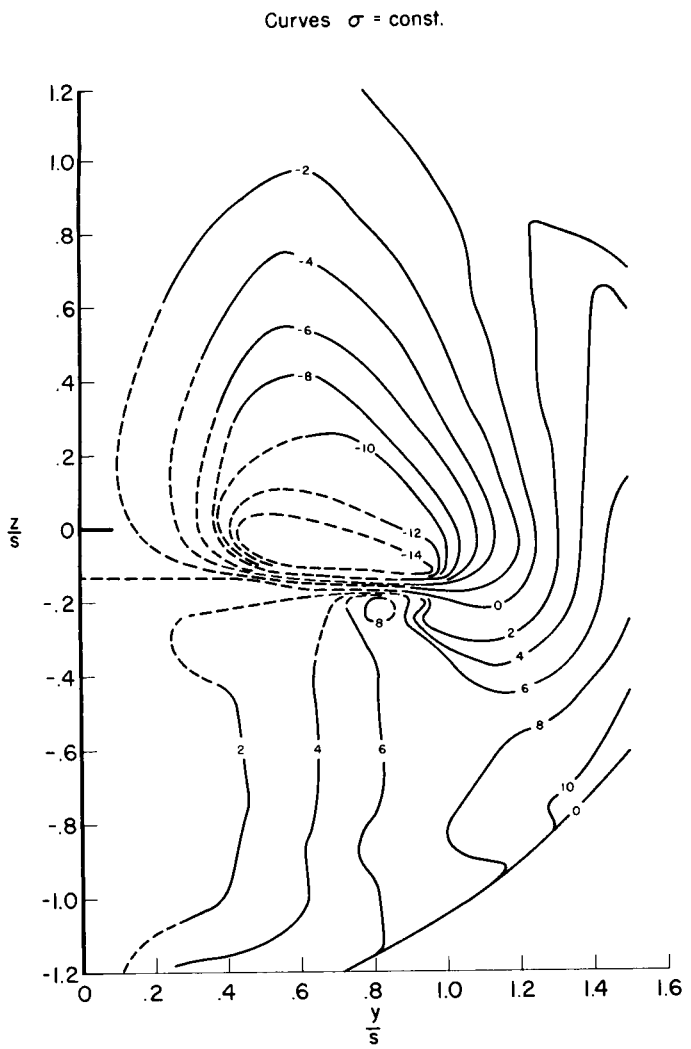

(c) $\alpha = 20^{\circ}$

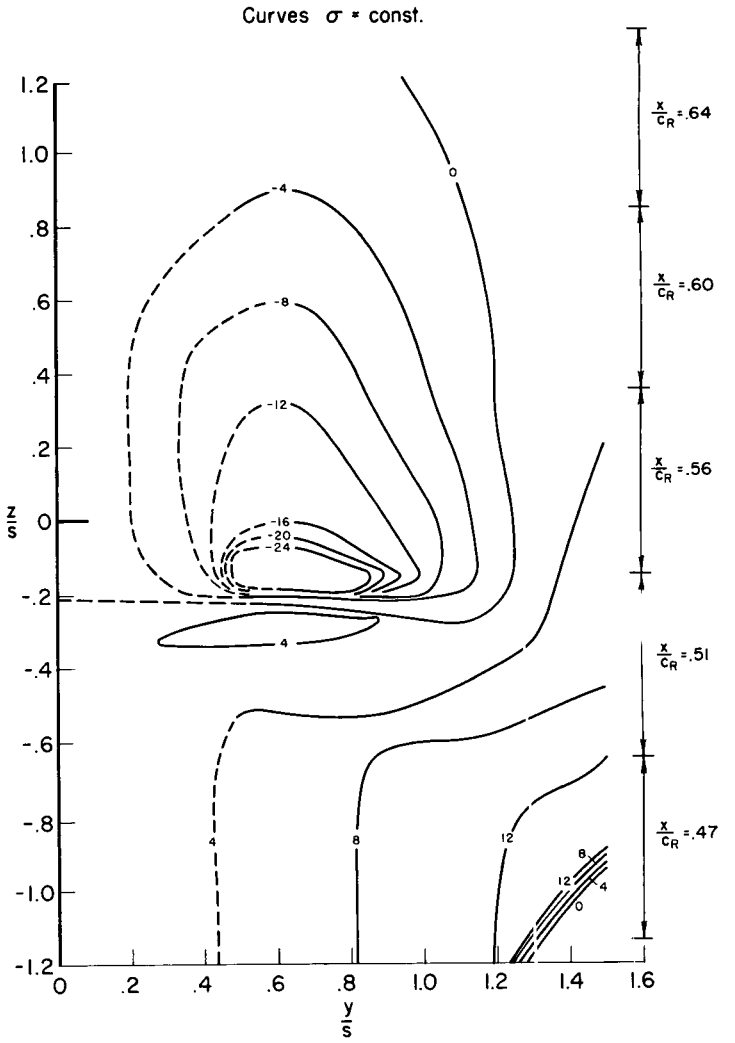

(d) $\alpha = 30^{\circ}$; $x/c_R \approx 0.55$

Figure 20.- Concluded.

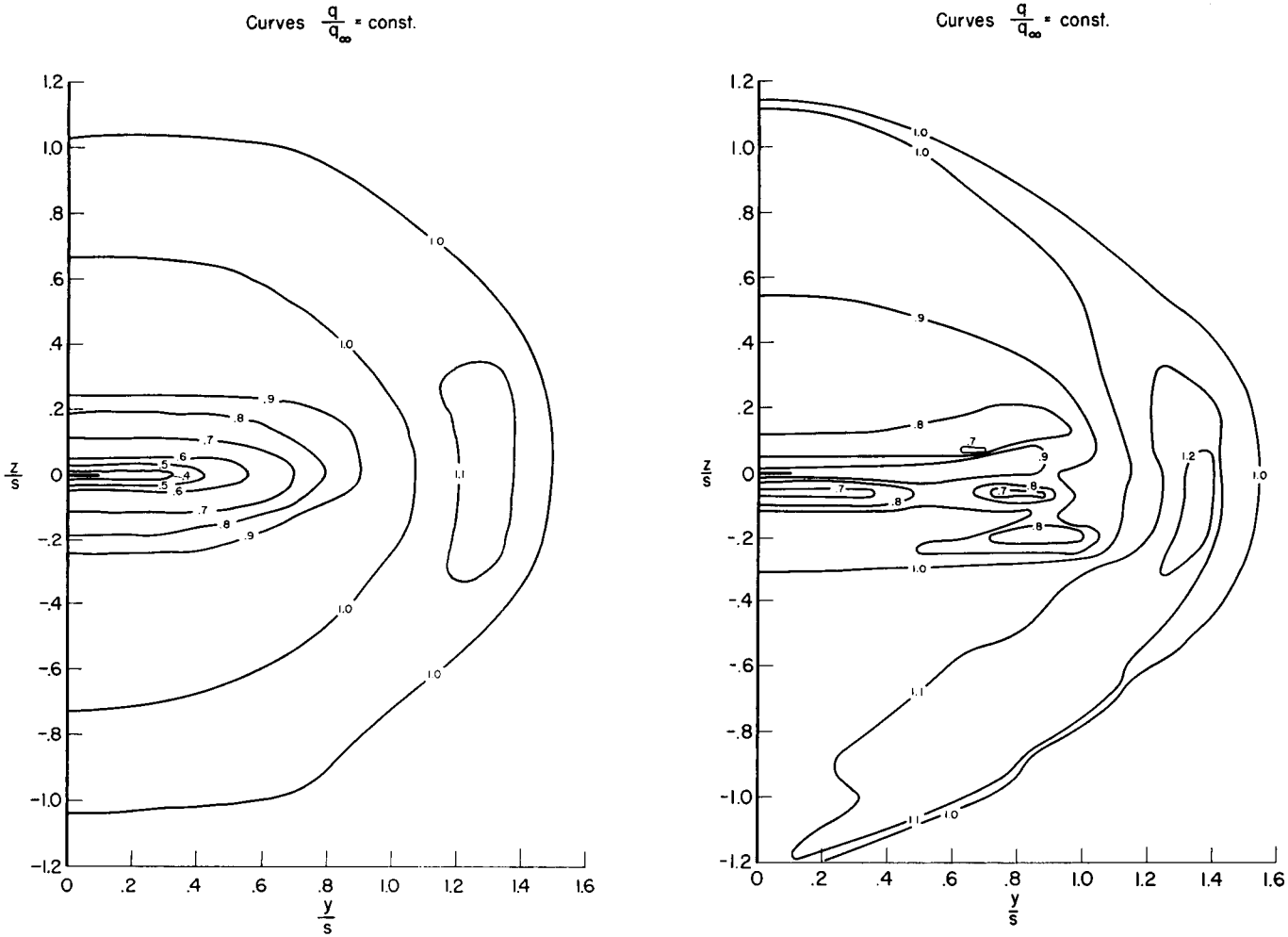

(a) $\alpha = 0^\circ$ (b) $\alpha = 6^\circ$

Figure 21.- Contours of constant dynamic-pressure ratio behind triangular wing; $x/c_R = 0.55$.

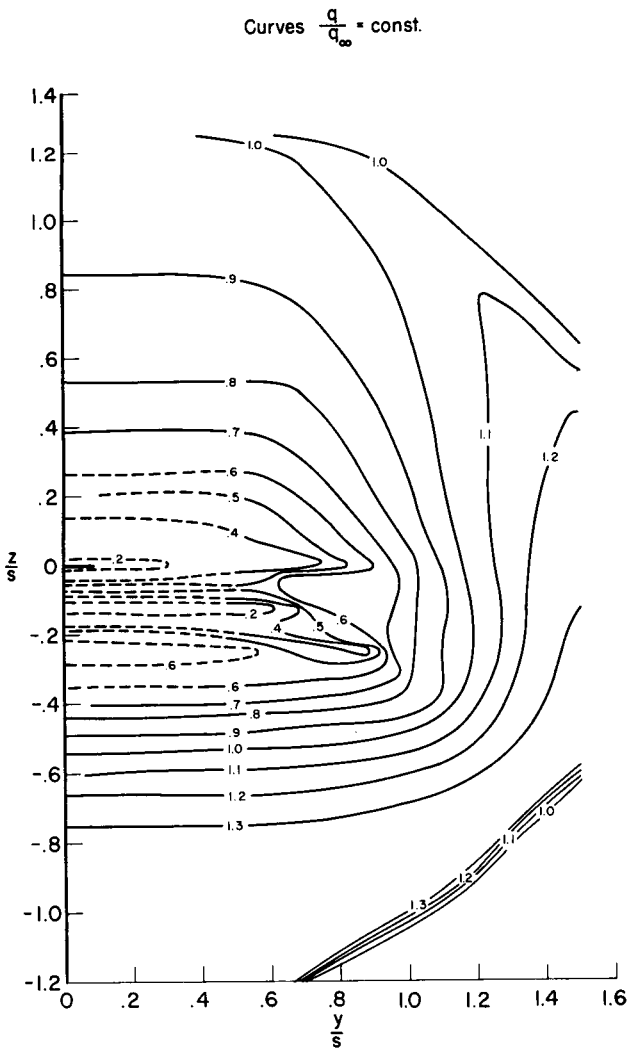

(c) $\alpha = 20^\circ$

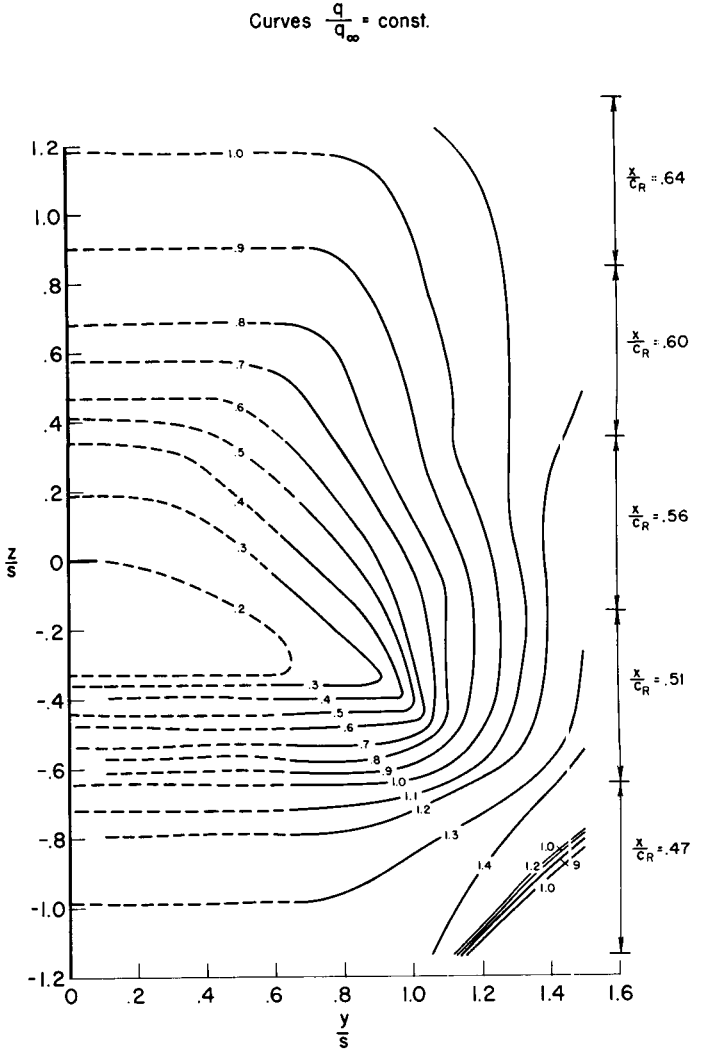

(d) $\alpha = 30^\circ$; $x/c_R \approx 0.55$.

Figure 21.- Concluded.

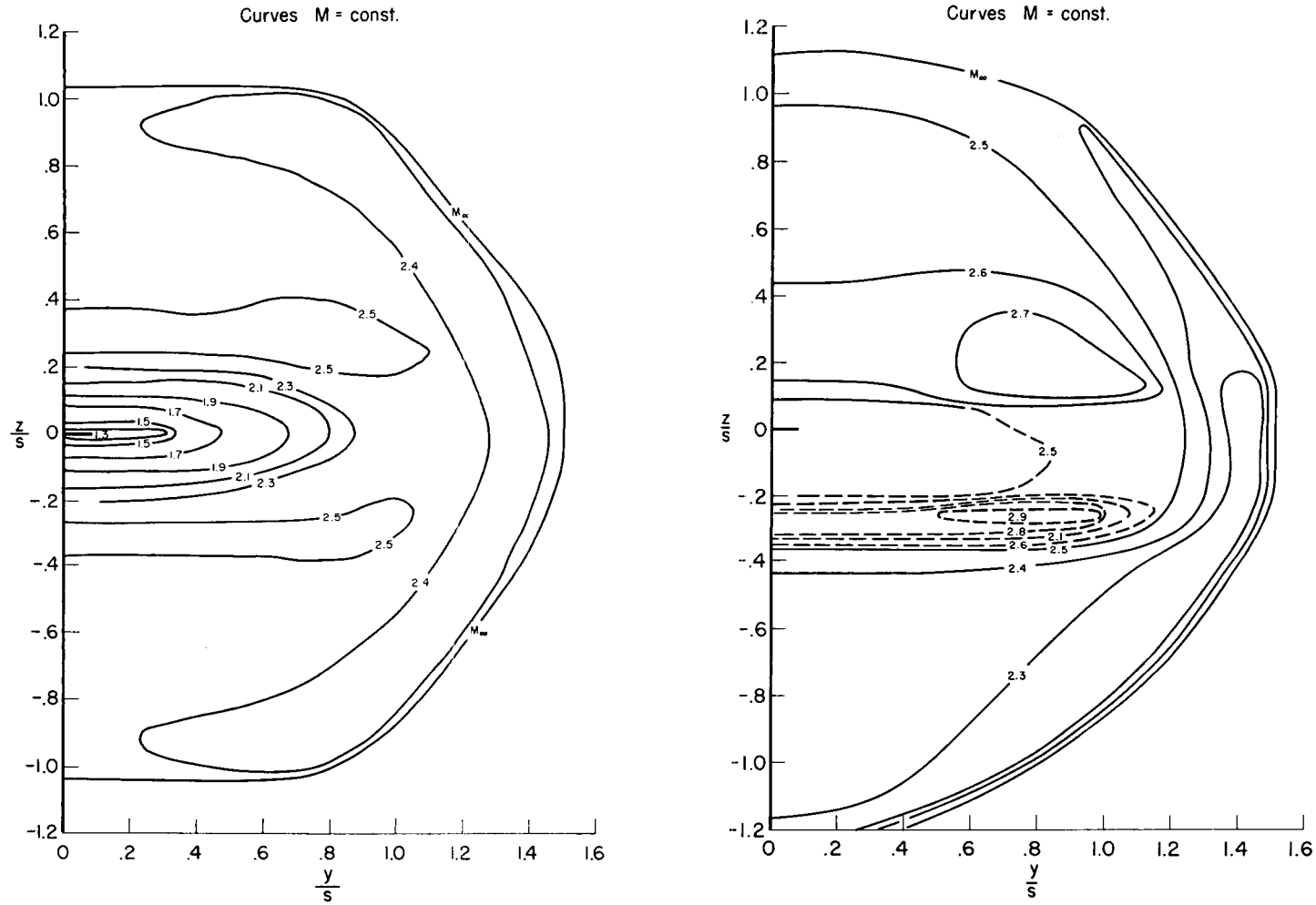

(a) $\alpha = 0^{\circ}$ (b) $\alpha = 6^{\circ}$

Figure 22.- Contours of constant Mach number behind triangular wing; $x/c_R = 0.55$.

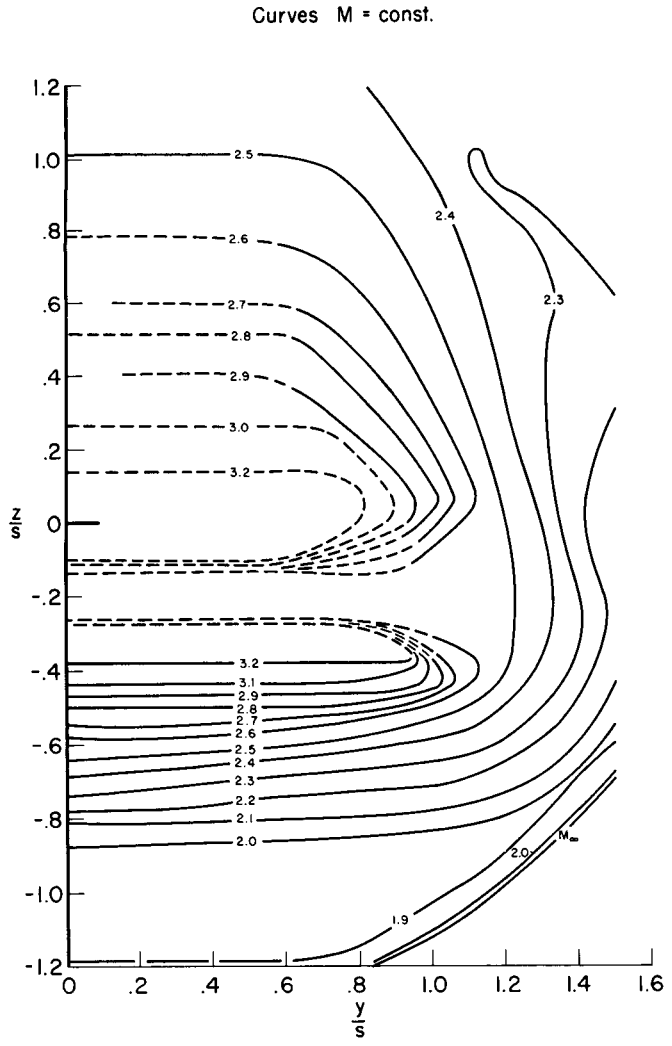

(c) $\alpha = 20^{\circ}$

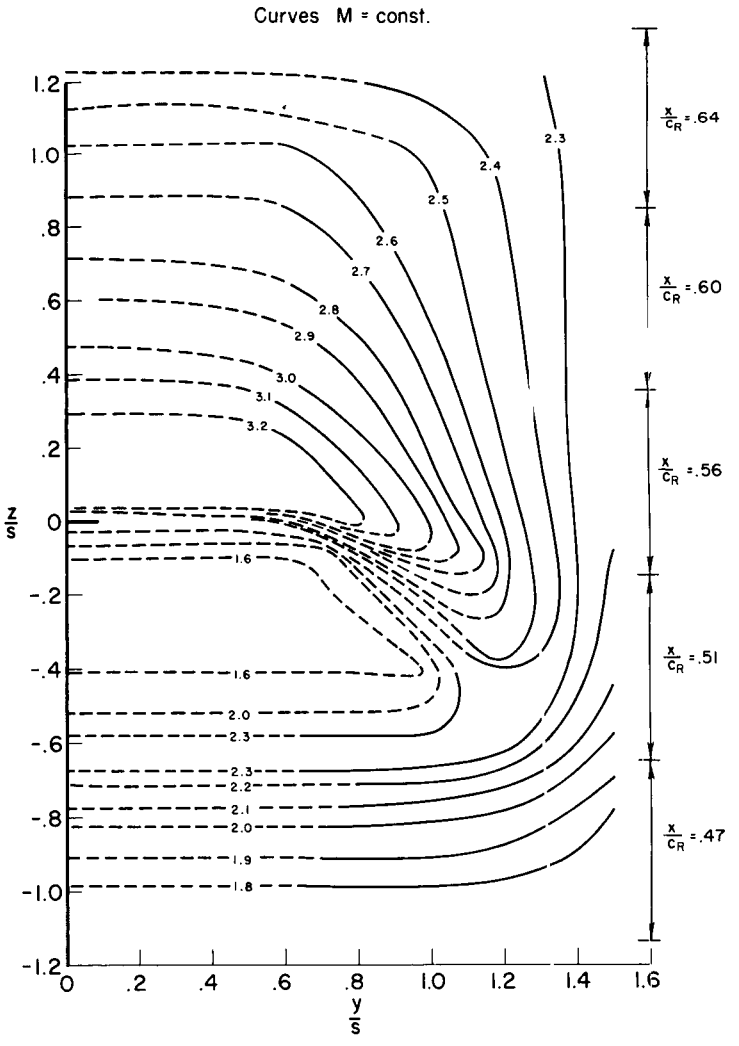

(d) $\alpha = 30^{\circ}$ $x/c_R \approx 0.55$

Figure 22.- Concluded.

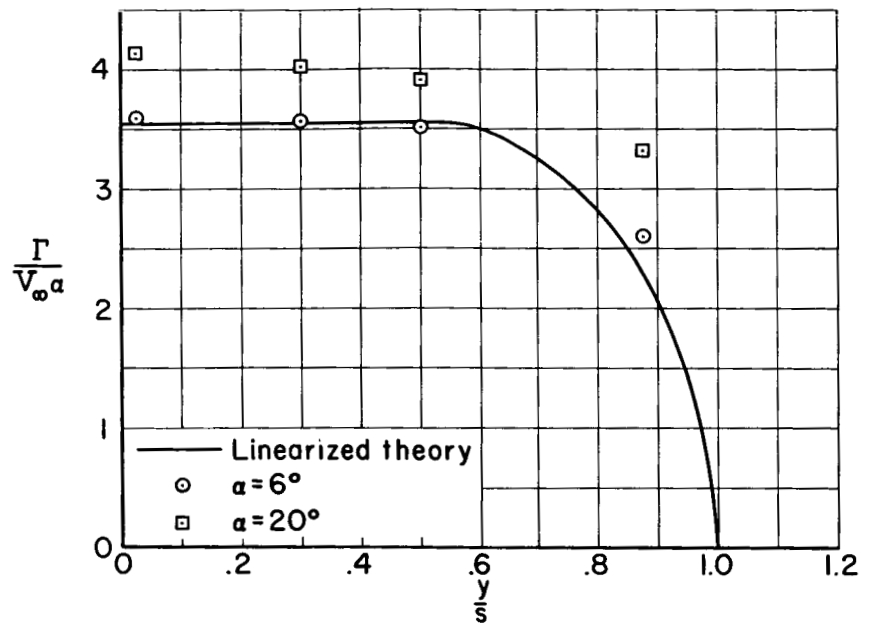

(a) Rectangular wing.

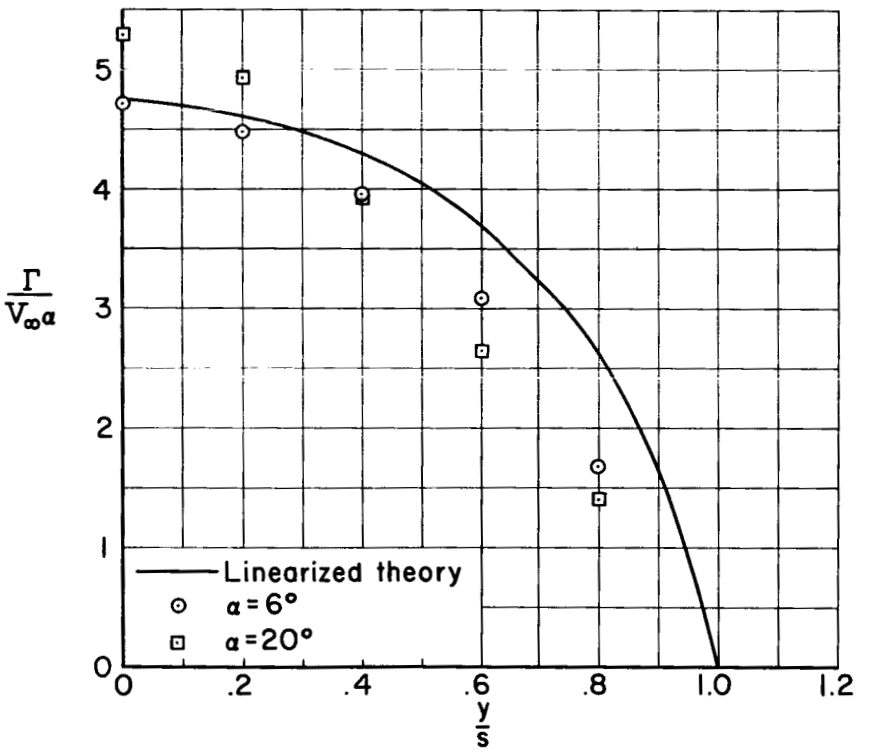

(b) Triangular wing.

Figure 23.- Comparison of experimental and theoretical span loading.

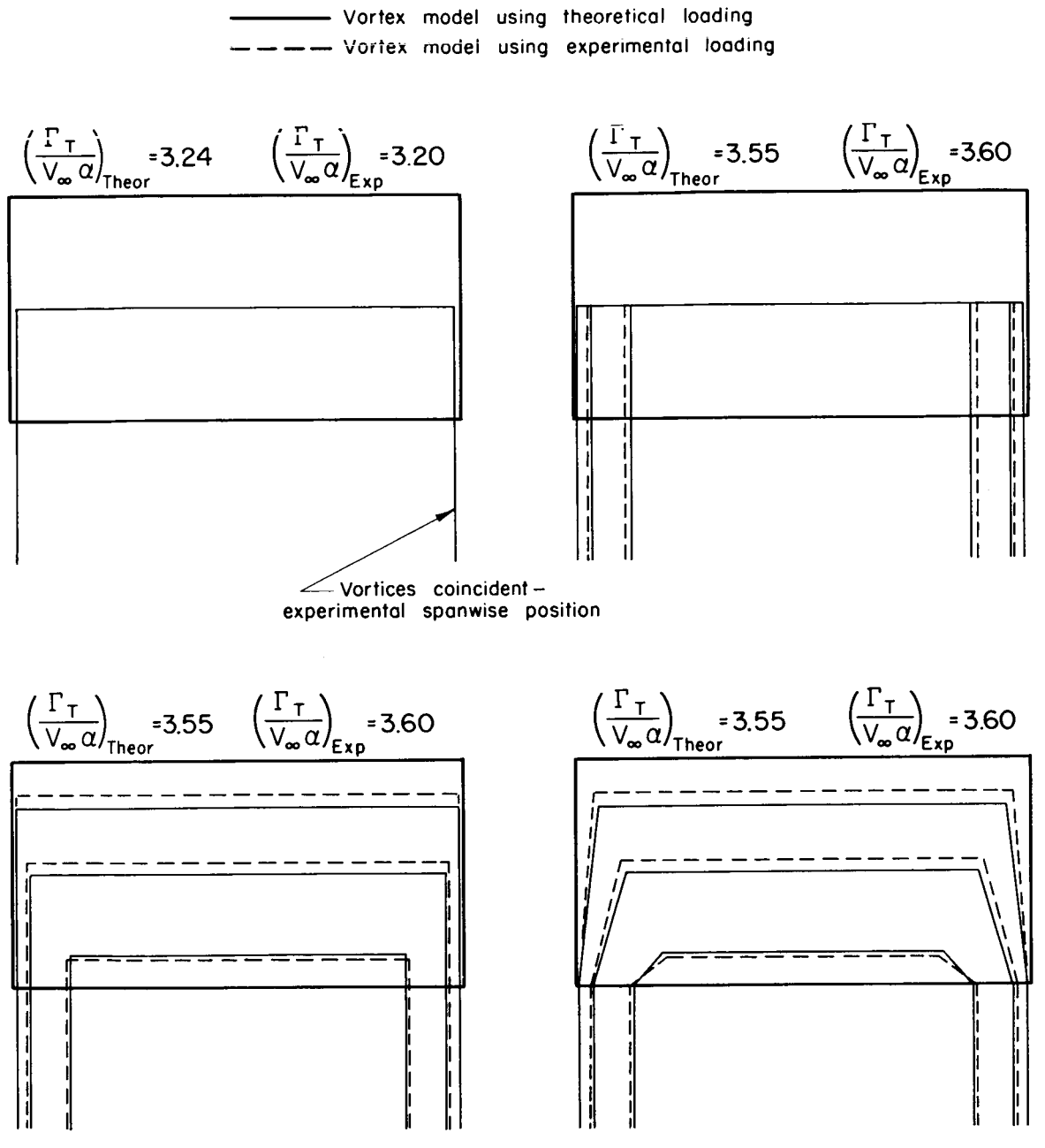

(a) $\alpha = 6^\circ$

Figure 24.- Comparison of vortex models obtained using theoretical and experimental span loading; rectangular wing.

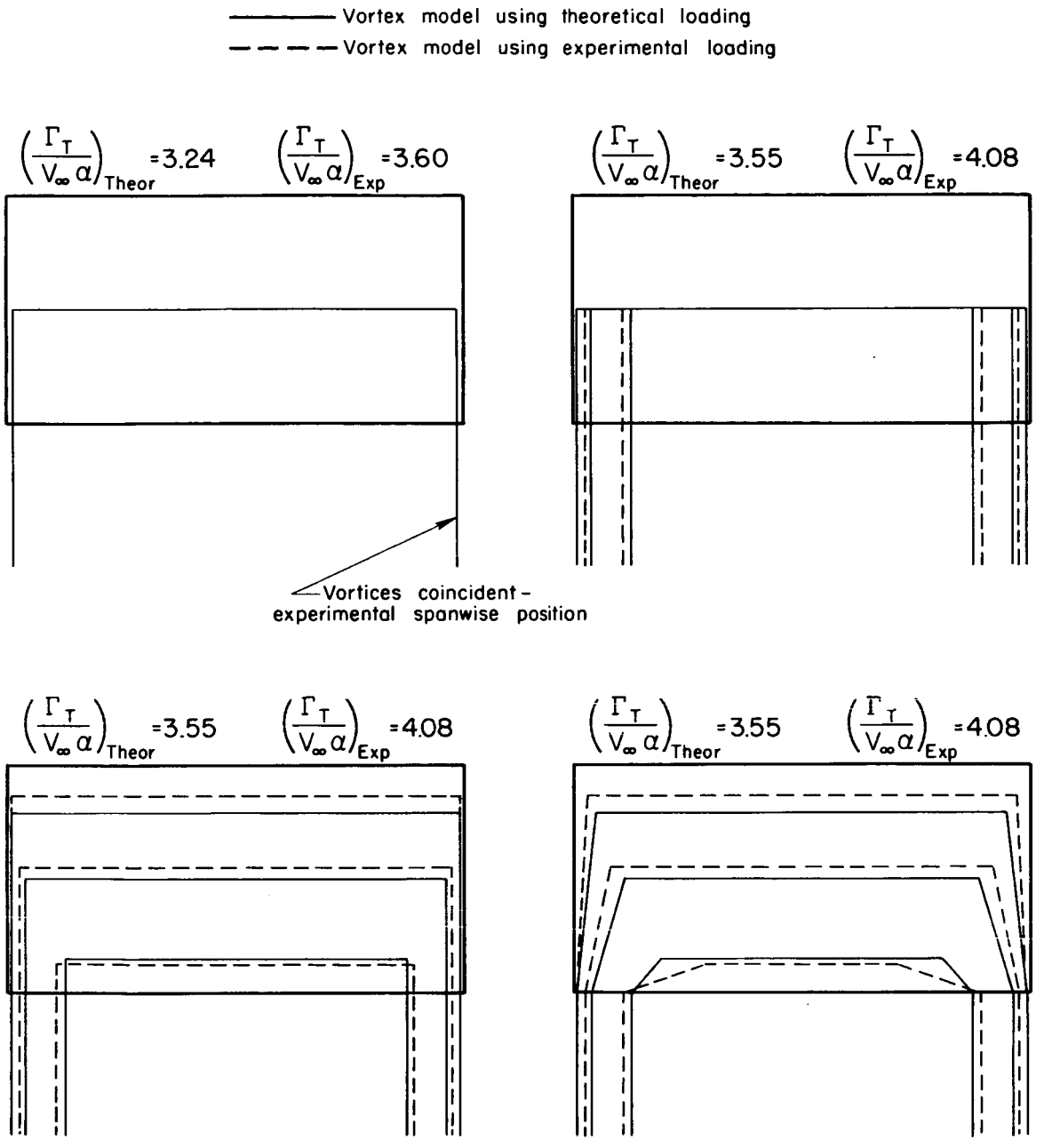

(b) $\alpha = 20^\circ$

Figure 24.- Concluded.

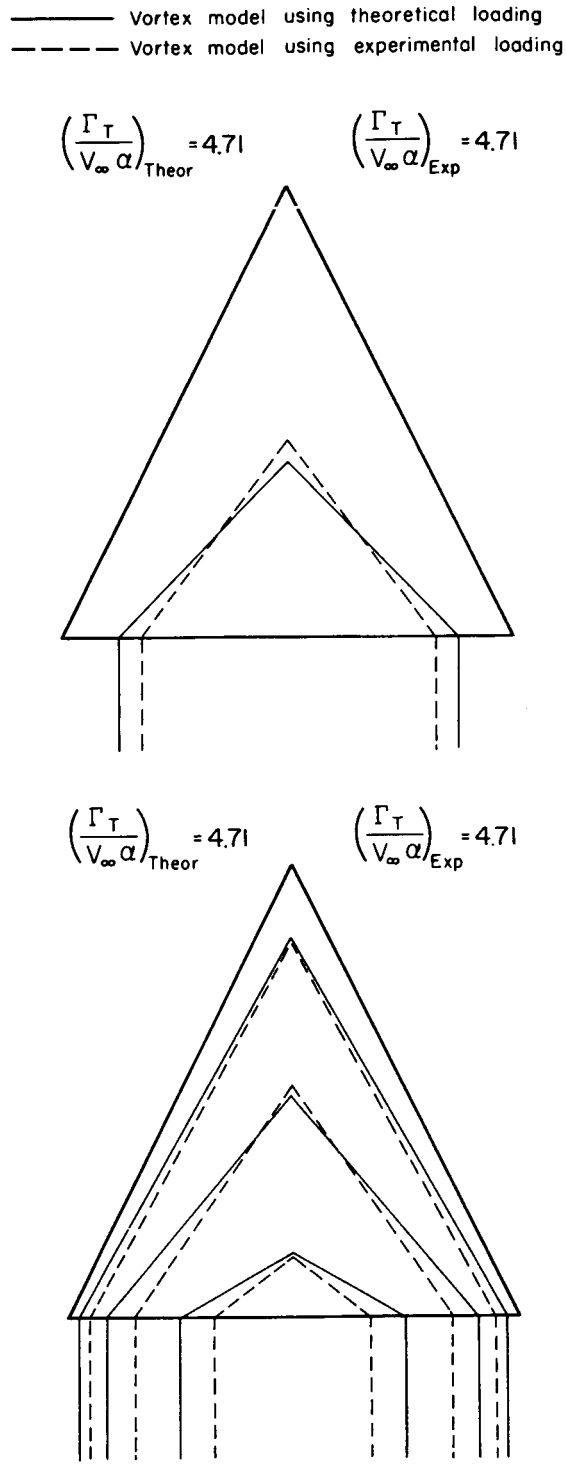

Figure 25.- Comparison of vortex models obtained using theoretical and experimental span loading; triangular wing; $\alpha = 6^{\circ}$.

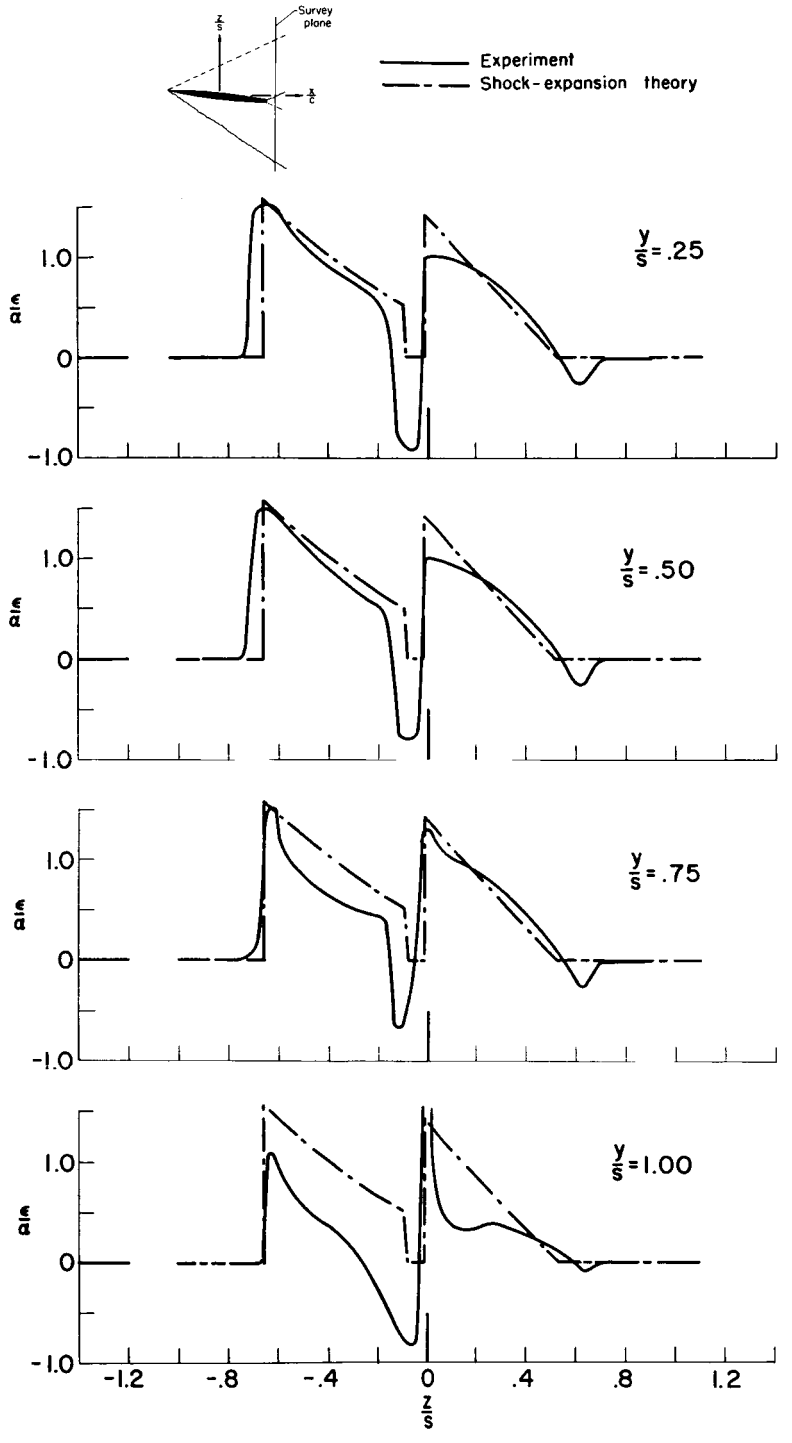

(a) x/c = 0.56

Figure 26.- Comparison of measured downwash behind rectangular wing with shock-expansion theory; $\alpha = 6^{\circ}$.

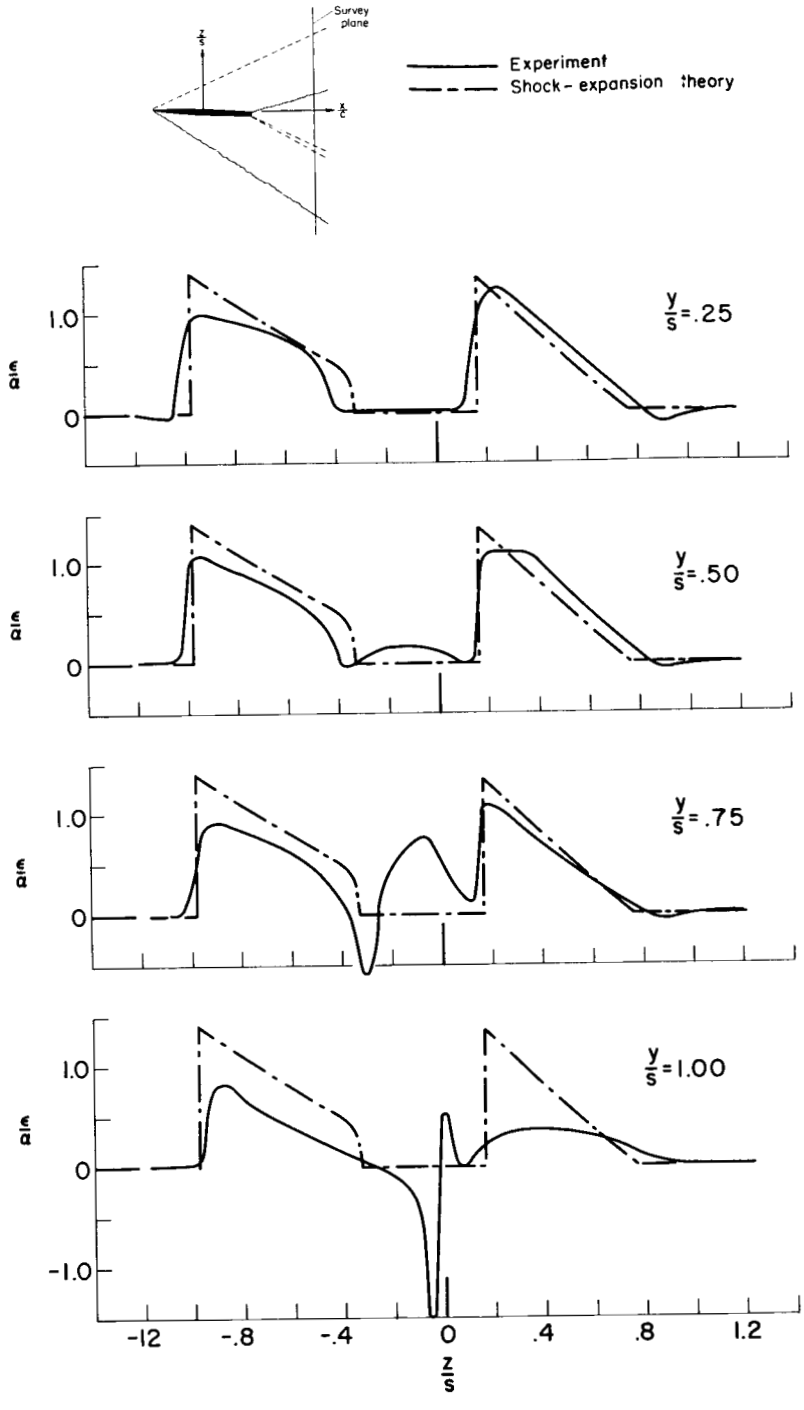

(b) x/c = 1.10

Figure 26.- Concluded.

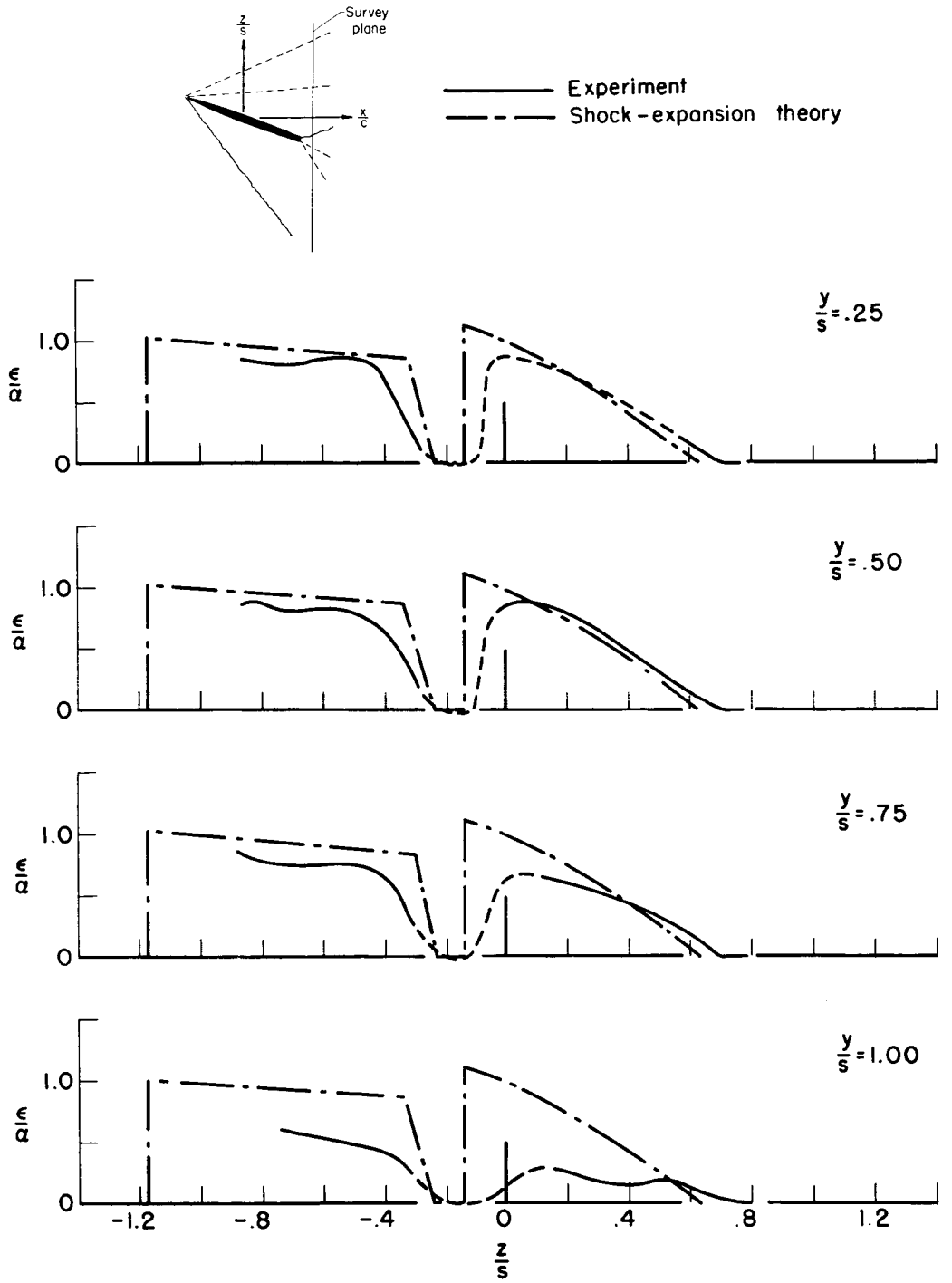

(a) x/c = 0.56

Figure 27.- Comparison of measured downwash behind rectangular wing with shock-expansion theory; $\alpha = 20^{\circ}$.

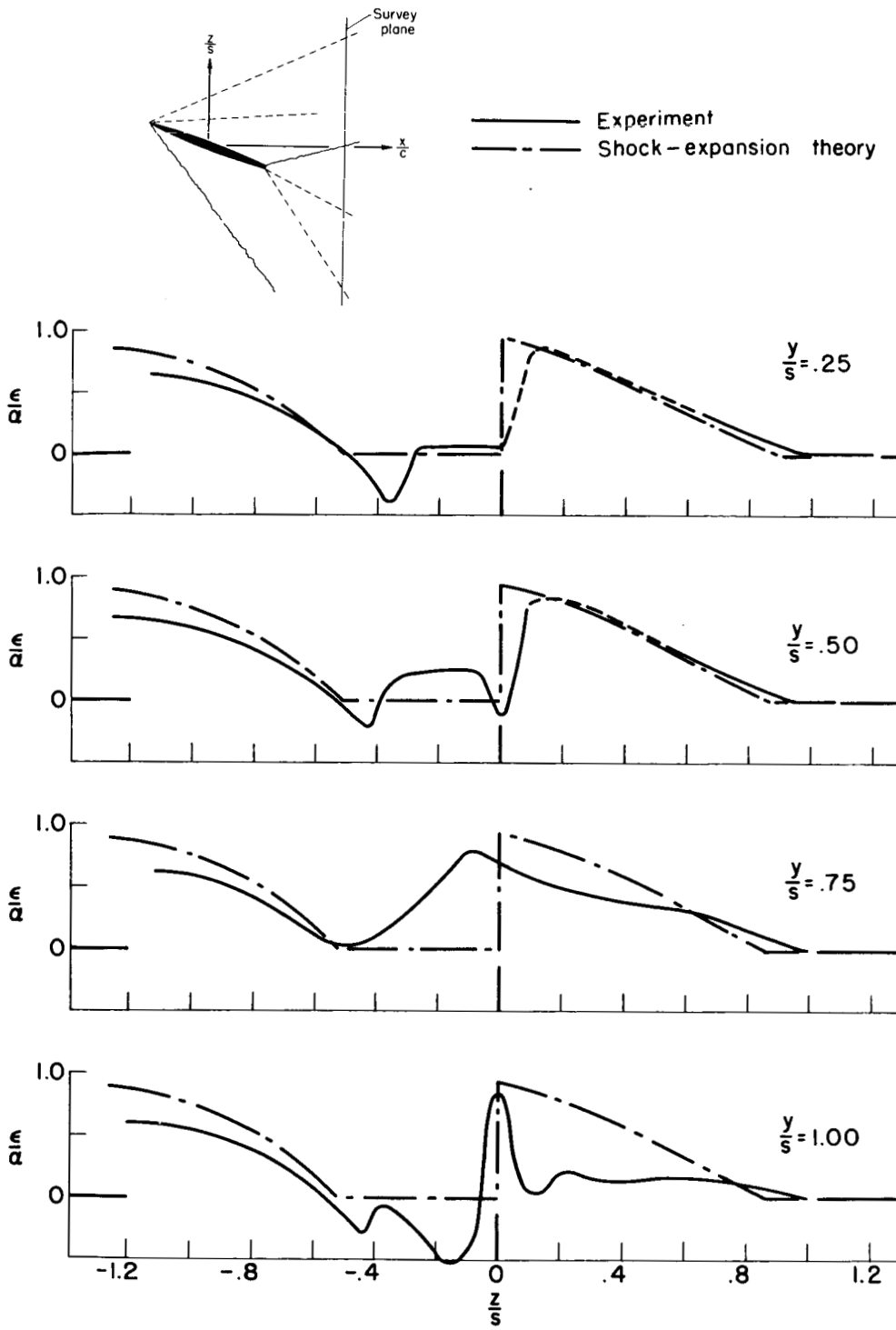

(b) x/c = 1.10

Figure 27.- Concluded.

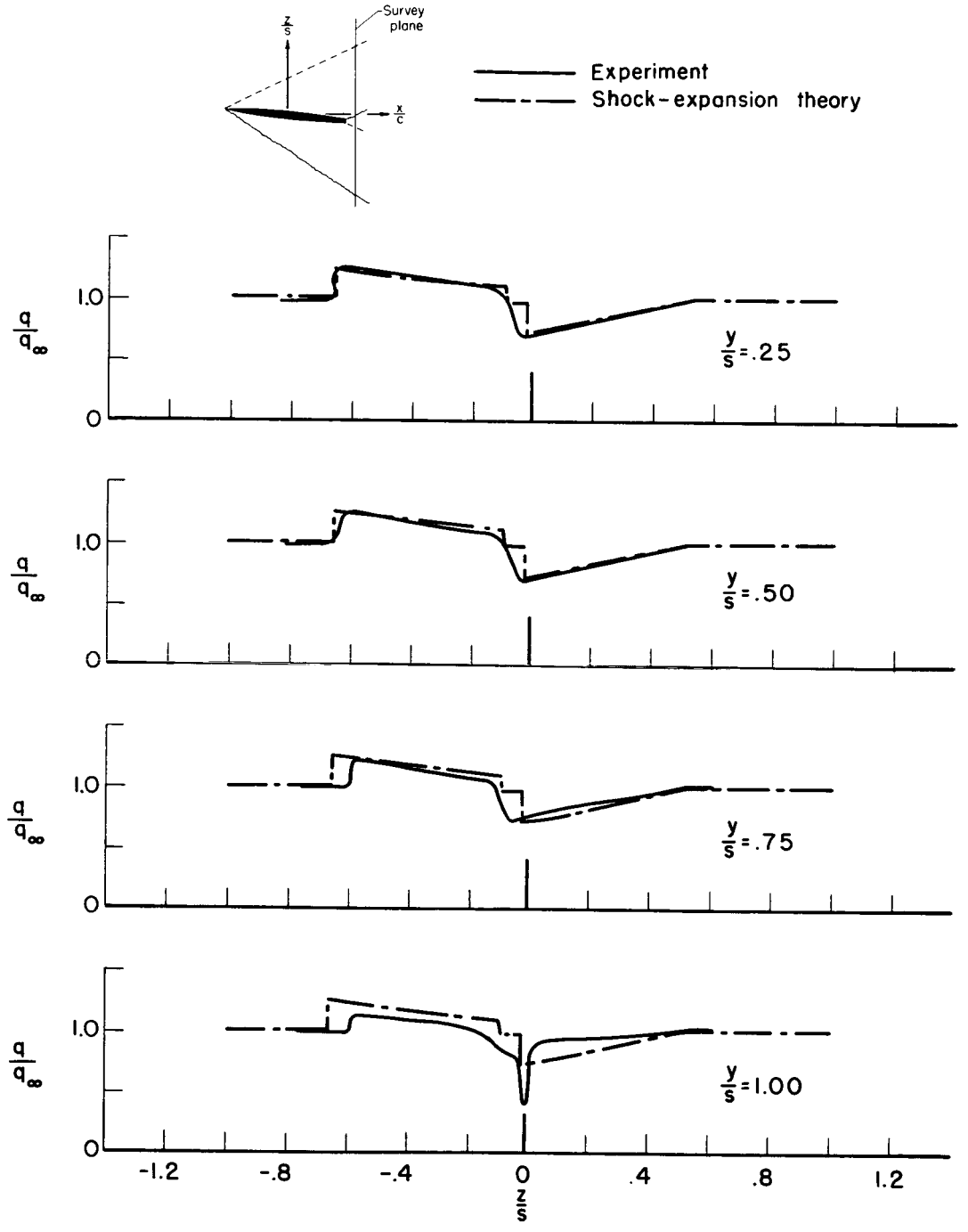

(a) x/c = 0.56

Figure 28.- Comparison of measured dynamic pressure behind rectangular wing with shock-expansion theory; $\alpha = 6^{\circ}$.

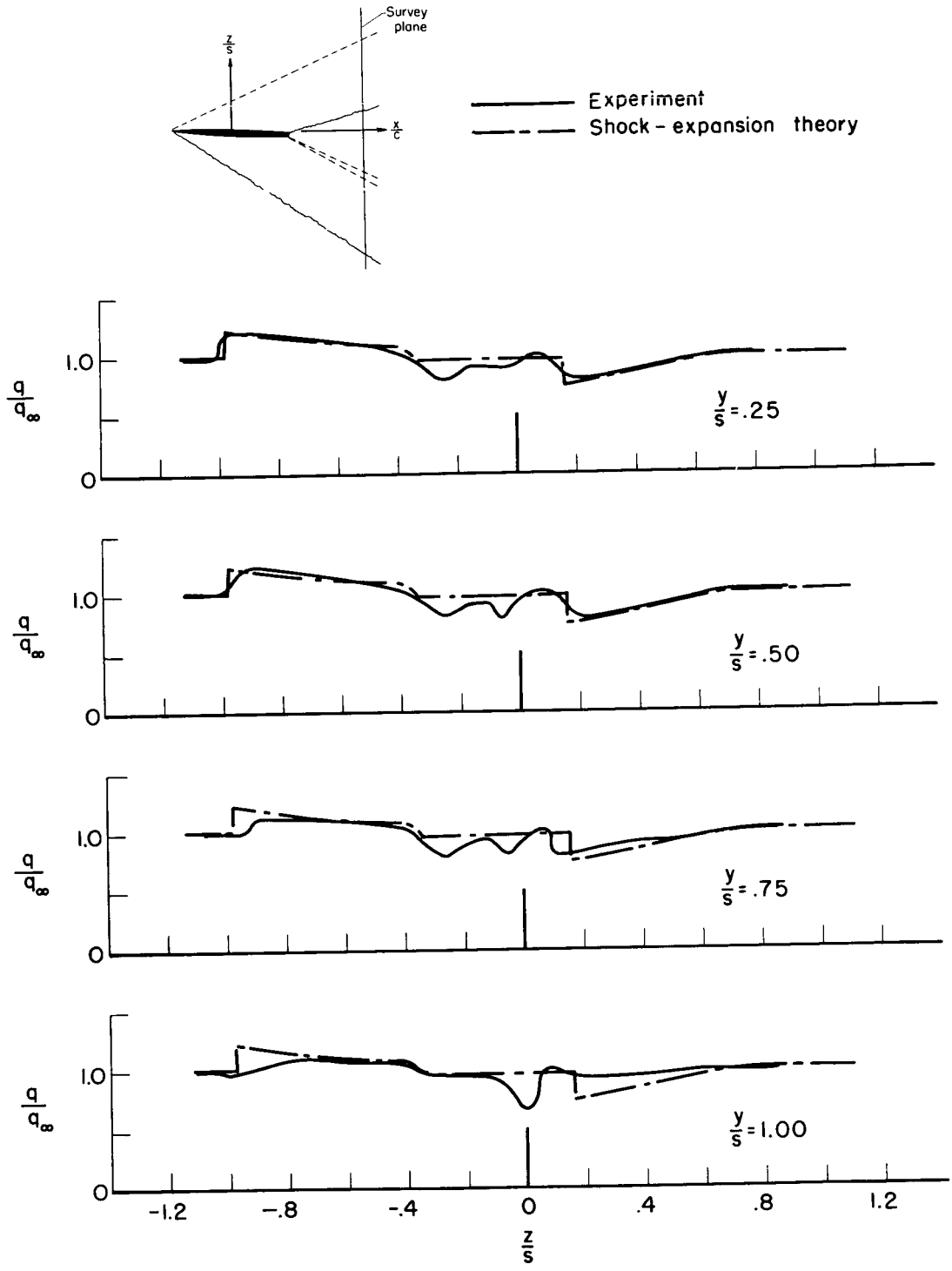

(b) x/c = 1.10

Figure 28.- Concluded.

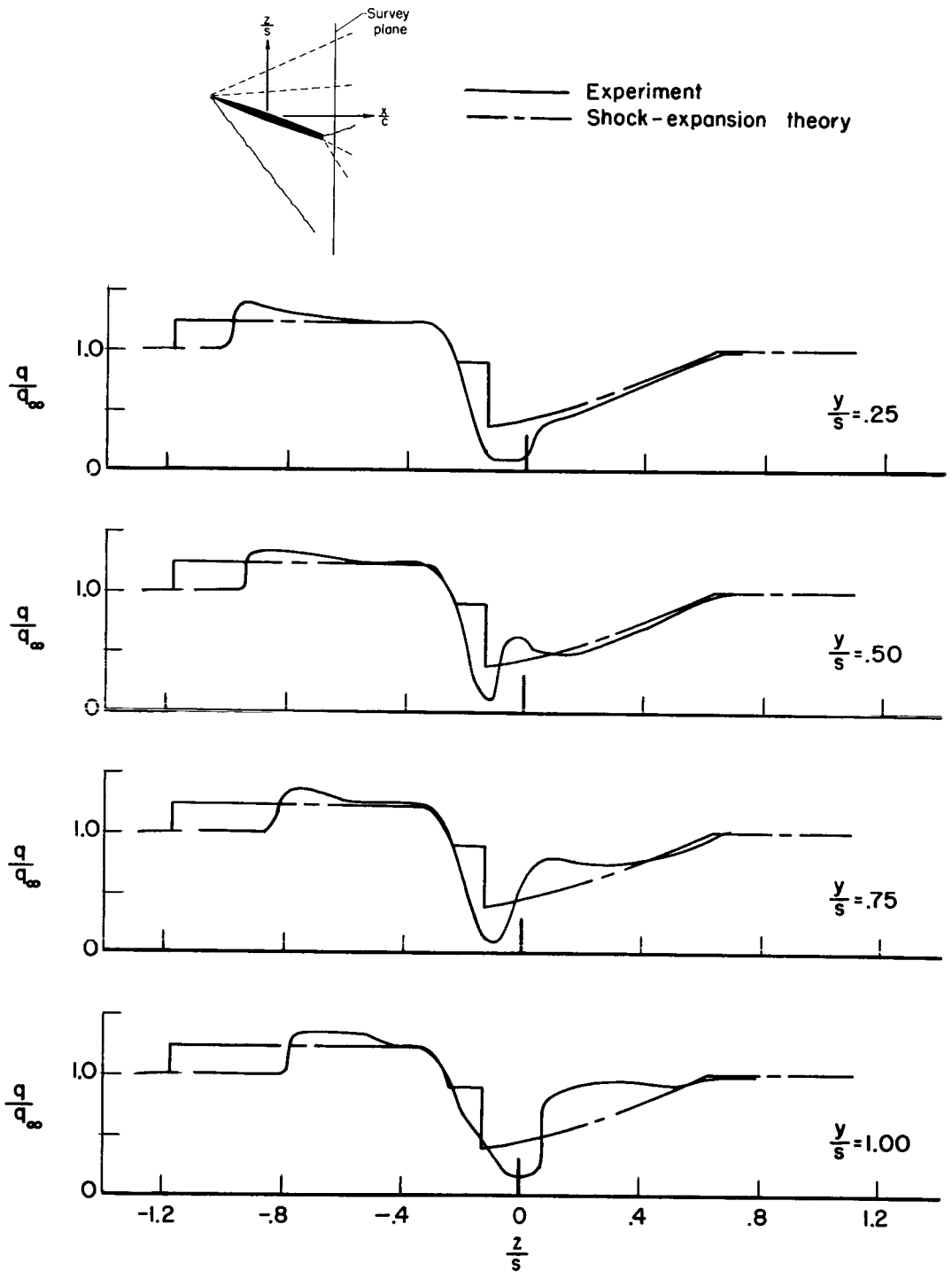

(a) x/c = 0.56

Figure 29.- Comparison of measured dynamic pressure behind rectangular wing with shock-expansion theory; $\alpha = 20^{\circ}$.

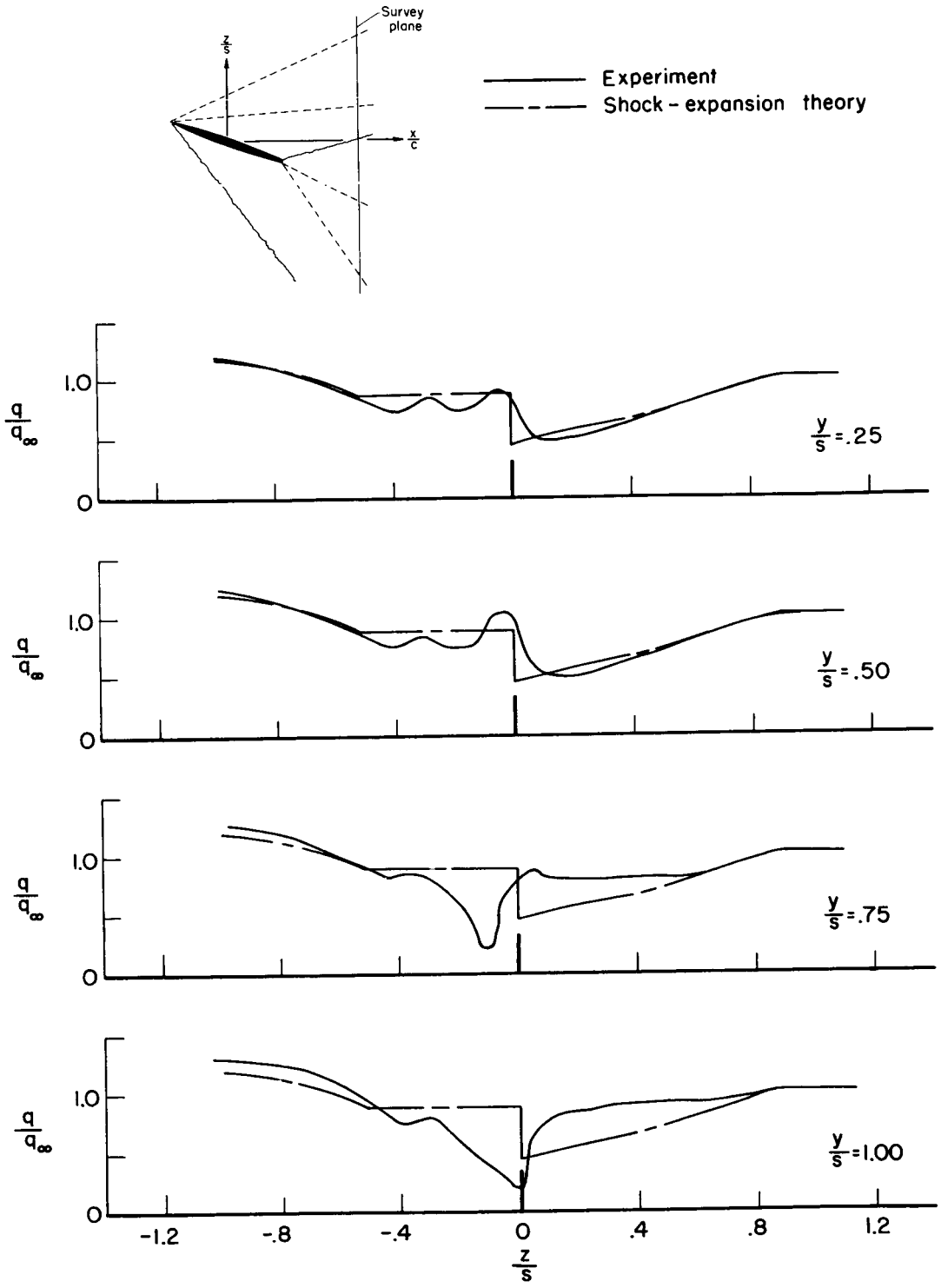

(b) x/c = 1.10

Figure 29.- Concluded.

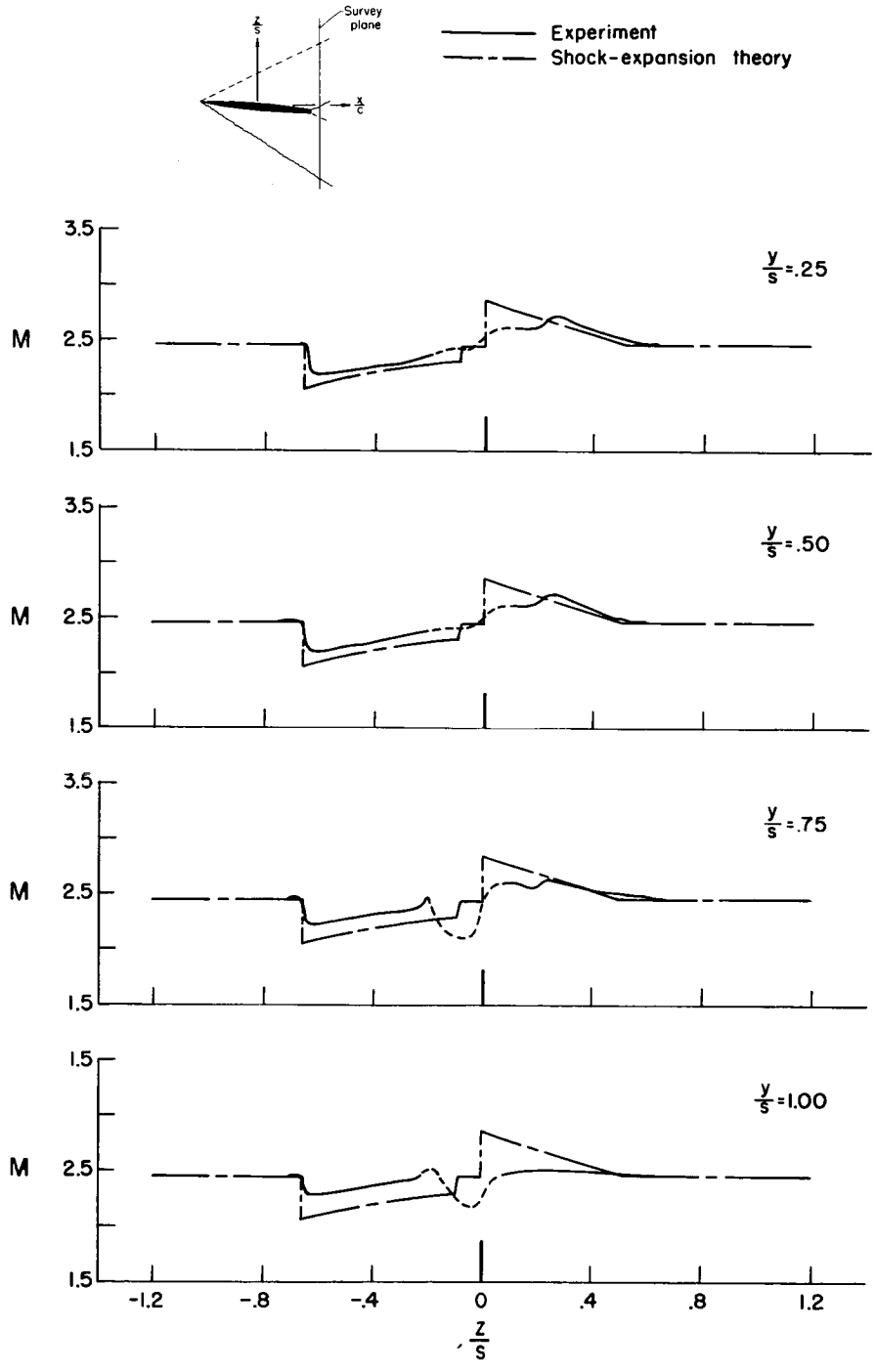

(a) x/c = 0.56

Figure 30.- Comparison of measured Mach number behind rectangular wing with shock-expansion theory; $\alpha = 6^{\circ}$.

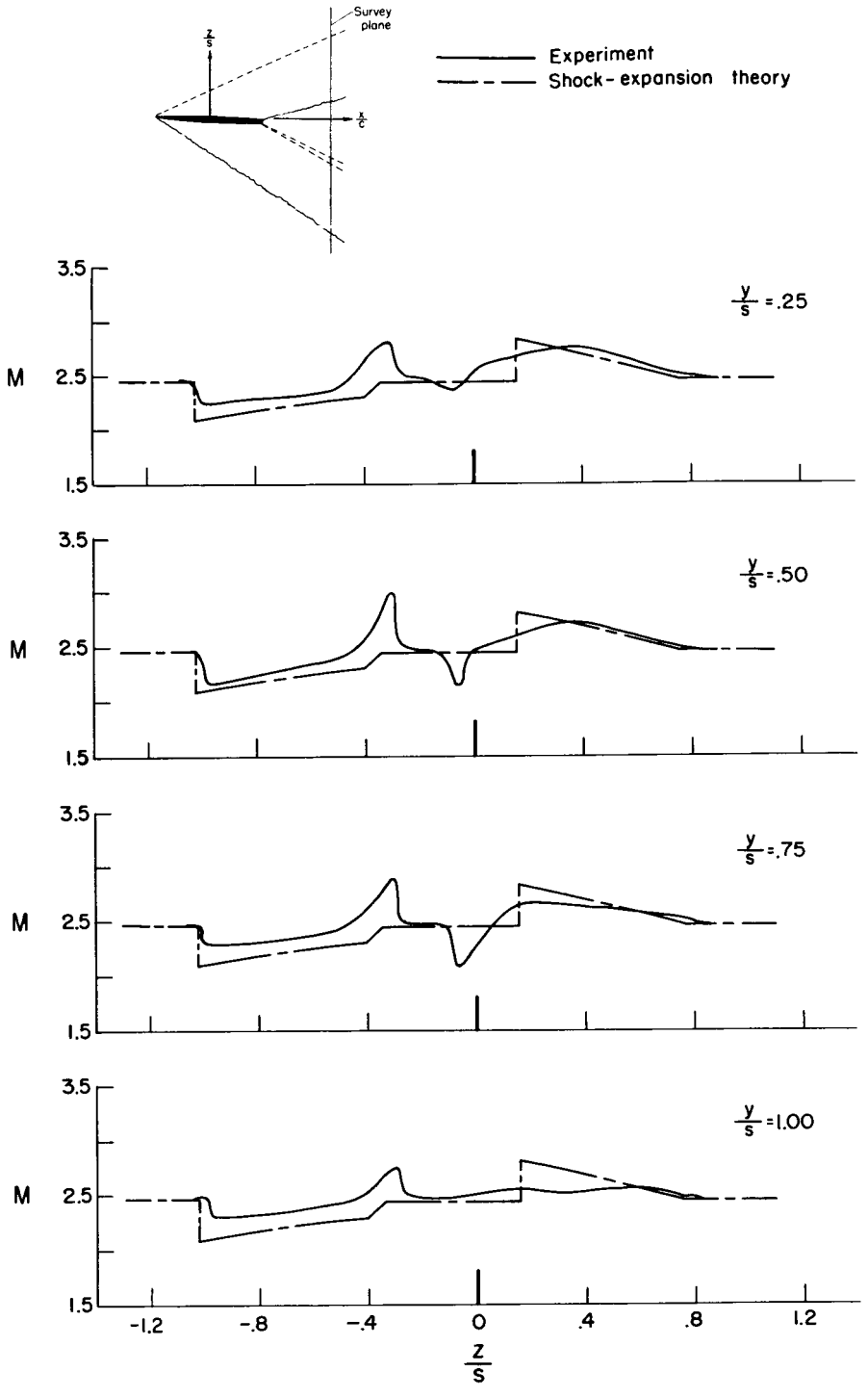

(b) x/c = 1.10

Figure 30.- Concluded.

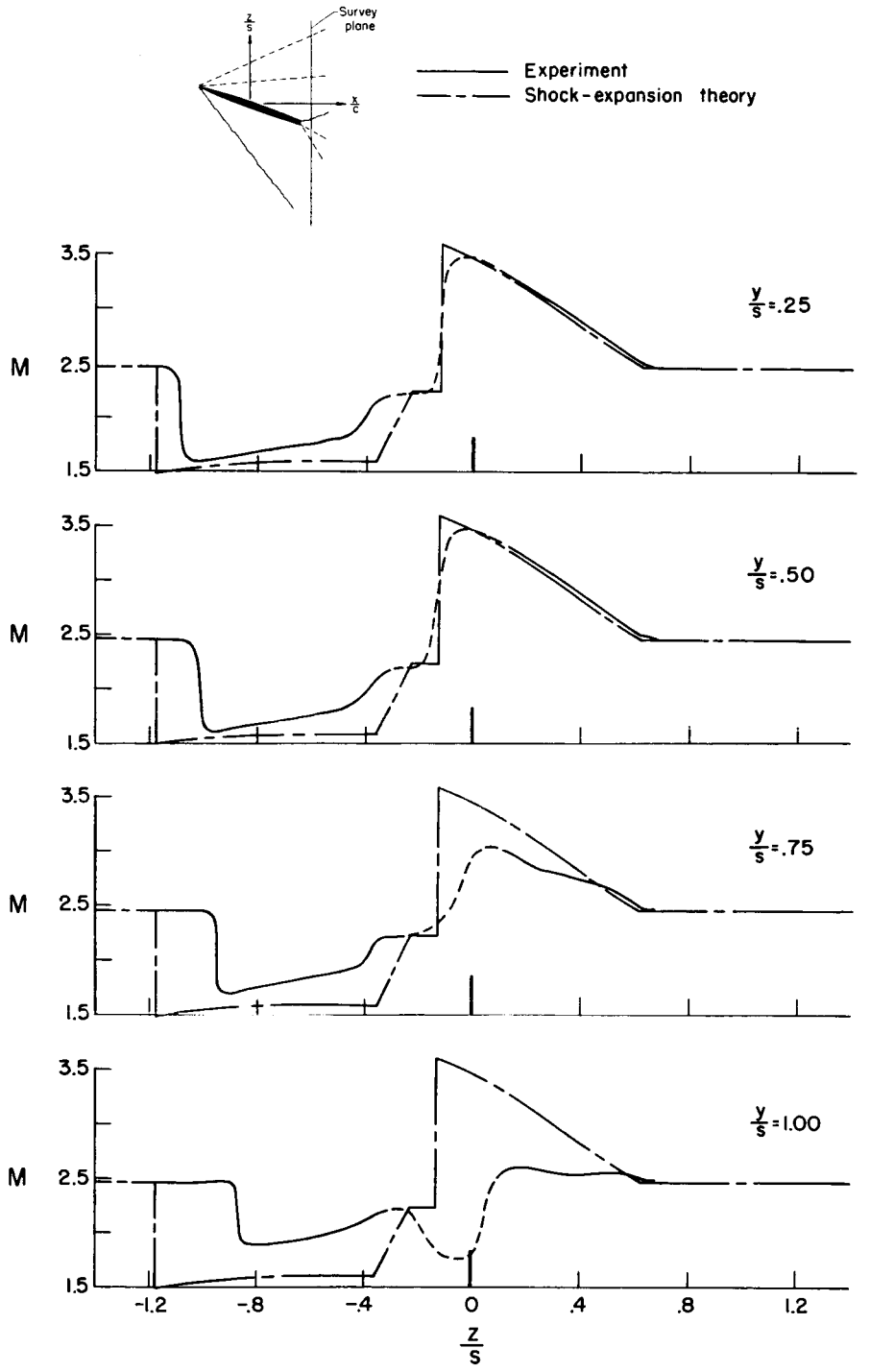

(a) x/c = 0.56

Figure 31.- Comparison of measured Mach number behind rectangular wing with shock-expansion theory; $\alpha = 20^{\circ}$.

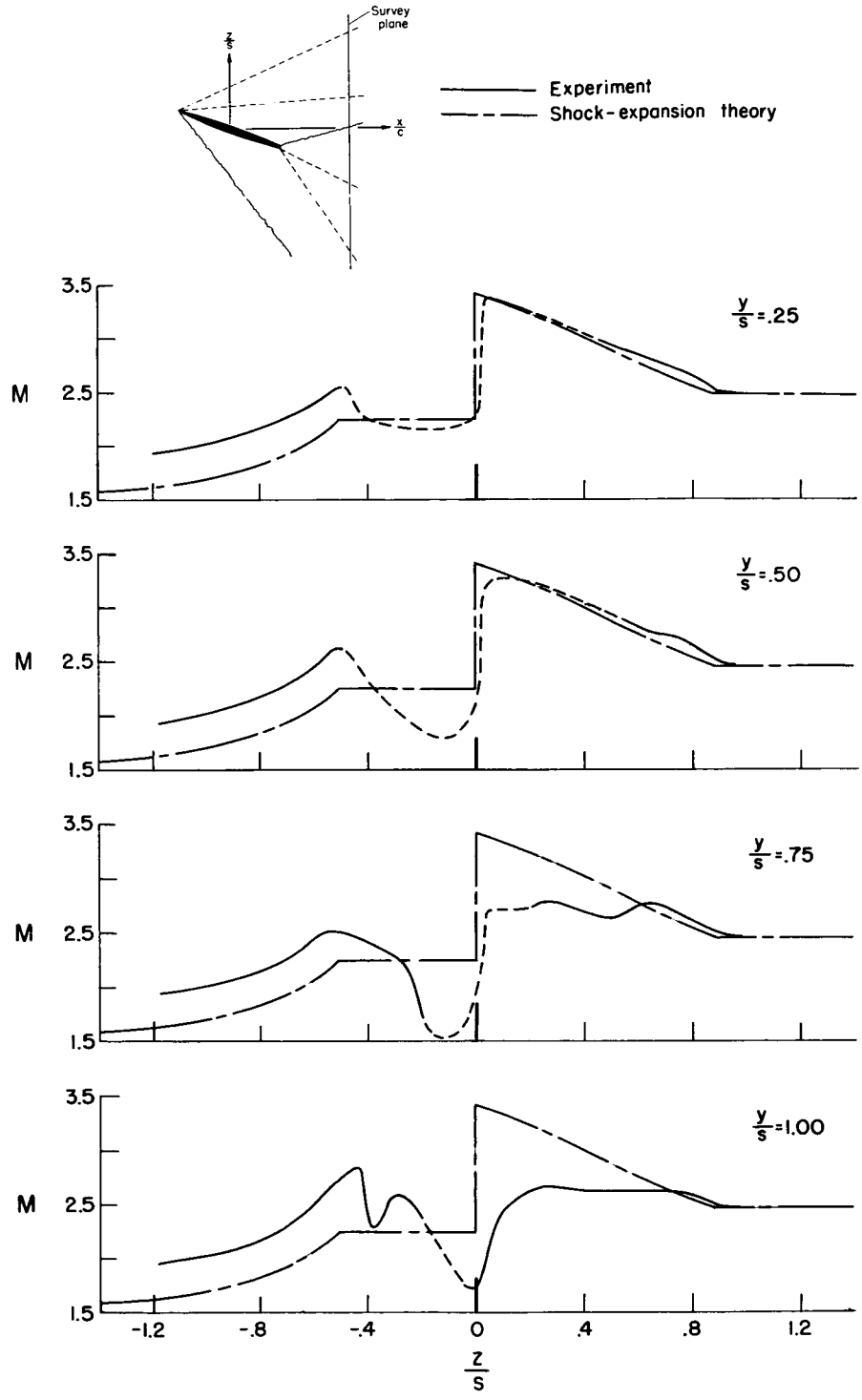

(b) x/c = 1.10

Figure 31.- Concluded.

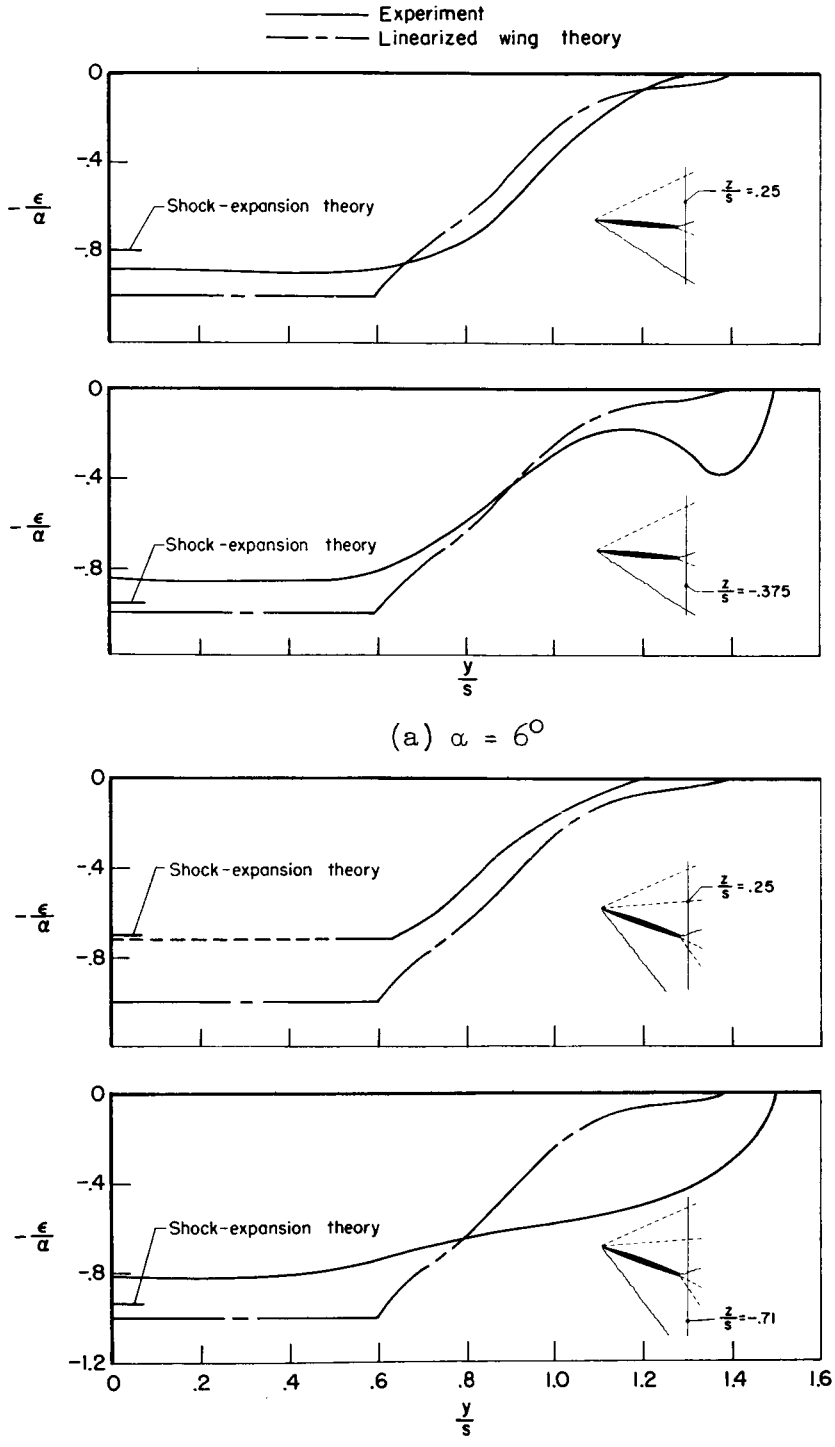

Figure 32.- Comparison of measured downwash behind rectangular wing with theory; x/c = 0.56.

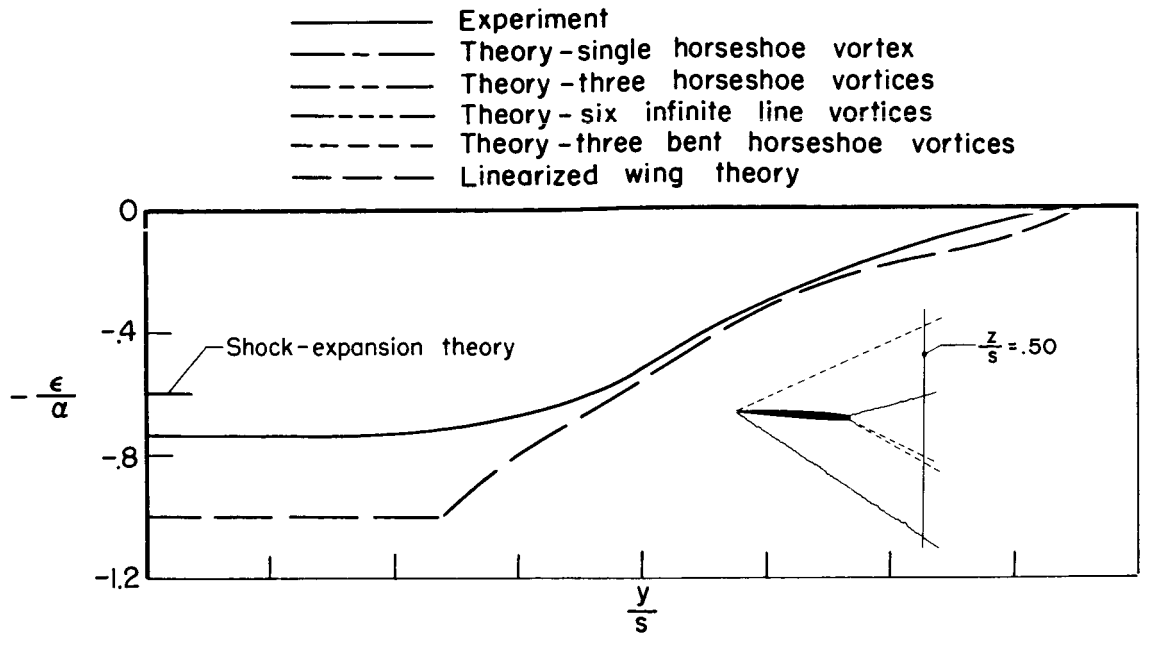

(a) $z/s = 0.50$

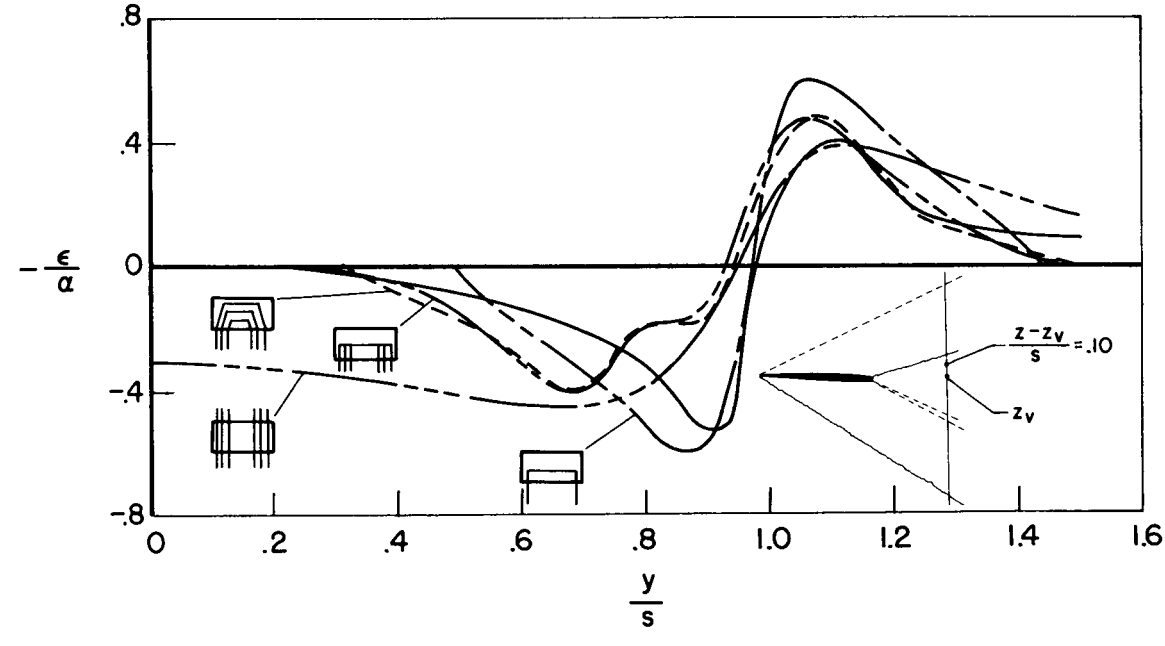

(b) $(z-z_v)/s = 0.10$; $z_v/s = -0.025$

Figure 33.- Comparison of measured downwash behind rectangular wing with theory; $\alpha = 6^\circ$; $x/c = 1.10$.

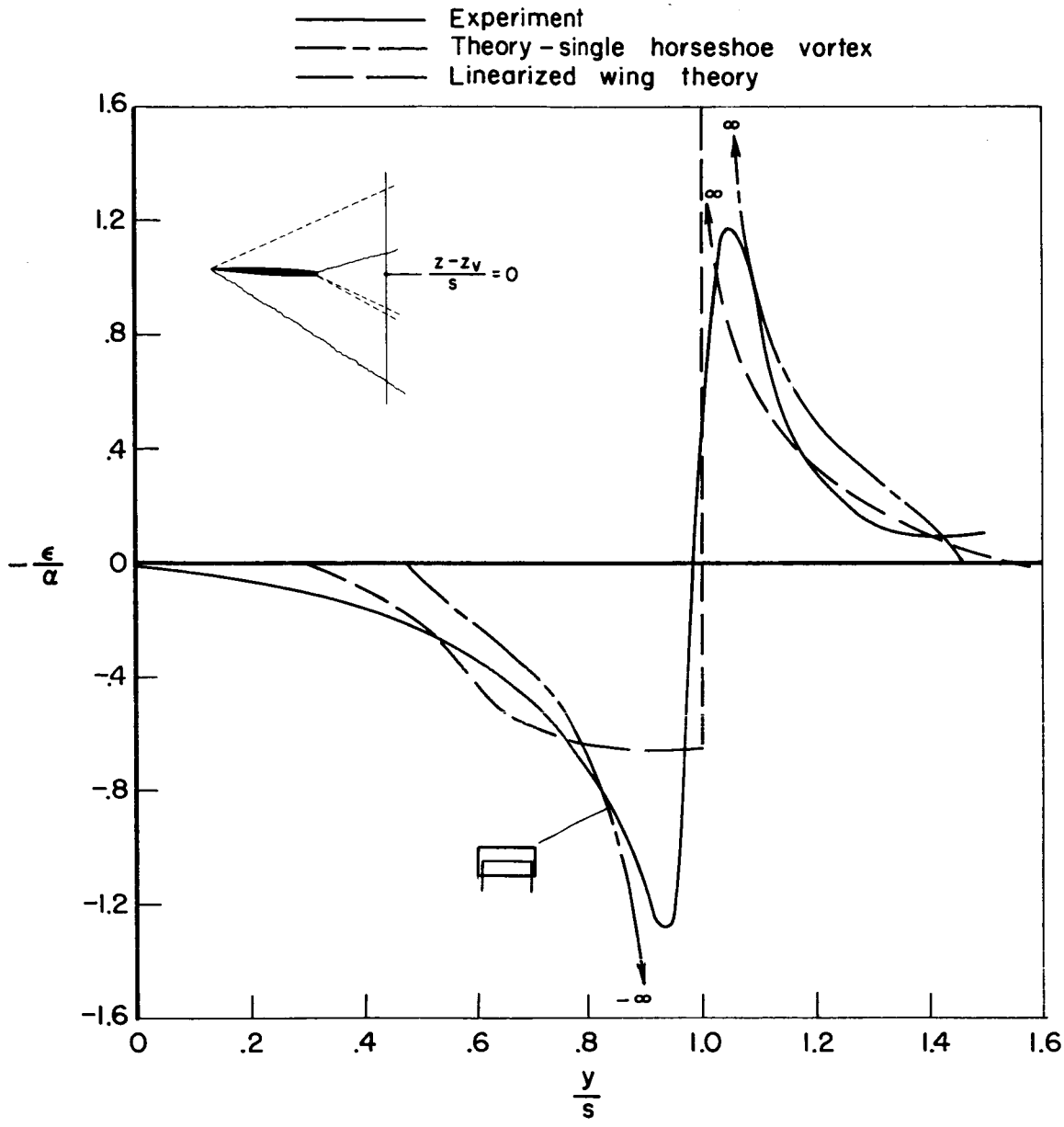

(c) $(z-z_v)/s = 0$; $z_v/s = 0.025$

Figure 33.- Continued.

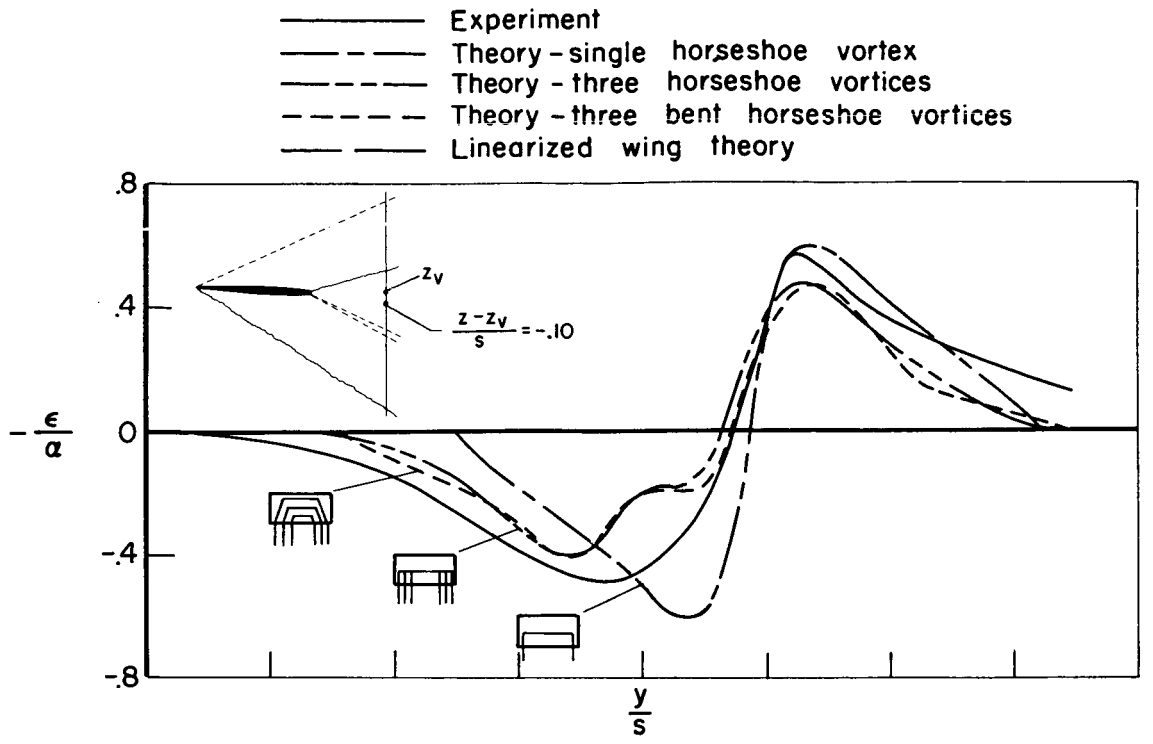

(d) $(z-z_v)/s = 0.10$, $z_v/s = -0.025$

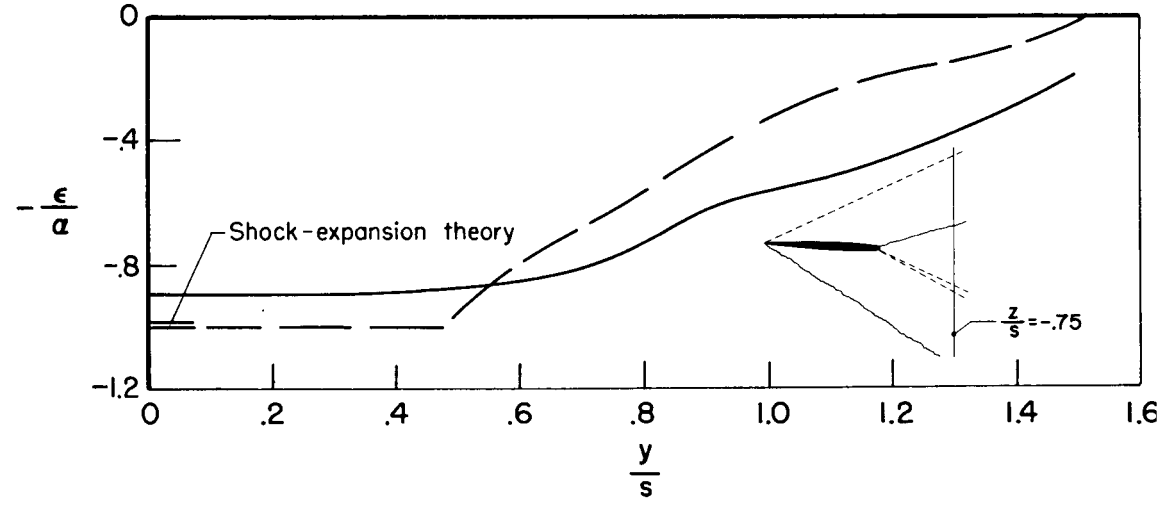

(e) $z/s = -0.75$

Figure 33.- Concluded.

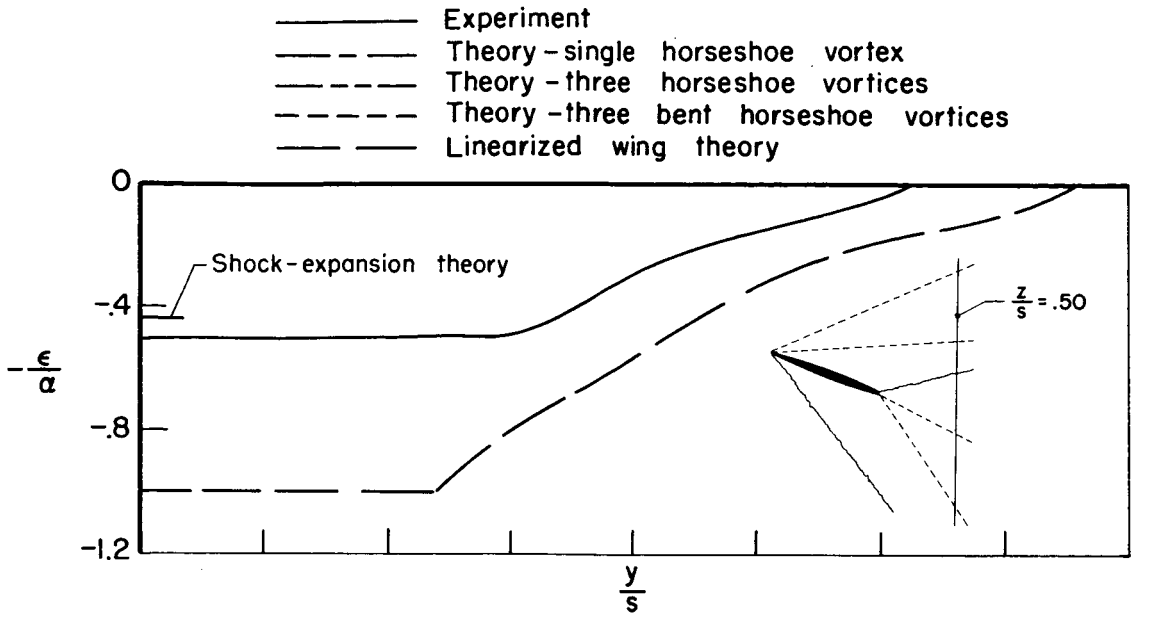

(a) z/s = 0.50

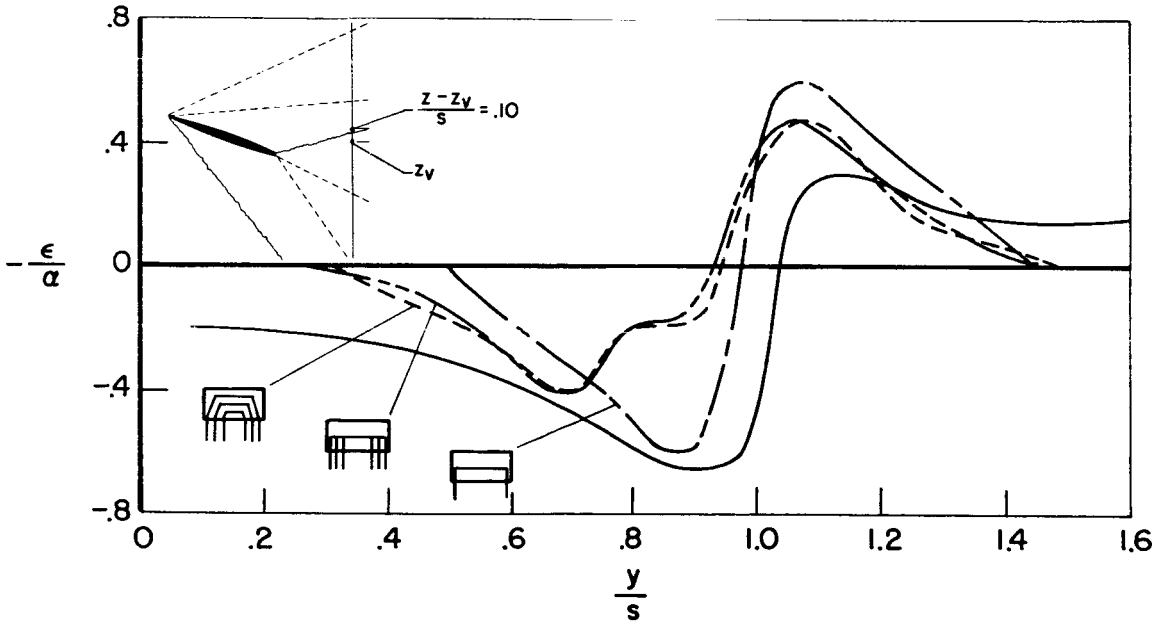

(b) $(z-z_v)/s = 0.10$; $z_v/s = -0.062$

Figure 34.- Comparison of measured downwash behind rectangular wing with theory; $\alpha = 20^\circ$; $x/c = 1.10$.

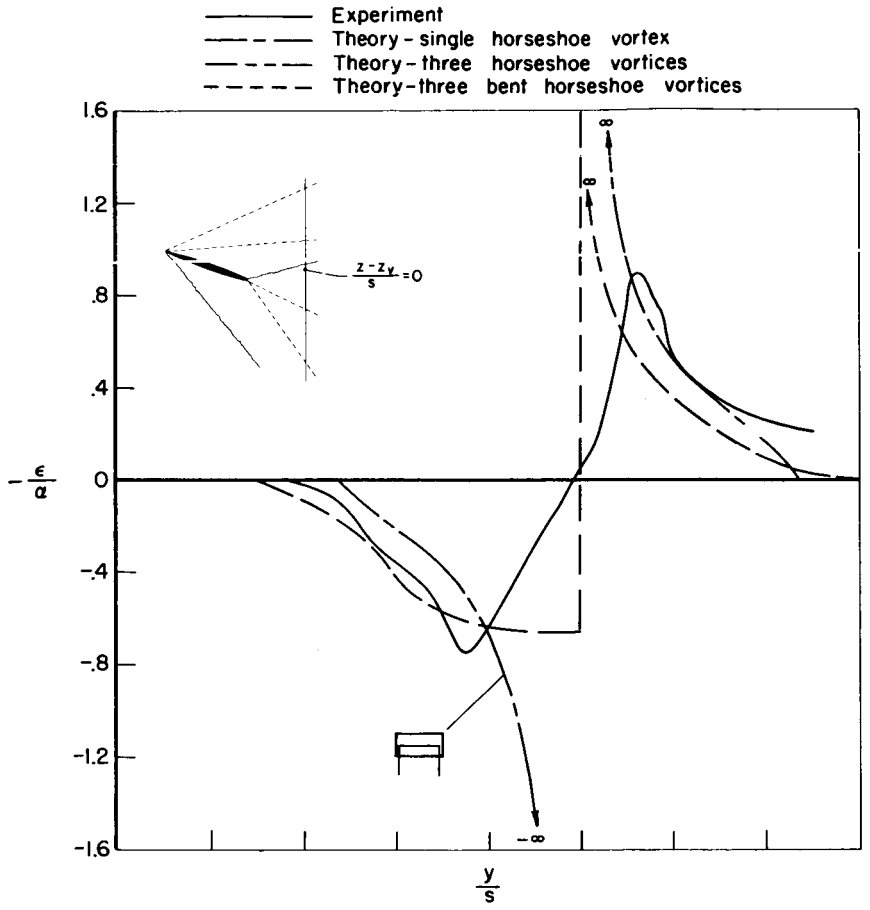

(c) $(z-z_V)/s = 0$; $z_V/s = -0.062$

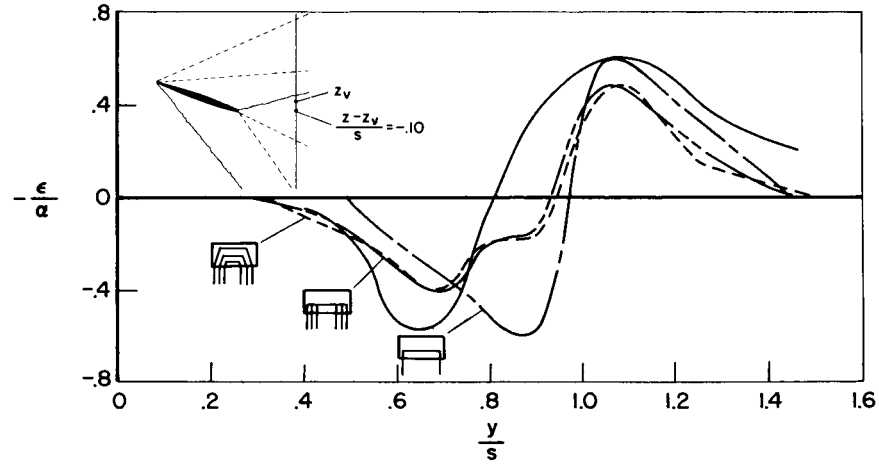

(d) $(z-z_V)/s = -0.10$; $z_V/s = -0.062$

Figure 34.- Concluded.

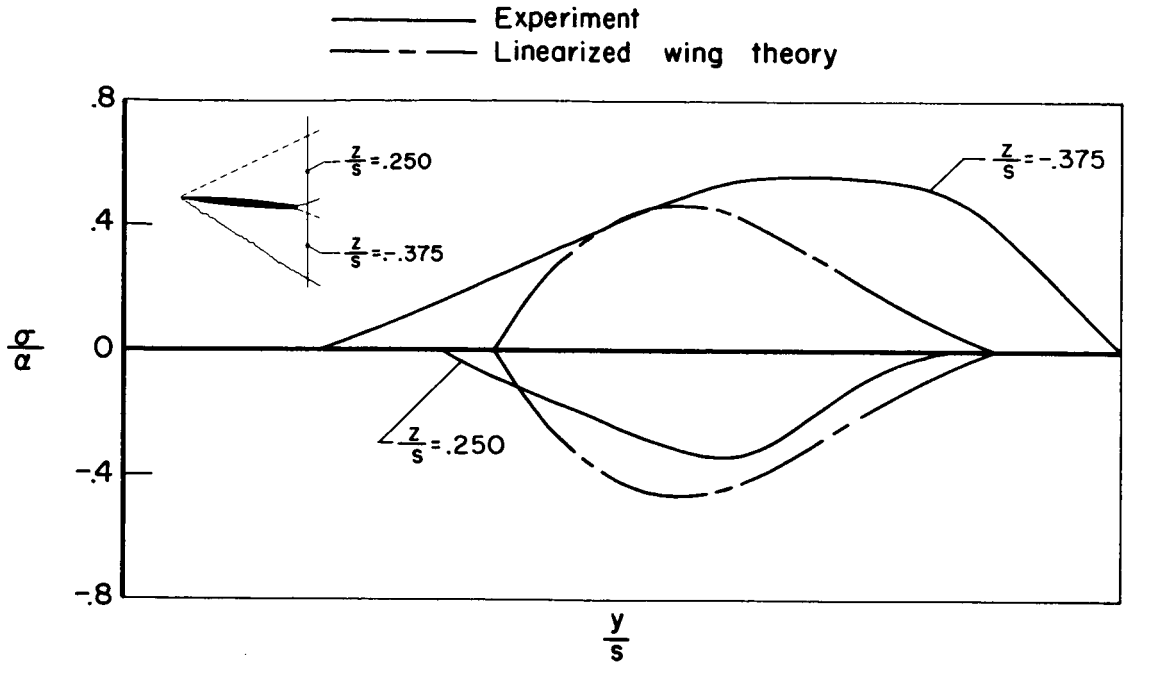

(a) $\alpha = 6^\circ$

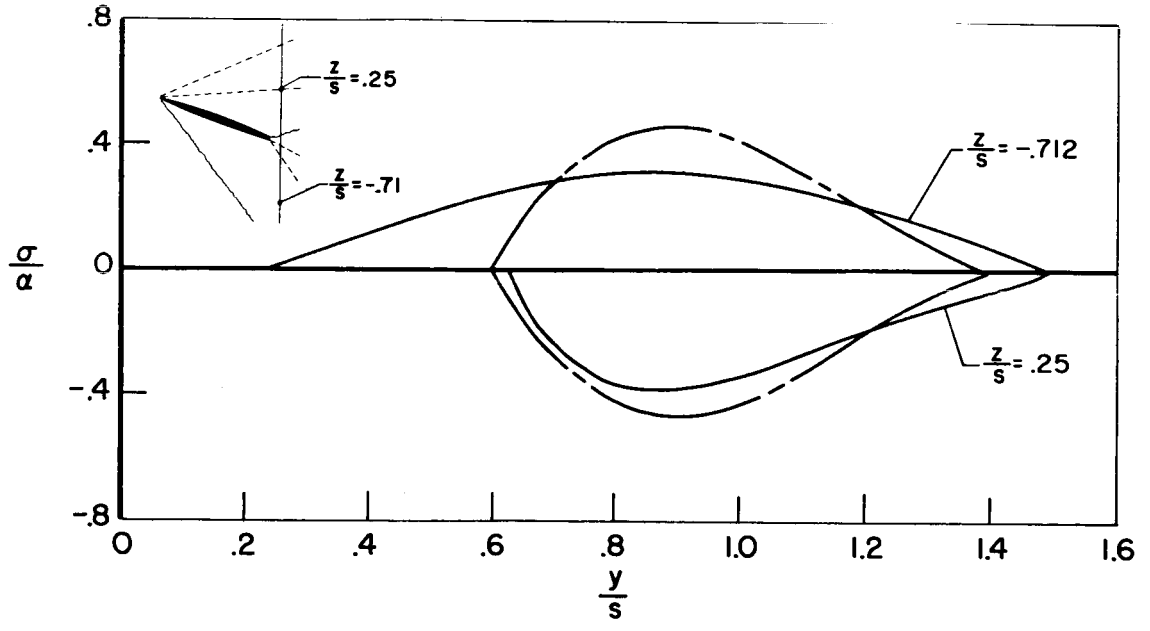

(b) $\alpha = 20^\circ$

Figure 35.- Comparison of measured sidewash behind rectangular wing with theory; x/c = 0.56.

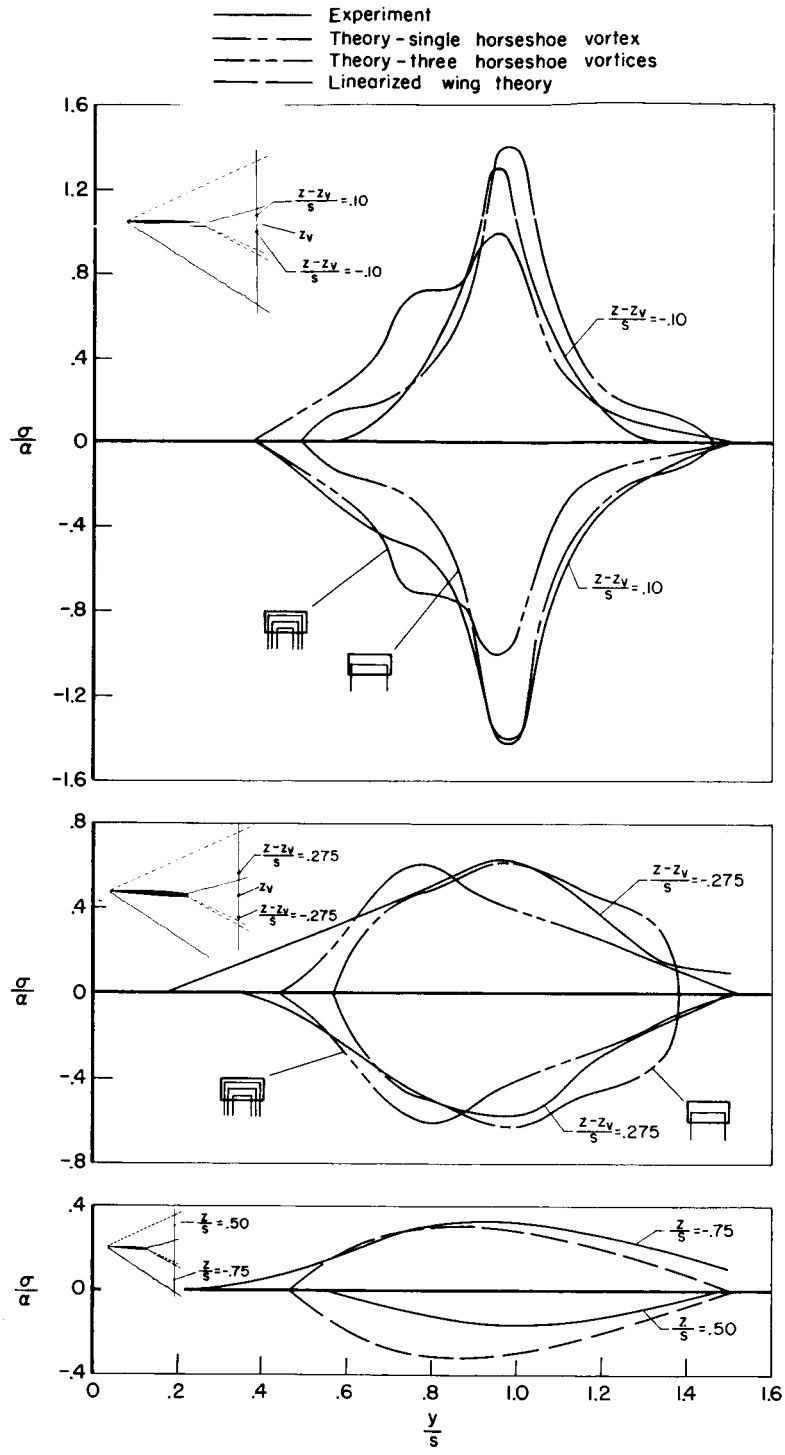

Figure 36. - Comparison of measured sidewash behind rectangular wing with theory; $\alpha = 6^{\circ}$; $x/c = 1.10$.

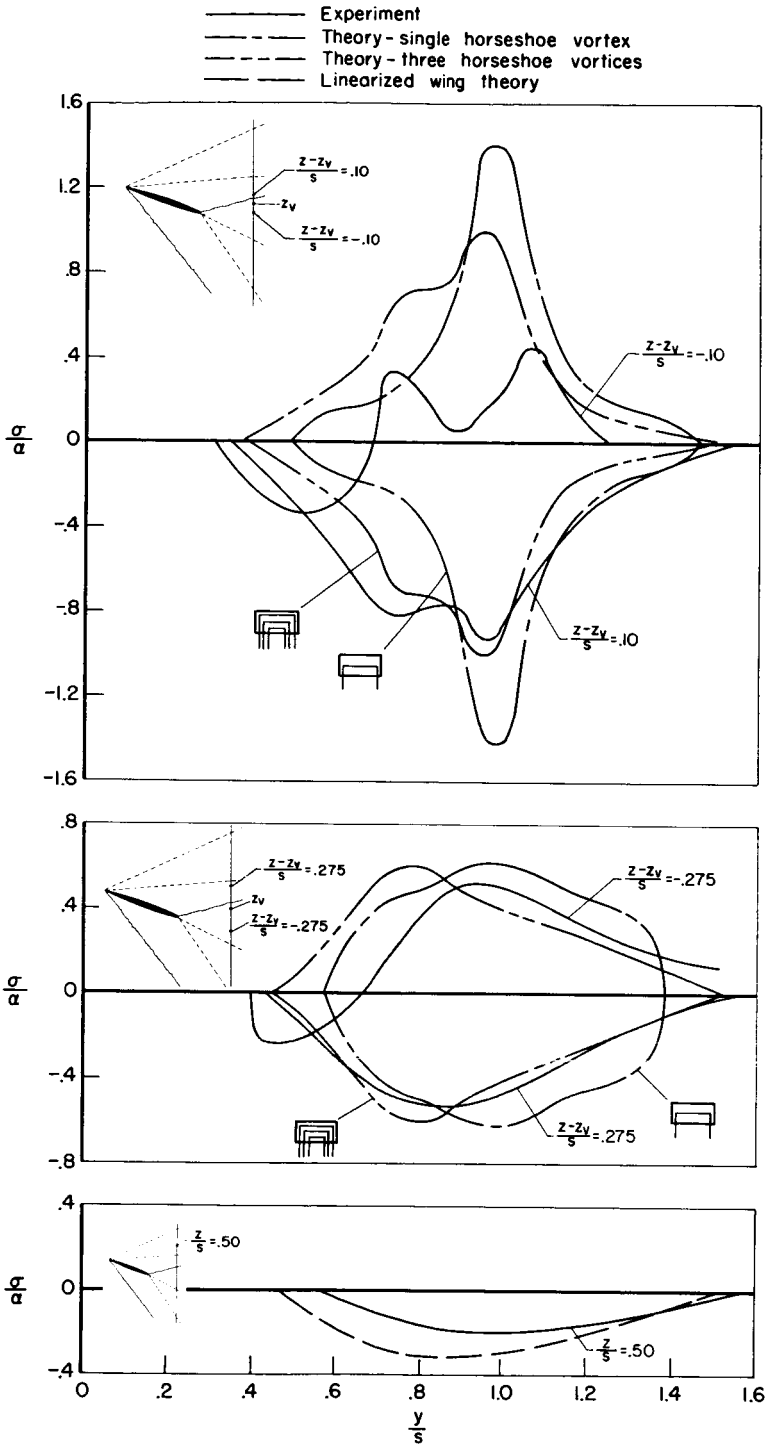

Figure 37.- Comparison of measured sidewash behind rectangular wing with theory; $\alpha = 20^{\circ}$; $x/c = 1.10$.

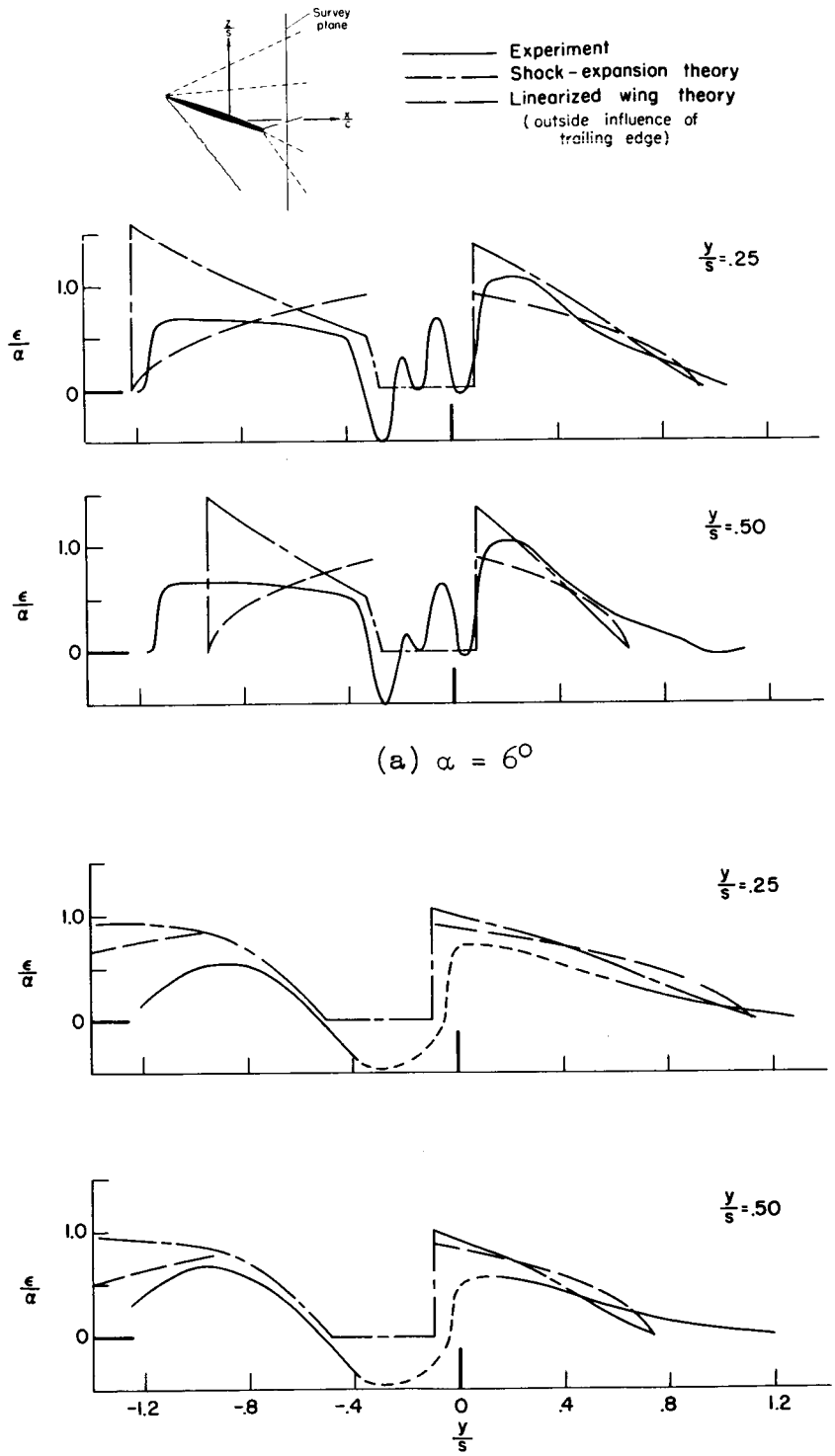

Figure 38.- Comparison of measured downwash behind triangular wing with theory; $x/c_R = 0.55$.

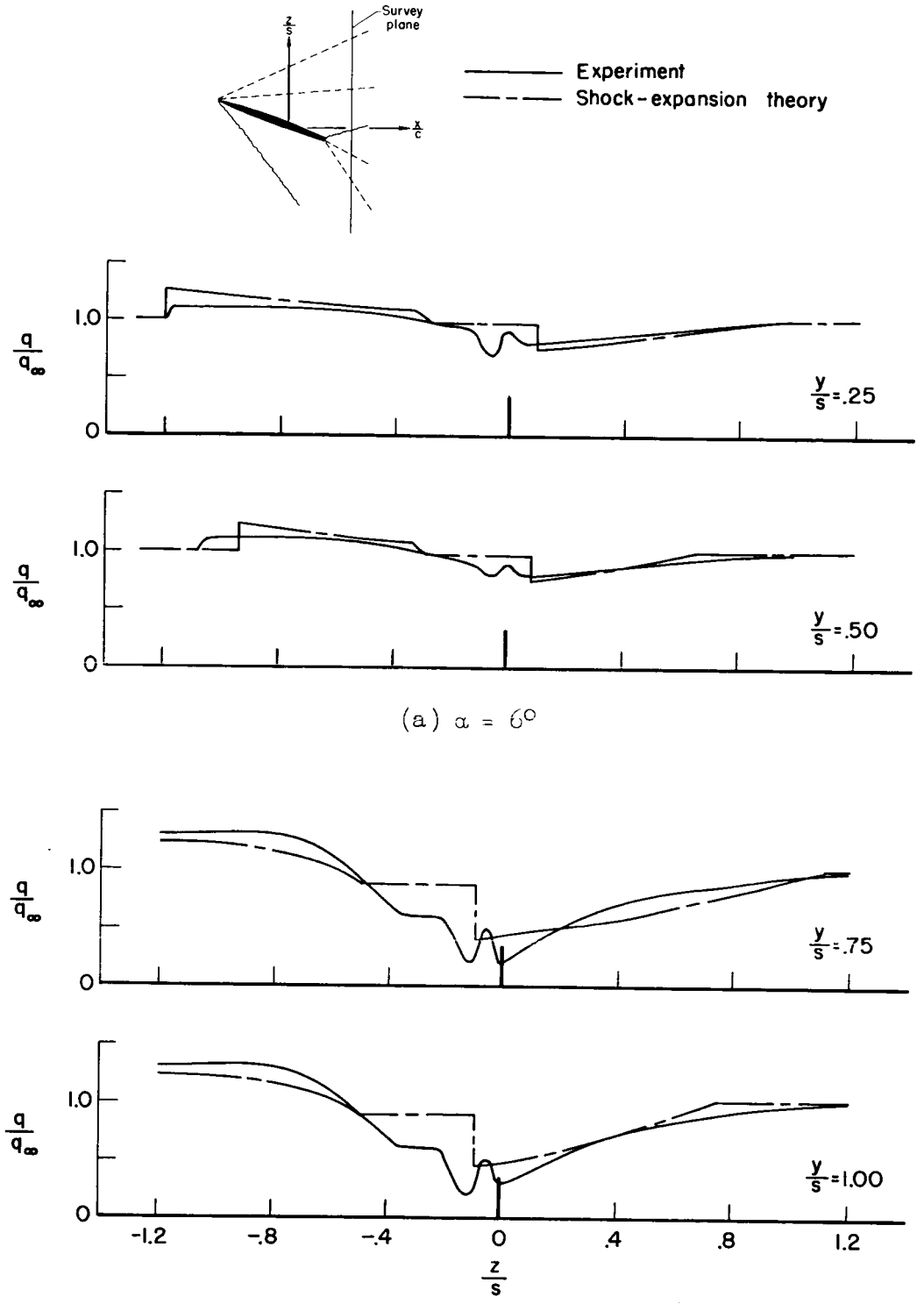

Figure 39.- Comparison of measured dynamic pressure behind triangular wing with shock-expansion theory; x/c_R = 0.55.

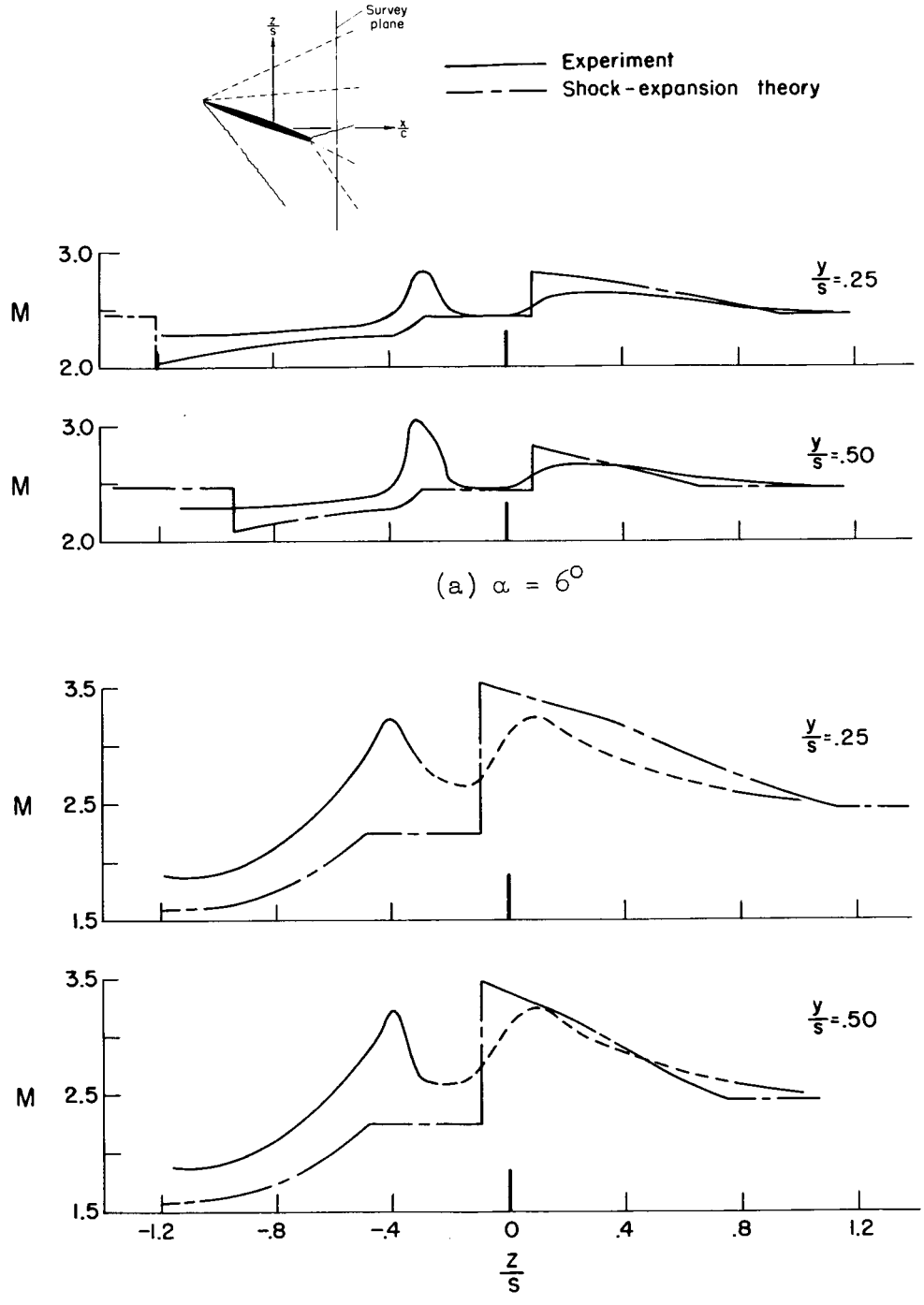

Figure 40.- Comparison of measured Mach number behind triangular wing with shock-expansion theory; $x/c_R = 0.55$.

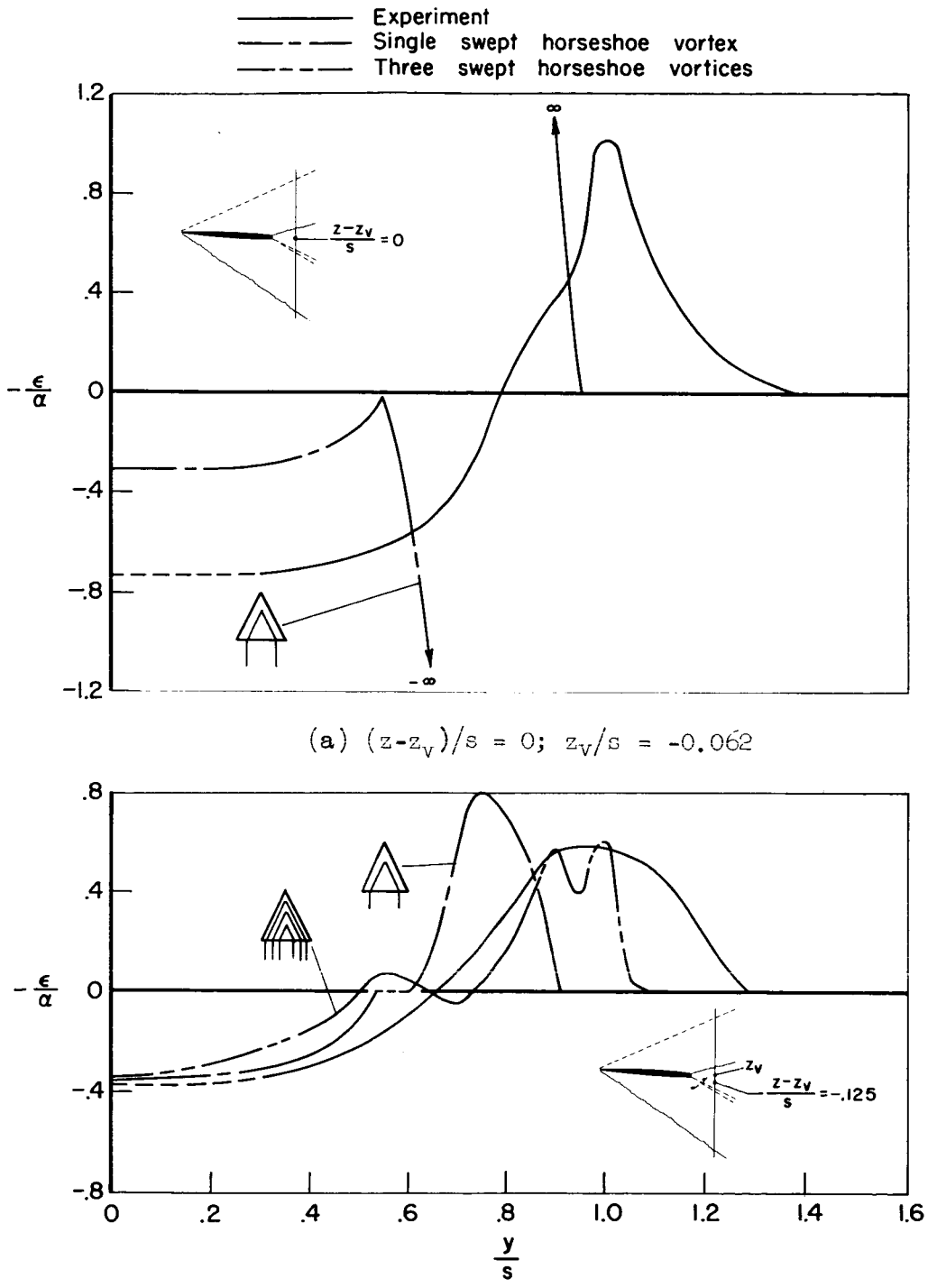

Figure 41.- Comparison of measured downwash behind triangular wing with theory; $\alpha = 6^{\circ}$; $x/c_R = 0.55$.

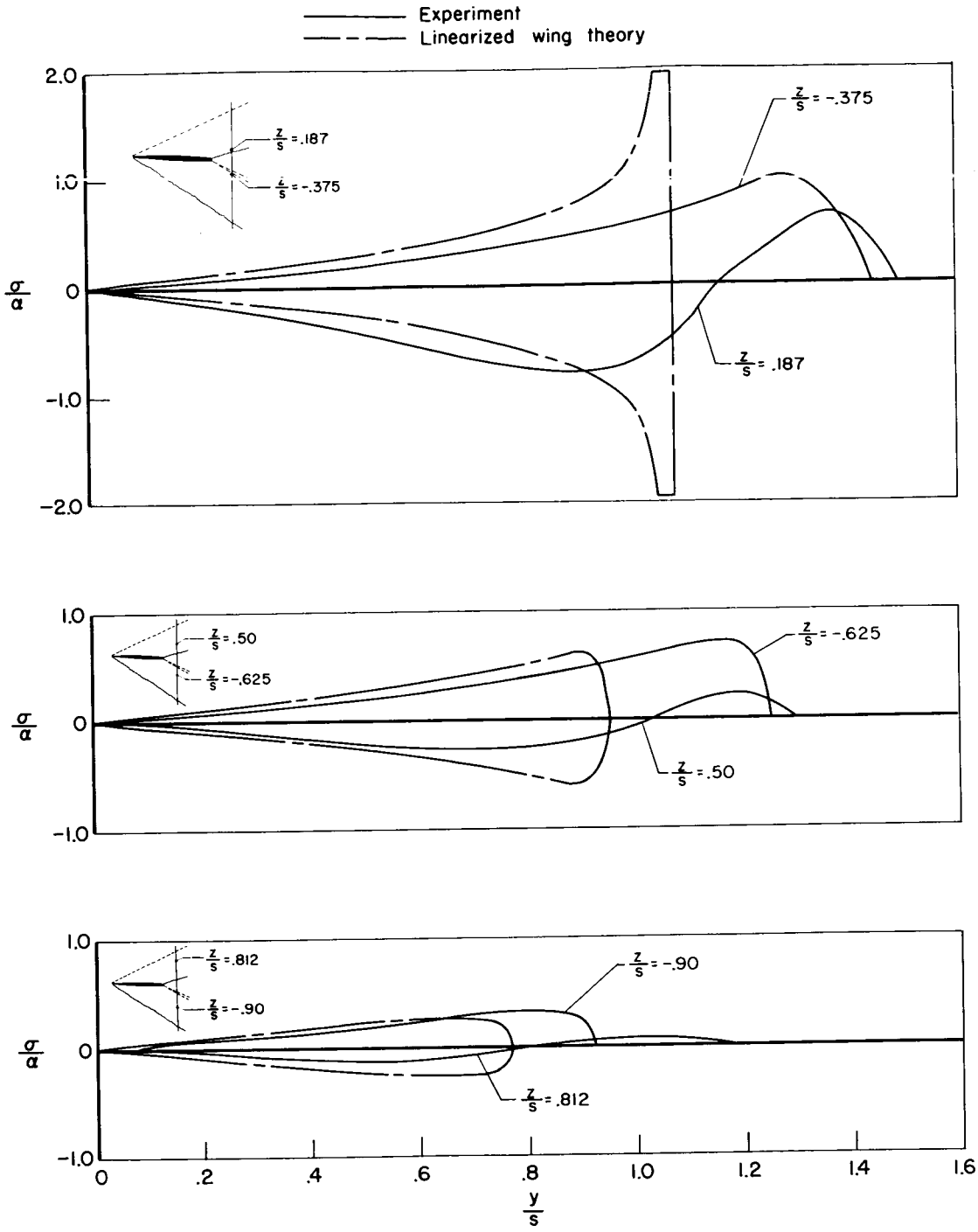

(a) $\alpha = 6^{\circ}$

Figure 42.- Comparison of measured sidewash behind triangular wing with theory; $x/c_R = 0.55$.

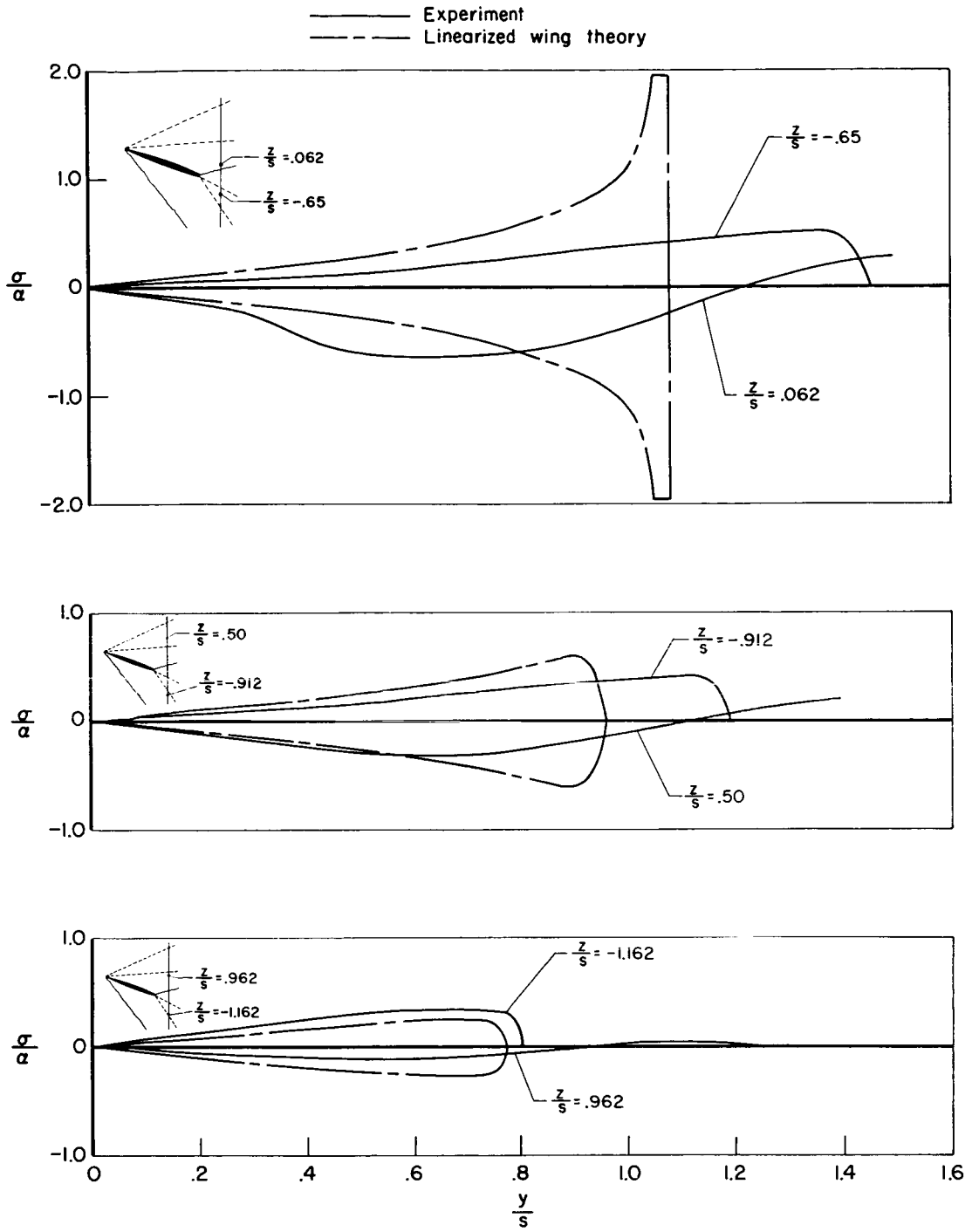

(b) $\alpha = 20^{\circ}$

Figure 42.- Concluded.

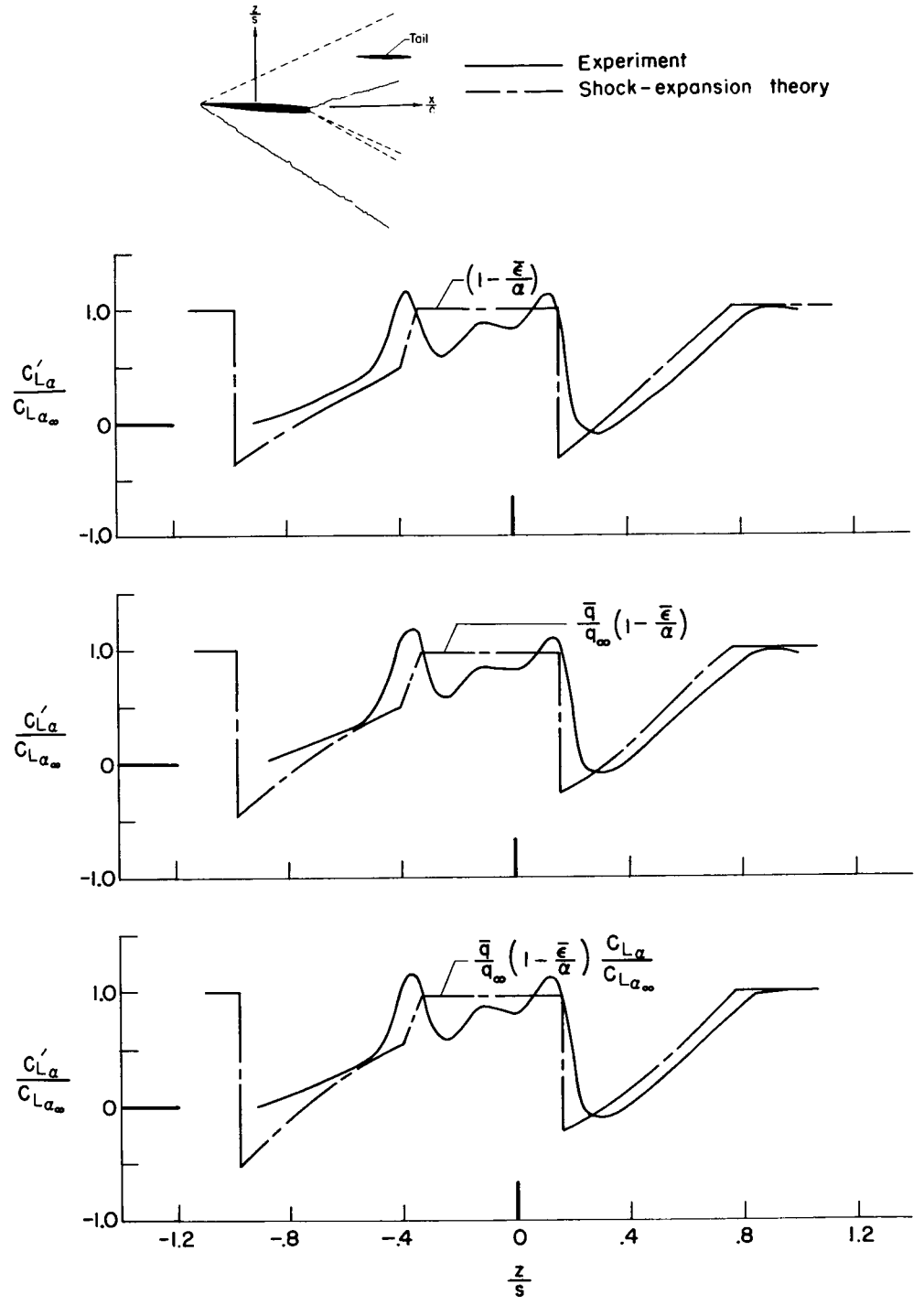

(a) $\alpha = 6^\circ$

Figure 43.- Effectiveness of horizontal tail in wake of rectangular wing; $S_t/S_w = 0.50$; $x/c = 1.10$.

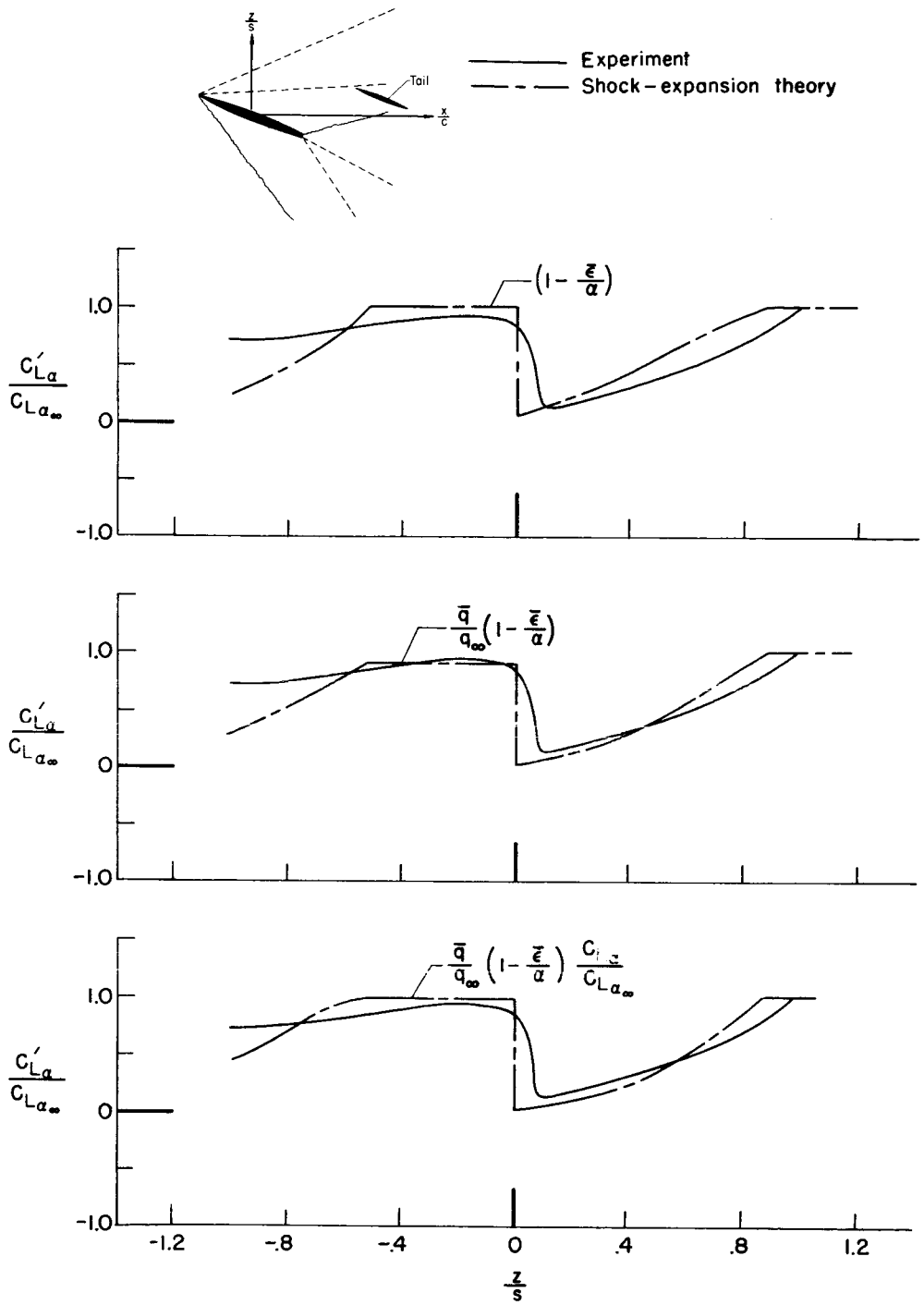

(b) $\alpha = 20^\circ$

Figure 43.- Concluded.